

2020

Observing and modeling climate controls and feedbacks on vegetation phenology at local-to-continental scales

<https://hdl.handle.net/2144/41532>

"Downloaded from OpenBU. Boston University's institutional repository."

BOSTON UNIVERSITY
GRADUATE SCHOOL OF ARTS AND SCIENCES

Dissertation

**OBSERVING AND MODELING CLIMATE CONTROLS AND FEEDBACKS ON
VEGETATION PHENOLOGY AT LOCAL-TO-CONTINENTAL SCALES**

by

MINKYU MOON

B.A., Seoul National University, 2012
M.S., Seoul National University, 2014

Submitted in partial fulfillment of the
requirements for the degree of
Doctor of Philosophy

2020

© 2020 by
MINKYU MOON
All rights reserved

Approved by

First Reader

Mark A. Friedl, Ph.D.
Professor of Earth and Environment

Second Reader

Michael C. Dietze, Ph.D.
Associate Professor of Earth and Environment

Third Reader

Dan Li, Ph.D.
Assistant Professor of Earth and Environment

ACKNOWLEDGMENTS

NASA grant number NNX15AB96A and NSF grant number EF-1702627 supported this research.

The first and third chapters of this dissertation were previously published in *Remote Sensing of Environment* (Moon et al., 2019) and *Agricultural and Forest Meteorology* (Moon et al., 2020).

I would like to thank all faculty members, students, administrative staff from the Earth and Environment department, and the committee members, Mike Dietze, Dan Li, and Andrew Richardson, and especially my advisor Mark Friedl, for their advice, friendship, and support.

I would also like to thank all of my family, including my brother, parents and lovely wife and my boys, Jihyuk and Jiwon. I love you all very much.

**OBSERVING AND MODELING CLIMATE CONTROLS AND FEEDBACKS ON
VEGETATION PHENOLOGY AT LOCAL-TO-CONTINENTAL SCALES**

MINKYU MOON

Boston University Graduate School of Arts and Sciences, 2020

Major Professor: Mark A. Friedl, Professor of Earth and Environment

ABSTRACT

Vegetation phenology controls seasonal variation in ecosystem processes and exerts important controls on land-atmosphere exchanges of carbon, water, and energy. However, the ecological processes and interactions between climate and vegetation that control phenology and associated feedbacks to the atmosphere are not fully understood. In this dissertation, I use remote sensing in combination with climate and ecological data to improve understanding of biophysical controls and feedbacks between vegetation phenology and the atmosphere in temperate forest ecosystems of North America.

In the first part of this dissertation, I evaluate the agreement and characterize the similarities and differences between land surface phenology products from two remote sensing instruments (MODIS and VIIRS) that are designed to provide long-term continuity of land surface phenology measurements at global scale. Results from this analysis indicate that the VIIRS land surface phenology product provides excellent continuity with the MODIS record despite subtle differences between each instrument and the algorithms used to generate each product. In the second part of this dissertation, a state-space Bayesian modeling framework is applied to seventeen years of MODIS and daily weather data to

improve understanding of what controls the timing of springtime phenology in deciduous forests of temperate and boreal North America. Results show that photoperiod is more important in warmer regions than in colder regions, which contradicts a widely held hypothesis that photoperiod provides a key safety mechanism preventing early leaf-out during springtime. In the final part of this dissertation, I use a physically-based attribution method to quantify the relative importance of covarying surface biophysical and atmospheric variables in modifying the surface energy balance during springtime. Results show that the widely observed decrease in the Bowen ratio that occurs with leaf emergence is not solely attributable to changes in surface resistance caused by increasing leaf area during spring. Rather, observed changes in the Bowen ratio reflect the combined effects of changes in surface properties and atmospheric conditions. The results from this dissertation provide an improved foundation for long-term studies focused on observing and modeling springtime vegetation phenology and associated feedbacks to the atmosphere in deciduous forest ecosystems at local-to-continental scales.

TABLE OF CONTENTS

ACKNOWLEDGMENTS	iv
ABSTRACT	v
TABLE OF CONTENTS.....	vii
LIST OF TABLES	xi
LIST OF FIGURES	xiii
LIST OF ABBREVIATIONS.....	xx
1. INTRODUCTION	1
1.1. Land surface phenology from satellite remote sensing	3
1.2. Climate controls on land surface phenology.....	5
1.3. Vegetation phenology feedbacks on land-atmosphere interaction	6
1.4. Research objectives and questions.....	7
2. LONG-TERM CONTINUITY IN LAND SURFACE PHENOLOGY MEASUREMENTS: A COMPARATIVE ASSESSMENT OF THE MODIS LAND COVER DYNAMICS AND VIIRS LAND SURFACE PHENOLOGY PRODUCTS	9
2.1. Introduction.....	9
2.2. Data and Methods	11
2.2.1. Overview of land surface phenology product algorithms.....	11
2.2.2. Intercomparison of land surface phenology products.....	13
2.2.3. Attribution of differences related to sensors versus algorithms.....	15
2.2.4. Comparison with results from the Landsat Phenology Algorithm	17
2.2.5. Comparison with phenometrics from the PhenoCam Dataset V1.0	18

2.3. Results.....	19
2.3.1. Baseline comparison of the VIIRS LSP and MODIS LCD products	19
2.3.2. Analysis and attribution of differences across products	26
2.3.3. Comparison with Landsat phenology	32
2.3.4. Comparison with PhenoCam phenology	37
2.4. Discussion.....	41
2.4.1 Comparison of MODIS LCD and VIIRS LSP products.....	41
2.4.2 Comparisons with independent data	44
2.5. Conclusion.....	46
3. CLIMATE CONTROLS ON SPRINGTIME PHENOLOGY IN EASTERN TEMPERATE FORESTS OF NORTH AMERICA.....	48
3.1. Introduction.....	48
3.2. Data and Methods	50
3.2.1. Study region and data.....	50
3.2.2. Springtime phenology model.....	53
3.2.3. Model application	56
3.3. Results.....	58
3.4. Discussion.....	64
3.4.1. Geographical variation in model performance	64
3.4.2. The role of photoperiod on springtime phenology in a changing climate	66
3.5. Conclusions.....	69

4. MODIFICATION OF SURFACE ENERGY BALANCE DURING SPRINGTIME: THE RELATIVE IMPORTANCE OF BIOPHYSICAL AND METEOROLOGICAL CHANGES	70
4.1. Introduction.....	70
4.2. Methods and data	72
4.2.1. Attribution method.....	72
4.2.2. Estimation of changes in surface and atmospheric properties	75
4.2.3. Optimization of attribution method	77
4.2.4. Springtime phenology.....	78
4.2.5. Attribution of changes in aerodynamic resistance	79
4.3. Results and discussion	82
4.3.1. Changes in surface and atmospheric properties during springtime	82
4.3.2. Attribution of decreases in the Bowen ratio	87
4.3.3. Attribution of increases in aerodynamic resistance: the role of wind speed... 93	
4.4. Conclusions.....	96
5. CONCLUSIONS	97
5.1. Summary of key findings.....	98
5.2. Future research.....	100
5.2.1. Moderate spatial resolution land surface phenology	100
5.2.2. Data-driven phenology models with high performance computing systems 101	
5.2.3. Feedbacks between vegetation phenology shifts and biogeochemical cycles	101

APPENDIX A	103
APPENDIX B	106
BIBLIOGRAPHY	107
CURRICULUM VITAE	121

LIST OF TABLES

Table 2.1 Summary statistics (mean, \bar{x} , and standard deviation, σ) for each tile, stratified by the three dominant land cover types from Fig. 2.3, excluding barren and sparsely vegetated pixels. IGBP land cover was derived from the Collection 6 MODIS Land Cover Type product: 4: deciduous broadleaf forests; 5: mixed forests; 7: open shrublands; 8: woody savannas; 9: savannas; 10: grasslands; 12: croplands.	22
Table 2.2 Statistical agreement between the VIIRS LSP and MODIS LCD products in 2013. IGBP denotes land cover type. Bias is calculated as VIIRS – MODIS; RMSD is the root mean squared deviation. See caption of Table 2.1 for IGBP class names.	24
Table 2.3 Linear regression and AI statistics for EVI2 time series from VIIRS and MODIS, stratified by the three most common land cover types in each tile. See caption of Table 2.1 for IGBP class names. RMSD is the root mean squared deviation; 25%, 50%, 75% represent the 1 st quartile, median, and 3 rd quartile, respectively.....	28
Table 2.4 Statistical agreement of the VIIRS LSP and MODIS LCD products with SOS transition dates derived from Landsat in 2013. Bias is calculated as VIIRS – Landsat and MODIS – Landsat; RMSD is the root mean squared deviation; \bar{x} is the mean and σ is one standard deviation. Ecoregions are the EPA Level 2 ecoregions: AH: Atlantic Highlands; CUP: Central USA Plains; MWP: Mixed Woods Plains; MWS: Mixed Woods Shield; OA: Ozark/Ouachita-Appalachian Forests; TP: Temperate Prairies.	35

Table 2.5 Statistical agreement between the VIIRS LSP and MODIS LCD products with EOS transition dates derived from Landsat in 2013. Bias is calculated as VIIRS – Landsat and MODIS – Landsat; RMSD is the root mean squared deviation; \bar{x} is the mean and σ is one standard deviation. See Table 2.4 for the ecoregions.	36
Table 2.6 Statistical agreement between the VIIRS LSP and MODIS LCD products with phenometrics derived from PhenoCam imagery. n is the number of site-years; Bias is calculated as VIIRS – PhenoCam and MODIS – PhenoCam; RMSD is the root mean squared deviation. See Fig. 2.10 for the vegetation type.	39
Table 4.1 List of AmeriFlux sites. IGBP denotes the International Geosphere-Biosphere Program land cover type classification: CRO: cropland; DBF: deciduous broadleaf forest; ENF: evergreen needleleaf forest; GRA: grassland; MF: mixed forest; SH: shrubland.....	75
Table 4.2 Springtime phenology and changes in biophysical and meteorological properties after leaf emergence.....	85
Table 4.3 The 30-days averaged daytime Bowen ratio before and after springtime phenology and their differences for different vegetation types. Values in parentheses indicate one standard deviation.....	90

LIST OF FIGURES

- Fig. 2.1. Schematic of the algorithms used to create the VIIRS LSP and MODIS LCD products. Panel (a) is a sample of VIIRS EVI2 time series for a single pixel. Panels (b) and (d) illustrate the VIIRS algorithm, while panels (c) and (e) illustrate the MODIS algorithm. 13
- Fig. 2.2. Map of the study area showing three VIIRS and MODIS tiles (H12V04, H11V04, and H08V05), 22 Landsat sidelap regions, and 34 PhenoCam sites used in the analysis. The background image shows the IGBP land cover type across the study area from the Collection 6 MODIS Land Cover Type product in 2013. 15
- Fig. 2.3. Images showing the timing of greenup onset, maturity onset, senescence onset, and dormancy onset (day of year) from the VIIRS LSP and the MODIS LCD products in 2013. Each tile is dominated by different land cover types: forests in the Northeastern U.S. and Eastern Canada (H12V04), croplands in the Central U.S. (H11V04), and shrublands and grasslands in the Southwestern U.S (H08V05). In the columns, VI and MO denote the VIIRS and MODIS products, respectively. 21
- Fig. 2.4. Comparison of phenometrics from the VIIRS LSP and the MODIS LCD products in 2013, stratified by the three most common land cover types in each tile. Red indicates high density and light purple indicates low density of observations. The dashed lines show 1:1 agreement. See caption of Table 2.1 for IGBP class names and statistical summaries for each phenometric. 23
- Fig. 2.5. Comparison of (a) bias and (b) RMSD between phenometrics from the VIIRS LSP and MODIS LCD products from consecutive two years (2013 and 2014). Bias is

calculated as VIIRS – MODIS; RMSD is the root mean squared deviation. Different symbols denote different land cover types in different tiles, and different colors denote different phenometrics. Values in parentheses indicate ± 1 standard deviation. The solid and dashed lines are regression fits and 1:1 lines, respectively. See caption of Table 2.1 for IGBP class names..... 25

Fig. 2.6. NBAR EVI2 time series from VIIRS (diamonds) and MODIS (circles), stratified by the three most common land cover types in each tile during 2013 and 2014. Each dot represents 3-day composites NBAR EVI2 value from each instrument. See caption of Table 2.1 for IGBP class names. 27

Fig. 2.7. Differences in phenometrics from MODIS LCD versus VIIRS LSP derived from differences in input (EVI2 time series) versus algorithms. Panels (a) and (b) illustrate differences in phenometrics arising from different input data, while panels (c) and (d) illustrate differences in phenometrics arising from the different algorithms. Bias represents differences in phenometrics; RMSD is the root mean squared deviation. Values in parentheses indicate ± 1 standard deviation. The solid and dashed lines are the regression and 1:1 lines, respectively. Different shapes denote different land cover types in different tiles and different colors denote different phenometrics. See Fig. 2.5 for symbols and colors legends. 31

Fig. 2.8. Analysis of errors in phenometrics between the VIIRS LSP and MODIS LCD products versus errors introduced by uncertainties in input data. Panels (a) and (b) illustrate errors in phenometrics between the two products versus errors arising from uncertainties in VIIRS and MODIS input data, respectively; panel (c) illustrates

relationship between errors arising from uncertainties in VIIRS and MODIS input data. Values in parentheses in panel (c) indicate ± 1 standard deviation. The solid and dashed lines are the regression and 1:1 lines, respectively. Different shapes denote different land cover types in different tiles and different colors denote different phenometrics. See Fig. 2.5 for symbols and colors legends. 32

Fig. 2.9. Comparison of the VIIRS LSP and MODIS LCD products with phenometrics derived from Landsat in 2013 and 2014. Different colors denote different Landsat sidelaps and different shapes denote different years (circles: 2013; triangles: 2014). Values in parentheses indicate ± 1 standard deviation. The solid and dashed lines are the regression and 1:1 lines, respectively. See Table 2.4 and 2.5 for statistical summaries for each product in each sidelap. 34

Fig. 2.10. Comparison of the VIIRS LSP and MODIS LCD products with phenometrics derived from PhenoCam imagery in 2013 and 2014. SOS and EOS represent the DOY at mid-greenup and mid-down for the VIIRS and MODIS products, respectively. Different colors denote different vegetation types (see panel a) at each PhenoCam site (DB: deciduous broadleaf; EN: evergreen needleleaf; AG: agricultural; GR: grassland; SH: shrubland). Values in parentheses indicate ± 1 standard deviation. The solid and dashed lines are the regression and 1:1 lines, respectively. See Table 2.6 for the statistical agreement between PhenoCam and both VIIRS and MODIS SOS and EOS dates, for each vegetation type. 38

Fig. 2.11. VIIRS and MODIS pixels over the Jasper Ridge PhenoCam site (a), a PhenoCam image and region of interest used to generate G_{CC} time series (b), and time series of

EVI2 from VIIRS, and MODIS, along with G_{CC} from PhenoCam (c). Phenometrics from each time series are shown as vertical lines. In panel (a), the solid and dashed green lines represent a 3 by 3 window and the 500 m pixel centered at the camera's location, respectively; the yellow lines indicate the field of view of the PhenoCam. In panel (b), the yellow box represents the extracted region of interest from PhenoCam imagery. 40

Fig. 3.1. Map of the study area showing the Northern Forest and Eastern Temperate Forest ecoregions defined by the United States Environmental Protection Agency, along with the proportion of deciduous forests in 25 km² grid cells according to the MODIS Land Cover Type product. 52

Fig. 3.2. Model estimates from a randomly selected representative grid cell. Panel (a) shows the relationship between the MODIS onset dates and onset dates estimated by the model; panel (b) shows the distribution of posteriors for each forcing variable; and panel (c) shows the time series of the latent state (red line) and length of pre-season (identified by the horizontal arrow). 58

Fig. 3.3. Geographical pattern of model performance. RMSE is the root-mean square-error between the MODIS onset dates and onset dates from the model estimates. Vertical red line in panel (b) represents the median value (n = 2,018). 59

Fig. 3.4. Geographic sensitivity in the timing of greenup onset to different environmental forcing. Panels (a), (b), and (c) show geographical patterns in the sensitivity of greenup to thermal forcing, day-length, and chilling unit, respectively. In panel (d), the white and grey boxplots show the distribution of sensitivity to each forcing

variable in Eastern Temperate Forests (grey) and Northern Forests (white); note that only day-length shows a statistically significant difference in sensitivity between the two ecoregions ($p < 0.001$). 61

Fig. 3.5. Relative importance of thermal forcing versus day-length. The circles colored in red and blue represent the importance of thermal forcing and day-length, respectively; while the size of circles represents the relative importance of thermal forcing versus day-length (i.e., the bigger the size, the larger the importance). In panel (b), the lines and associated numbers identify the climate space of terrestrial biomes adapted from Gauthier et al. (2015): 1) tropical rain forest; 2) tropical seasonal forest/savanna; 3) subtropical desert; 4) temperate rain forest; 5) temperate seasonal forest; 6) woodland/shrubland; 7) temperate grassland/desert; 8) taiga..... 63

Fig. 3.6. Geographical pattern in pre-season-period (a) and the relationship between pre-season-period and sensitivity to day-length..... 64

Fig. 4.1. Changes in biophysical and meteorological properties 60 days before and after leaf emergence at the Morgan-Monroe State Forest site averaged from 2001 to 2014. $EVI2$, T_s , H , LE , S_{in} , L_{in} , q_a , u , G , r_a , and r_s represent vegetation index, land surface temperature, sensible heat flux, latent heat flux, incoming shortwave radiation, incoming longwave radiation, specific humidity, wind speed, ground heat flux, aerodynamic resistance, and surface resistance, respectively. Dots and lines represent 14-year averaged values and 10-day moving averages, respectively. Vertical dotted lines near 15 days before leaf emergence represent 15% of the seasonal $EVI2$ amplitude. Note that the values are estimated from daytime conditions. 83

Fig. 4.2. Relationship between changes in surface resistance and vegetation index (EVI2). Each point represents the average change for each vegetation type. Changes in EVI2 values are computed based on the average EVI2 value in 3 by 3 MODIS pixel windows centered over each flux tower..... 86

Fig. 4.3. Attribution of the Bowen ratio change after springtime phenology. β_O and β_M are the observed and modeled changes in Bowen ratio, respectively. S_{in} , L_{in} , q_a , T_a , G , r_a , r_s , and α represent contributions from changes in incoming shortwave radiation, incoming longwave radiation, specific humidity, air temperature, ground heat flux, aerodynamic resistance, surface resistance, and albedo, respectively. Different panels present results for different vegetation types. The error bars show one standard deviation from the mean. Note the difference in the scale of the y-axis between panels a-c and panels d-f. 89

Fig. 4.4. Annual patterns in specific humidity (q_a ; red dots and solid lines) and wind speed (u ; blue dots and dashed lines) at the Morgan-Monroe State Forest site measured from a flux tower (a) and at 500 hPa across the northeastern United States from the MERRA reanalysis data (b). Dots and lines represent 10-year averaged values (i.e., from 2001 to 2010) and 30-day moving averages, respectively. Note the values are estimated from daytime conditions. 92

Fig. 4.5. The relationship between changes in wind speed (Δu) and changes in aerodynamic resistance (Δr_a) (a), attribution of changes in aerodynamic resistance (b), and changes in momentum roughness length (Δz_o) (c) at 10 deciduous broadleaf forest sites. Note that the aerodynamic resistance was estimated from sensible heat flux, land surface

temperature, and air temperature; hence Δu and Δr_a are quantified independently from each other. In panel (b), r_{aO} and r_{aM} represent the observed and modeled aerodynamic resistance changes, respectively, and *I*, *II*, and *III* represent contributions from changes in wind speed, atmospheric stability including roughness sublayer corrections, and roughness length (see Eq. 4.13); the error bars show one standard deviation from the mean. 95

LIST OF ABBREVIATIONS

Abbreviation	Definition
AVHRR	Advanced Very High Resolution Radiometer
r_a	Aerodynamic resistance
AI	Agreement index
ρ	Air density
P	Air pressure
T_a	Air temperature
BRDF	Bidirectional reflectance distribution function
β	Bowen ratio
λ	Coefficient in the approximated roughness sublayer correction
μ	Coefficient in the approximated roughness sublayer correction
ν	Coefficient in the approximated roughness sublayer correction
CONUS	Contiguous United States
DOY	Day of year
d	Displacement height
ϵ	emissivity
EOS	End of growing season
g	Gravitational acceleration
G	Ground heat flux
HPLM	Hybrid Piecewise Logistic Model
L_{in}	Incoming longwave radiation
S_{in}	Incoming shortwave radiation
IBM	Intrinsic Biophysical Mechanism
JPSS-1	Joint Polar Satellite System
LCD	Land Cover Dynamics
LSP	Land surface phenology
T_s	Land surface temperature
LPA	Landsat Phenology Algorithm
LE	Latent heat flux
L_v	Latent heat of vaporization
z	Measurement height
MODIS	Moderate Resolution Imaging Spectroradiometer
z_o	Momentum roughness length
NBAR	Nadir BRDF-adjusted reflectance

Abbreviation	Definition
NPP	National Polar-Orbiting Partnership
R_n	Net surface radiation
NDVI	Normalized difference vegetation index
L	Obukhov length
η	Ratio of the gas constants for dry air to water vapor
RMSD	Root-mean-squared difference
$\hat{\Psi}_h$	Roughness sublayer correction function for heat
$\hat{\Psi}_m$	Roughness sublayer correction function for momentum
z_*	Roughness sublayer height above the displacement height
q_s^*	Saturated specific humidity
e^*	Saturation vapor pressure
H	Sensible heat flux
c_p	Specific heat of air
q_a	Specific humidity
Ψ_h	Stability correction function for heat
Ψ_m	Stability correction function for momentum
SOS	Start of growing season
σ	Stefan-Boltzmann constant
α	Surface albedo
r_s	Surface resistance
Φ	surface-layer stability function
MCD12Q2	The MODIS Land Cover Dynamics product
z_{oh}	Thermal roughness length
EVI2	Two-band enhanced vegetation index
TRM	Two-Resistance Mechanism
VIIRS	Visible Infrared Imaging Radiometer Suite
κ	von-Karman constant
u	Wind speed

1. INTRODUCTION

Since the launch of the first Landsat satellite in 1972, space-based observations of the Earth have provided an important new perspective and way to study environmental systems (Melaas et al., 2018; Woodcock et al., 2008). Beginning in the early 1980's, sensors such as the Advanced Very High Resolution Radiometer (AVHRR) have provided daily observations of the global land surface at 1-4 km spatial resolution (Reed et al., 1994). Beginning in the 1980's, atmospheric corrections based on radiative transfer theory became more common, making it possible to obtain land surface reflectances from these measurements and providing geophysical and ecologically meaningful measurements that can be analyzed across both time and space. Simple transformations of surface reflectances (i.e., vegetation indices) were subsequently shown to be correlated with the biophysical and biochemical properties of plants (Huete, 1988; Myneni et al., 1997; Sellers, 1985; Tucker, 1979). By leveraging these developments and applying them to time series of vegetation indices such as the normalized difference vegetation index (NDVI), numerous studies have revealed widespread changes in terrestrial ecosystems over the last three decades related to both human activity and climate change (Hansen et al., 2013; Myneni et al., 1997; Park et al., 2016; Sulla-Menashe et al., 2018).

The growing quality and size of remote sensing archives, in combination with continuously evolving climate and vegetation models have provided valuable opportunities to pose and test hypothesis related to how climate interacts with the biosphere, and vice versa. For example, Piao et al. (2008) evaluated whether or not longer growing seasons induced by warmer spring and autumn temperatures enhances carbon sequestration, and,

by extending the period of net carbon uptake, will enhance carbon sequestration in the coming decades. To do this, they used eddy covariance measurements in combination with a state-of-the-art ecosystem model and time series of vegetation index data from the AVHRR. Their results suggested that warming acted to enhance net ecosystem productivity in spring by increasing photosynthesis more than respiration. In contrast, net productivity decreased in autumn because increases in respiration acted to offset increased photosynthesis and end-of-season moisture stressed acted to reduce photosynthesis. They concluded that if future autumn warming occurs at a faster rate than future warming in springtime, the ability of northern ecosystems to sequester carbon will be less than previously suggested. More generally, the results of Piao et al. (2008) demonstrated complex and unexpected interactions between phenology, climate change and ecosystem productivity that had previously not been considered.

A key limitation of the study by Piao et al. (and others) is the quality of satellite data they used. Specifically, time series of NDVI measurements derived from the AVHRR have substantial limitations related to their coarse spatial resolution, low quality snow and cloud detection, uncertainty in radiometric calibration, and errors in geolocation (Gutman, 1999; Ju and Masek, 2016a; Nagol et al., 2009; Sulla-Menashe et al., 2018; White et al., 2009). In an analysis comparing AVHRR NDVI time series with the time series of NDVI from NASA's Moderate Resolution Imaging Spectroradiometer (MODIS), Fensholt and Proud (2012) identified large differences in long-term NDVI trends from each instrument, especially at high latitude regions. Ju and Masek (2016) reported similar differences in NDVI trends from Landsat versus AVHRR over high latitudes. Despite this, NDVI time

series from AVHRR continue to be widely used because they provide global observations that span more than three decades.

In addition to studies focused on so-called greening and browning trends, a large literature has emerged over the last two decades focused on using measurements of vegetation phenology as a key diagnostic indicator of climate change impacts on ecosystem properties and processes (Richardson et al., 2013), much of it leveraging remote sensing. In addition to providing valuable information related to the nature and magnitude of growing season changes, green leaf phenology regulates several important surface biophysical properties and processes including land surface albedo (Moore et al., 1996a; Ollinger et al., 2008), surface energy budgets (Dorman & Sellers, 1989; Ryu et al., 2008), the partitioning of surface radiation between latent and sensible heat fluxes (Hogg et al., 2000; Schwartz, 1992), and aerodynamic and surface resistances (Blanken & Black, 2004; Zhao et al., 2016). Hence, accurate representation of spatiotemporal dynamics in vegetation phenology is important for a variety of topics in both basic and applied ecological sciences ranging from monitoring the impact of climate change on species and communities, to modeling seasonal variation in ecosystem processes (Chen et al., 2016; Menzel et al., 2006; Peñuelas et al., 2009; Richardson et al., 2010).

1.1. Land surface phenology from satellite remote sensing

Prior to the era of Earth observation satellites, observations of vegetation phenology were collected via field surveys, which recorded the timing of discrete phenological events for individual species, such as flowering and leaf emergence in spring and leaf coloration

and leaf drop in fall (e.g., Caprio, 1957). These data continue to be collected and have substantial value. However, because field surveys generally focus on a limited set of plants and species at local scales, generalizing and upscaling results from field data (e.g., to the scale of entire biomes) is challenging. In the last several decades, satellite remote sensing has been shown to provide a powerful complement to field observations that can be used to monitor and characterize the nature, magnitude, and timing of changes in land surface phenology at regional to global scales. Because of its 30+ year record of measurements, the AVHRR time series of NDVI have been widely used for this purpose (Buitenwerf et al., 2015; Dardel et al., 2014; de Beurs and Henebry, 2005; Fang et al., 2001; Fensholt and Rasmussen, 2011; Guay et al., 2014).

However, as I described previously, the coarse spatial resolution of AVHRR data, in combination with uncertainty in radiometric calibration, low quality snow and cloud detection, broad spectral channels, and errors in geolocation introduce considerable uncertainty to time series of vegetation indices and phenological metrics derived from this instrument (Gutman, 1999; Ju & Masek, 2016; Nagol et al., 2009; Sulla-Menashe et al., 2018; White et al., 2009). With the launch of MODIS on-board the NASA's Terra spacecraft in 1999, the remote sensing and global change community were provided with newer, higher spatial resolution imagery specifically designed for land applications with dramatically improved radiometric and geometric properties relative to AVHRR imagery. Twenty years later, the MODIS record provides a new foundation for ongoing long-term monitoring of continental to global-scale remote sensing of terrestrial ecosystems and land surface phenology. Moving forward, the Visible Infrared Imaging Radiometer Suite

(VIIRS) onboard the Joint Polar Satellite System is designed to provide continuity with MODIS for decades to come. However, despite substantial similarities between both the instruments and data sets being generated by MODIS and VIIRS, significant differences exist. Hence, it's important to evaluate the viability and issues surrounding the use of VIIRS in combination with MODIS as a basis for long term studies of terrestrial ecosystem change.

1.2. Climate controls on land surface phenology

The timing of leaf emergence and growth is affected by multiple environmental controls whose relative influence varies across species and regions (Lechowicz, 1984). Three cues are widely understood to be primarily responsible for triggering spring phenology: spring warming, day length (i.e., photoperiod), and winter chilling. Spring warming is the most obvious cue for springtime phenological events, and many studies have identified multi-decadal trends toward earlier spring onset of budburst and leaf emergence arising from large-scale warming patterns (Cleland et al., 2007; Doi and Katano, 2008; Keenan et al., 2014; Menzel et al., 2006; Parmesan and Yohe, 2003; Piao et al., 2006; Yue et al., 2015).

While most studies and models have focused on the role of temperature in spring phenology, photoperiod and chilling are widely viewed to be “safety mechanisms” that prevent early onset, thereby avoiding physical damage induced by frost events that affect plant growth as well as carbon and nutrient cycles (Augspurger, 2009; Hufkens et al., 2012; Inouye, 2008; Liu et al., 2018). Given these controls, a key question that has emerged in

the phenology research community is whether or not temperature-driven trends in vegetation phenology will continue under ongoing warming, or whether these safety mechanisms will constrain the impact of warmer temperatures (Fu et al., 2015; Liu et al., 2017; Melaas et al., 2018; Park et al., 2018; Piao et al., 2017; Richardson et al., 2018a; Vitasse et al., 2011; Zohner et al., 2016). This topic is currently an active and open area of research for which time series of remotely sensed phenological information provides an important basis of investigation.

1.3. Vegetation phenology feedbacks on land-atmosphere interaction

It has long been known that vegetation influences weather and climate (Sellers et al., 1997) and that phenology plays an important role in regulating interactions between the land surface and the atmosphere (Richardson et al., 2013). Specifically, vegetation phenology regulates seasonal variation in mass and energy exchange between terrestrial ecosystems and the atmosphere by modifying surface biophysical properties and processes including land surface albedo (Moore et al., 1996; Ollinger et al., 2008), aerodynamic and surface resistances (Blanken and Black, 2004; Zhao et al., 2016), and the partitioning of available energy into latent and sensible heat fluxes (Hogg et al., 2000; Schwartz, 1992). At the same time, vegetation phenology also affects a number of atmospheric properties and processes including daily air temperature range (Schwartz, 1996), cloud formation (Freedman et al., 2001), and precipitation (Zhang et al., 2005). Therefore, understanding the role of vegetation phenology in land-atmosphere interactions is essential to improving weather and climate models, and to understanding how ecosystems will respond to and

affect future climate change (Peñuelas et al., 2009; Pielke et al., 1998; Richardson et al., 2013; Wilson and Baldocchi, 2000). To date, the vast majority of research in this area has focused on one-way forcing and interactions; i.e., the role of springtime changes in atmospheric properties on vegetation phenology and associated energy balance processes. As a result, questions focused on dynamical interactions and feedbacks between land surface energy balance and the atmosphere that arise from phenological processes has been understudied and is poorly understood.

1.4. Research objectives and questions

With the issues and background discussed above as context, the overarching goal of my dissertation research is to use contemporary and historical remote sensing data in combination with climate and ecological data to improve understanding of how terrestrial ecosystems are changing. In particular, my dissertation examines questions related to: (1) the viability of using time series of vegetation indices from MODIS and VIIRS to create fused time series of land surface phenology measurements in support of long-term phenological trend analyses; (2) how different environmental controls interact with each other and influence the timing of spring greenup from remote sensing; and (3) how springtime vegetation phenology and atmospheric properties interact in ways that influence the timing and magnitude land surface fluxes of moisture and heat to the atmosphere. To address these questions, my dissertation includes three main elements.

In the first chapter, I conduct a comprehensive evaluation of the newly available Collection 6 MODIS Land Cover Dynamics (LCD) product by performing a comparative

assessment of LCD data sets with corresponding metrics from the VIIRS Land Surface Phenology product. The results from this chapter provide guidance regarding the utility of combined time series from VIIRS and MODIS to address questions related to long-term changes in phenology arising from climate change. In the second chapter, I use the MODIS LCD product, phenological models, and climate data to characterize and quantify how each of the key phenological controls identified above (i.e., thermal forcing, day-length, and winter chilling) control the timing of springtime phenology and explore how these controls vary geographically over large areas. In the third chapter, I present a physically-based method that captures first-order interactions between land surface phenology and surface energy balance, and then apply this method to examine relationships among changes in surface energy balance, springtime phenology, and land-atmosphere feedbacks. I conclude my dissertation with a summary of key results and a discussion of future research directions.

2. LONG-TERM CONTINUITY IN LAND SURFACE PHENOLOGY MEASUREMENTS: A COMPARATIVE ASSESSMENT OF THE MODIS LAND COVER DYNAMICS AND VIIRS LAND SURFACE PHENOLOGY PRODUCTS

2.1. Introduction

The Moderate Resolution Imaging Spectroradiometer (MODIS) onboard NASA's Terra (since 1999) and Aqua (since 2002) platforms have provided high quality global imagery at 250, 500, and 1 km spatial resolution that is well-suited for retrieving land surface phenology (Ganguly et al., 2010; Zhang et al., 2003). In particular, the MODIS LCD product (MCD12Q2) provides annual measurements of global land surface phenology at 500 m spatial resolution and has been successfully used to explore a variety of climate-ecosystem relationships at large spatial scales (Friedl et al., 2014; Hufkens et al., 2012; Keenan et al., 2014; Zhang et al., 2004). However, the MODIS sensors are well-beyond their original design life and are expected to cease operation in the coming years. To provide continuity with both MODIS and AVHRR, the Visible Infrared Imaging Radiometer Suite (VIIRS) was launched in October 2011 as a part of the instrument suite onboard the Suomi National Polar-Orbiting Partnership (NPP). With the launch of the first Joint Polar Satellite System (JPSS-1) in November of 2017, VIIRS provides the operational basis for long-term continuity of the MODIS land product suite (Justice et al., 2013). In support of this vision, a new operational land surface phenology (LSP) product has been developed based on VIIRS data (Zhang et al., 2018b) and is designed to provide long-term continuity with the MODIS LCD product.

Because the VIIRS LSP and MODIS LCD products are derived from different instruments and are based on different algorithms, differences in the data products are unavoidable. To evaluate the similarities and differences between these two data products and, more specifically, to address the question of whether the VIIRS product provides continuity with the MODIS product for long-term studies of land surface phenology, here I present a systematic comparison of the Collection 6 MODIS LCD product (Gray et al., 2020) and the newly developed VIIRS LSP product (Zhang et al., 2018b). Several studies have previously examined correspondence between satellite-based LSP metrics and both in-situ measurements of phenology (Ganguly et al., 2010; Liang et al., 2011; Zhang et al., 2006) and other proxies of vegetation phenology such as time series of gross primary productivity derived from flux networks (Melaas et al., 2013a; Park et al., 2016; Sakamoto et al., 2010). Preliminary assessment of the overall accuracy of the VIIRS LSP product is presented elsewhere (Zhang et al., 2017b, 2018a). Here I focus on a product-to-product comparison, and specifically address the question of whether the VIIRS and MODIS products can be used jointly for studies that require time series of land surface phenology measurements. To do this, I systematically compare the operational VIIRS LSP and MODIS LCD products across the Contiguous United States (CONUS) and Eastern Canada, focusing on three sub-regions that span a wide range of climate and land cover types in the Northeastern United States, Eastern Canada, the Central U.S, and the Southwestern U.S. My analysis includes three elements. First, I assess the agreement between phenophase transition metrics (hereafter, phenometrics; e.g., the timing of greenness increase onset) from each product. Second, I conduct a comprehensive evaluation to attribute differences

between the two products to (1) differences in MODIS versus VIIRS input data and their associated quality, and (2) differences in the algorithm used to generate each product. Third, I conduct a multi-scale comparison of the MODIS LCD and VIIRS LSP products against phenometrics derived from Landsat (Melaas et al., 2016b) and from the PhenoCam Dataset V1.0 (Richardson et al., 2018a).

2.2. Data and Methods

2.2.1. Overview of land surface phenology product algorithms

To provide context for the analyses and results I describe below, I first provide an overview of the MODIS LCD and VIIRS LSP products, focusing on their primary similarities and differences. Specifically, there are three main steps in each land surface phenology algorithm: (1) preprocessing of vegetation index time series to remove spurious values, (2) time series smoothing or model fitting to create continuous time series without gaps, and (3) identification of phenometrics (Fig. 2.1). Space does not allow for a complete description of each algorithm. For more detailed information, please see Zhang et al. (2018b) and Gray et al. (2019).

Both products use daily nadir bidirectional reflectance distribution function (BRDF)-adjusted reflectance (NBAR) products (VNP43IA4 for VIIRS and MCD43A4 for MODIS) to compute time series of the two-band enhanced vegetation index (EVI2; Jiang et al., 2008) at each pixel, which serves as the primary input to both algorithms (Fig. 2.1a). Note that the MODIS NBAR product is produced using MODIS observations from both Terra and Aqua; whereas, the VIIRS NBAR product is generated using VIIRS observations

only from Suomi NPP. Spurious EVI2 values caused by snow-contamination are replaced by “background values”, which represent the minimum snow-free EVI2 at each pixel (Zhang et al., 2006). To reduce data volumes, daily NBAR data are sampled every 3 days in the VIIRS LSP algorithm, while in the MODIS LCD algorithm daily NBAR data are sampled every 5 days. Both products use snow flags included as part of the NBAR product (VNP43IA2 for VIIRS and MCD43A2 for MODIS) from each instrument to identify snow-contaminated values. The VIIRS product also uses land surface temperature as an additional constraint (Zhang et al., 2018b), while the MODIS product uses the normalized-difference snow index (NDSI) to flag snow-contaminated pixels (Gray et al., 2020).

To create smooth and gap-filled data, the VIIRS LSP algorithm first applies a Savitzky-Golay filter to EVI2 time series. A hybrid piecewise logistic model (HPLM) is then fit to the smoothed time series at each pixel (Fig. 2.1b). New in Collection 6, the MODIS LCD algorithm removes outliers and generates smoothed EVI2 time series in a single step using penalized cubic splines (Fig. 2.1c). For the VIIRS LSP, phenometrics are identified using the rate of change in curvature of the fitted HPLM; whereas, the MODIS LCD approach uses prescribed thresholds in the amplitude of variation in EVI2 for each phenological cycle (Fig. 2.1d and 2.1e, respectively). In the VIIRS LSP algorithm two local maxima in the rate of change of curvature during the “green-up” phase are used to identify phenometrics. Specifically, the day of year (DOY) corresponding to each of these maxima identifies the timing of greenup and maturity onset, and the date corresponding to the minimum rate of change in the curvature corresponds to the DOY when EVI2 reaches 50% of its seasonal amplitude. For the MODIS product, the timing of greenup onset, mid-

greenup, and maturity onset are retrieved as the DOY when the splined EVI2 time series first crosses 15%, 50%, and 90% of its seasonal amplitude, respectively. In both products, corresponding phenometrics during senescence, or “green-down” (i.e., senescence onset, mid-senescence, and dormancy onset) are identified in a similar manner.

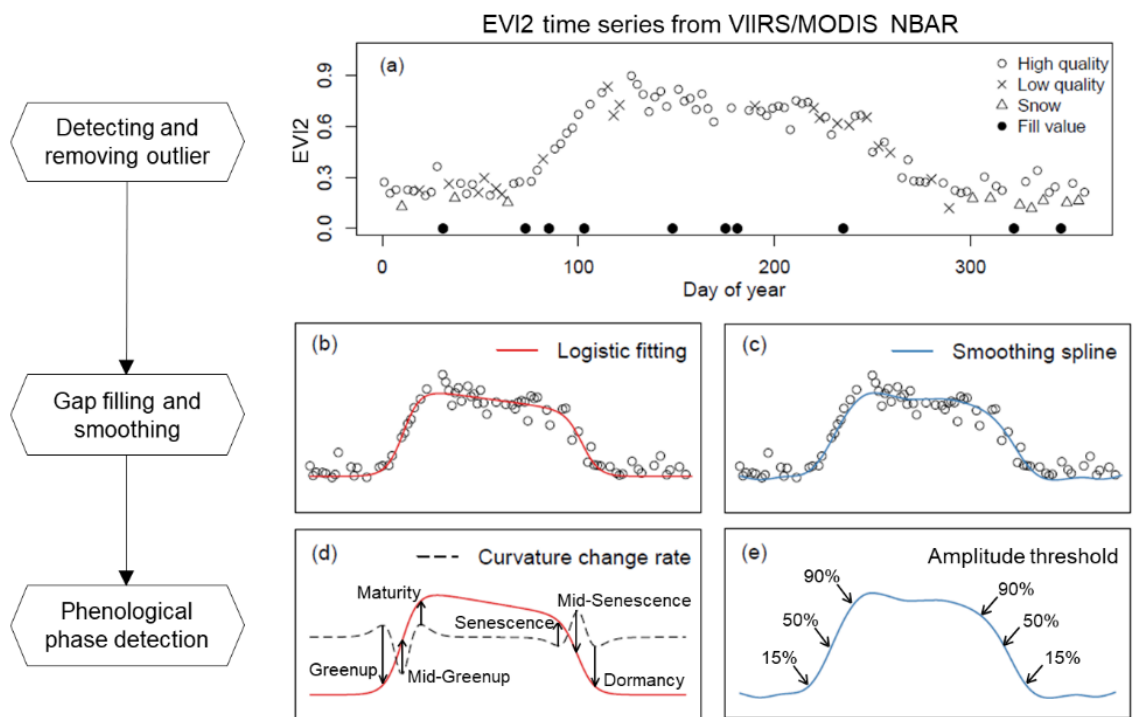


Fig. 2.1. Schematic of the algorithms used to create the VIIRS LSP and MODIS LCD products. Panel (a) is a sample of VIIRS EVI2 time series for a single pixel. Panels (b) and (d) illustrate the VIIRS algorithm, while panels (c) and (e) illustrate the MODIS algorithm.

2.2.2. Intercomparison of land surface phenology products

To compare the two products, I use a stratified random sample of pixels located in three 10° by 10° tiles in North America that encompass a wide range of climate and land

cover types (tiles H12V04, H11V04, and H08V05; Fig. 2.2). In each tile, I identify the three dominant vegetated land cover types based on the Collection 6 MODIS Land Cover Type product (MCD12Q1; Sulla-Menashe et al., 2019). Note, however, that for tile H08V05 (centered over the arid southwestern United States), pixels belonging to the Barren or Sparsely Vegetated class in the MCD12Q1 product, which are defined as having less than 10% vegetation cover, were excluded from the evaluation. Previous work has shown that discrepancies between phenometrics derived from VIIRS and MODIS are often associated with the low quality of EVI2 time series (Zhang et al., 2018b). Thus, I exclude pixels where differences in phenometric values between the two products were unusually large (viz., > 90 days). This step resulted in 0-4% of pixels from the original sample being removed from each land cover type in each of the tiles for each phenometric. Finally, prior to performing my assessment, I apply a 3×3 moving window median filter to each phenometric in each product to account for the fact that the effective spatial resolutions of NBAR data are greater than 500 m and are different for each sensor ($\sim 565 \text{ m} \times 595 \text{ m}$ and $833 \text{ m} \times 618 \text{ m}$ in the VIIRS and MODIS NBAR products, respectively; Campagnolo et al., 2016).

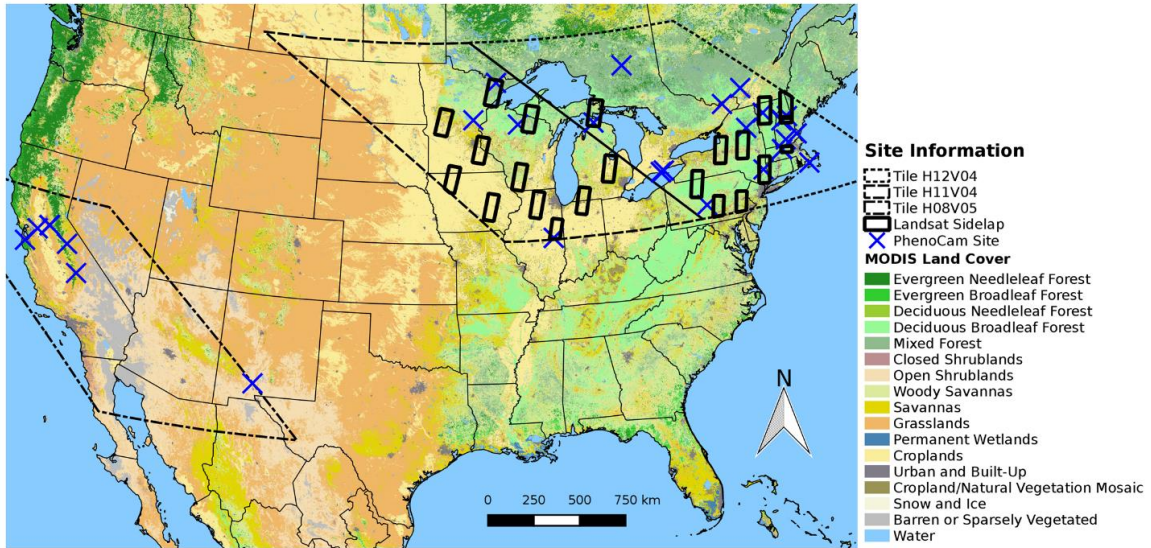


Fig. 2.2. Map of the study area showing three VIIRS and MODIS tiles (H12V04, H11V04, and H08V05), 22 Landsat sidelap regions, and 34 PhenoCam sites used in the analysis. The background image shows the IGBP land cover type across the study area from the Collection 6 MODIS Land Cover Type product in 2013.

2.2.3. Attribution of differences related to sensors versus algorithms

To evaluate and attribute sources of differences between the two products, I perform three sets of analyses. First, because differences in EVI2 time series derived from MODIS versus VIIRS are an obvious source of disagreement, I evaluate the overall agreement and quality of model fits to VIIRS and MODIS NBAR EIV2 time series. To do this, I use a randomly selected set of 10,000 pixels from each of the three dominant land cover types in each of the three tiles included in my analysis. To quantify the agreement between observations and fitted time series, I calculate the growing season agreement index (AI) for all pixels as defined by Zhang et al, (2018b):

$$AI = 100 - 100 \frac{\sum_{i=0}^n (P_{(i)} - O_{(i)})^2}{\sum_{i=0}^n (|P_{(i)} - \bar{O}| + |O_{(i)} - \bar{O}|)^2} \quad (2.1)$$

where n is the number of observations, $P_{(i)}$ is the modeled value for the i^{th} observation, $O_{(i)}$ is the EVI2 for the i^{th} observation, and \bar{O} is the mean EVI2 across the time series at each pixel. The VIIRS and MODIS products use 3-day and 5-day composites, respectively, to reduce data volumes and noise in EVI2 time series. However, because the purpose of this analysis is to compare the quality of input data for both products, I apply the same criteria for both sources of EVI2 data. Specifically, I use 3-day composited EVI2 values from both MODIS and VIIRS in 2013, selecting either the best quality EVI2 value or the maximum value composite, if more than one high quality value was available in each 3-day period.

Second, I assess how differences in both input data and algorithms introduce differences in phenometrics from each of the two products. To account for differences in input data, I estimated phenometrics from VIIRS and MODIS NBAR EVI2 time series using the VIIRS LSP algorithm and compared the resulting phenometrics. Then, to assess the contribution of using different algorithms, I apply both VIIRS LSP and MODIS LCD algorithms to MODIS NBAR EVI2 time series. Note that I use MODIS data for this analysis because MODIS EVI2 time series are less noisy than corresponding time series from VIIRS (see Results section), thereby minimizing differences caused by noise in input data.

Third, to provide an assessment of how data-induced uncertainties impact phenometrics, I perform a statistical simulation experiment wherein EVI2 time series and noise were simulated and used to estimate phenometrics. To do this, I first fit logistic

models to EVI2 time series and retained the model residuals. I then treat the modeled EVI2 time series as truth and the model residuals as instrument-induced errors, generated simulated EVI2 time series using non-parametric bootstrapping (Efron, 1979), and estimated phenometrics from the simulated EVI2 time series. To do this, I use the same data set of 10,000 randomly selected pixels from each land cover type in each of the tiles described above.

2.2.4. Comparison with results from the Landsat Phenology Algorithm

I use results from the Landsat Phenology Algorithm (LPA) described by Melaas et al. (2013, 2016) to provide an independent source of land surface phenology information that could be compared with VIIRS LSP and MODIS LCD results. The LPA exploits the temporal density of observations available in overlap regions between adjacent Landsat scenes (hereafter, “sidelaps”), and provides estimates of the DOY associated with the start and end of the growing season (SOS and EOS, respectively) at 30 m spatial resolution that are equivalent to the mid-greenup and mid-senescence dates from VIIRS and MODIS (Fig. 2.1). Comparison of LPA results against local-scale in-situ measurements indicate the LPA provides high quality estimates of SOS and EOS, especially for SOS (Melaas et al., 2016b).

For this analysis, I generate LPA results using USGS Landsat Analysis Ready Data in 22 sidelaps distributed across the Central and Northeastern U.S (Fig. 2.2) in 2013 and 2014. This data set includes Landsat 8 imagery, which increases data density, and the LPA implementation used here incorporates the topographic correction described by Tan et al. (2013), which is important in regions where topographically-induced variation in Landsat

surface reflectance affects LPA results (E. Melaas, pers. comm.). For each sidalap, corresponding values for mid-greenup and mid-senescence dates from the VIIRS LSP and MODIS LCD products were extracted, and data from all three sources were up-scaled to 1500 m spatial resolution (i.e., 3×3 500 m pixel windows) using the mean of all available 30 m LPA retrievals and the median of VIIRS LSP and MODIS LCD values in each 1500 m cell. To minimize deviations caused by missing data in LPA retrievals (e.g., caused by clouds), I excluded all 1500 m cells where fewer than 100 LPA SOS or EOS values out of ~ 2500 pixels were available. To explore how results varied as a function of geographic variation in ecological conditions, I stratify my analysis based on the EPA level II ecoregions (Omernik, 1987; Omernik and Griffith, 2014).

2.2.5. Comparison with phenometrics from the PhenoCam Dataset V1.0

To provide a second source of independent assessment data, I use phenometrics estimated using time series of PhenoCam imagery. PhenoCam is a continental-scale network that uses near-surface imagery from digital cameras to track vegetation phenology at high temporal resolution (Richardson et al., 2018a). The PhenoCam Dataset V1.0 (Richardson et al., 2018a) includes about 750 site-years of observations that characterize vegetation phenology in all major ecosystems across North America. For this work, I use all PhenoCam site-years for which corresponding VIIRS and MODIS phenometrics are available, again focusing on the date of mid-greenup and mid-senescence. More specifically, I use phenometrics derived from Green Chromatic Coordinate (G_{CC} ; Sonnentag et al., 2012) time series corresponding to the date when G_{CC} values reach 50%

of their seasonal amplitude during the greenup and green-down periods for each site-year. For this comparison, I only use data from the sites where the vegetation type of the region of interest in PhenoCam imagery corresponded to the MODIS land cover type surrounding the PhenoCam site. Specifically, sites where more than 5 pixels within 3×3 500 m windows centered over the site had land cover labels that were different from the PhenoCam vegetation type were excluded from the analysis. The resulting data set include 34 sites and a total 109 phenometrics (53 and 56 site-years for SOS and EOS, respectively; Table A1). In addition, to illustrate some of the challenges associated with comparison of results from data streams with such different spatial resolutions, I also present a comparison of G_{CC} and EVI2 time series (and corresponding phenometrics) at the Jasper Ridge PhenoCam site.

2.3. Results

2.3.1. Baseline comparison of the VIIRS LSP and MODIS LCD products

To evaluate the overall agreement between the VIIRS LSP and MODIS LCD products, Fig. 2.3 shows maps of phenometrics derived from the VIIRS LSP and MODIS LCD products in 2013 for each of the three tiles included in my analysis. Table 2.1 presents statistics summarizing the agreement between phenometrics derived from each product (stratified by land cover type). Fig. 2.4 shows scatterplots illustrating agreement between phenometrics for the two products. Fig. 2.5 presents year-to-year agreement from 2013 to 2014 in the bias and the root-mean-squared difference (RMSD) between VIIRS LSP and MODIS LCD phenometrics. Overall, results indicate that phenometrics are in close

agreement across land cover types, with phenometrics corresponding to the mid-point in the green-up and green-down periods (mid-greenup and mid-senescence) showing the strongest agreement. The maximum difference in mean phenometrics is less than two weeks in woody savannas in temperate regions (cf., tiles H12V04 and H11V04). In general, however, mean values across the study region and all six phenometrics show differences that were less than one week, with slightly larger differences during green-down (i.e., senescence onset, mid-senescence, and dormancy onset) than during green-up. RMSDs and bias between phenometrics from the MODIS LCD and VIIRS LSP products are consistent across products, and showed no systematic patterns of deviation as a function of location (tile) or land cover type.

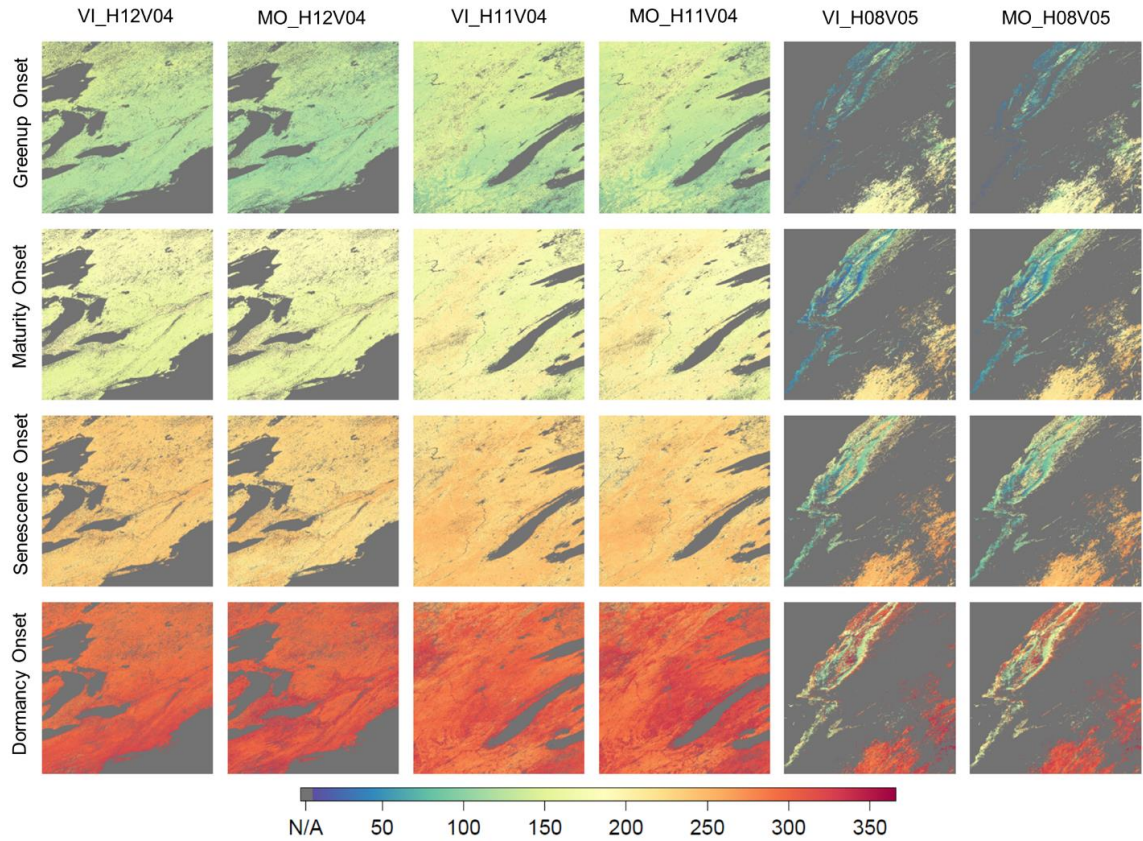


Fig. 2.3. Images showing the timing of greenup onset, maturity onset, senescence onset, and dormancy onset (day of year) from the VIIRS LSP and the MODIS LCD products in 2013. Each tile is dominated by different land cover types: forests in the Northeastern U.S. and Eastern Canada (H12V04), croplands in the Central U.S. (H11V04), and shrublands and grasslands in the Southwestern U.S. (H08V05). In the columns, VI and MO denote the VIIRS and MODIS products, respectively.

Table 2.1 Summary statistics (mean, \bar{x} , and standard deviation, σ) for each tile, stratified by the three dominant land cover types from Fig. 2.3, excluding barren and sparsely vegetated pixels. IGBP land cover was derived from the Collection 6 MODIS Land Cover Type product: 4: deciduous broadleaf forests; 5: mixed forests; 7: open shrublands; 8: woody savannas; 9: savannas; 10: grasslands; 12: croplands.

Tile ID	IGBP	%	Product	Greenup Onset		Date at mid-Greenup		Maturity Onset		Senescence Onset		Date at mid-Senescence		Dormancy Onset	
				\bar{x}	σ	\bar{x}	σ	\bar{x}	σ	\bar{x}	σ	\bar{x}	σ	\bar{x}	σ
Forests	5	32	VIIRS	131	12	152	10	173	12	232	12	260	8	289	11
			MODIS	122	12	149	9	174	9	223	10	264	6	294	14
	4	26	VIIRS	123	10	140	8	157	10	230	10	266	8	301	13
			MODIS	116	9	137	7	160	8	218	11	270	6	298	10
	8	20	VIIRS	126	15	145	14	166	16	232	12	266	11	300	16
			MODIS	113	14	139	13	168	15	225	13	274	10	309	14
Croplands	12	53	VIIRS	137	19	164	15	191	16	234	14	262	14	292	20
			MODIS	139	20	167	16	194	13	232	13	262	15	297	20
	8	11	VIIRS	129	14	148	12	168	13	228	13	264	11	300	15
			MODIS	121	13	144	11	171	12	225	12	275	10	310	14
	4	8	VIIRS	131	11	147	9	164	10	228	11	263	9	298	14
			MODIS	125	10	145	9	168	9	221	10	271	7	300	10
Shrublands/ Grasslands	7	33	VIIRS	181	34	199	28	211	42	246	40	273	41	301	43
			MODIS	180	38	202	28	215	41	244	41	269	40	304	38
	10	22	VIIRS	153	57	172	52	146	83	184	82	211	84	240	89
			MODIS	153	57	175	53	152	81	181	80	208	81	244	83
	9	7	VIIRS	131	59	150	56	151	66	199	64	231	63	266	65
			MODIS	126	56	153	56	156	64	191	63	224	62	274	52

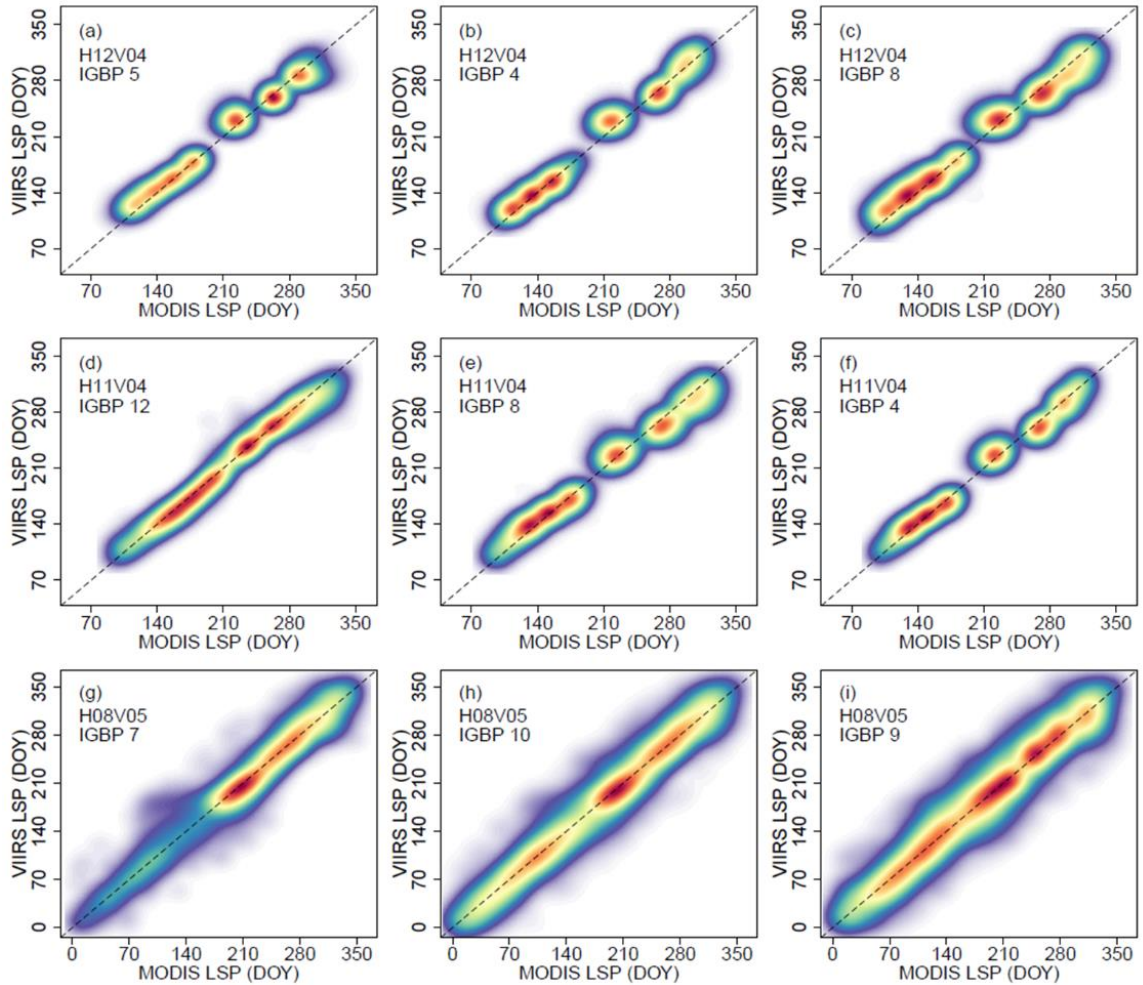


Fig. 2.4. Comparison of phenometrics from the VIIRS LSP and the MODIS LCD products in 2013, stratified by the three most common land cover types in each tile. Red indicates high density and light purple indicates low density of observations. The dashed lines show 1:1 agreement. See caption of Table 2.1 for IGBP class names and statistical summaries for each phenometric.

Table 2.2 Statistical agreement between the VIIRS LSP and MODIS LCD products in 2013. IGBP denotes land cover type. Bias is calculated as VIIRS – MODIS; RMSD is the root mean squared deviation. See caption of Table 2.1 for IGBP class names.

Tile ID	IGBP	Greenup		Date at mid-Greenup		Maturity Onset		Senescence Onset		Date at mid-Senescence		Dormancy Onset	
		Bias	RMSD	Bias	RMSD	Bias	RMSD	Bias	RMSD	Bias	RMSD	Bias	RMSD
Forests	5	8.9	11.2	3.1	5.3	-1.5	5.4	8.9	12.1	-4.1	6.8	-4.7	11.0
	4	6.8	8.7	2.4	3.8	-2.7	4.9	12.4	15.0	-4.3	6.4	2.8	9.1
	8	12.2	14.5	6.3	8.2	-2.2	5.8	7.6	12.1	-8.3	11.1	-8.3	14.2
Croplands	12	-1.3	6.7	-2.8	6.0	-3.3	5.6	2.3	5.8	0.6	7.1	-4.8	11.3
	8	8.0	10.2	4.4	6.0	-3.1	6.2	3.8	9.6	-10.4	13.1	-9.0	14.4
	4	5.7	7.5	2.2	3.8	-3.7	5.7	6.0	9.8	-8.8	10.4	-2.3	8.7
Shrublands/ Grasslands	7	-0.1	19.1	-3.6	11.3	-4.6	10.2	3.1	12.2	4.9	12.5	0.2	16.4
	10	-0.3	16.5	-3.1	11.6	-5.7	10.7	4.9	13.7	4.6	12.9	-1.7	16.6
	9	3.6	18.1	-2.4	12.5	-5.4	12.3	10.1	18.6	7.4	17.6	-4.5	21.6

Systematic differences between the two products (i.e., bias: VIIRS - MODIS phenometrics) are generally less than one week (absolute bias 4.8 ± 3.0 days; mean \pm one standard deviation), and root mean square deviations (RMSDs) are less than two weeks for most phenometrics across land cover classes (10.7 ± 4.3 days) (Table 2.2). At the same time, modest systematic biases are clearly evident for some phenometrics. For example, mean values for maturity onset from VIIRS are systematically earlier than those from MODIS (-3.6 ± 1.4 days). Similarly, mean senescence onset dates are later for VIIRS than for MODIS (6.6 ± 3.4 days). Moreover, dormancy onset dates from VIIRS are earlier than from MODIS in forest- and cropland-dominated tiles (-4.4 ± 4.3 days). The largest biases are located in woody savannas and were associated with earlier greenup and later dormancy in the MODIS LCD product (12.2 and 8.0 days earlier and 8.3 and 9.0 days later for the forest and croplands tiles, respectively). Semi-arid land cover types (viz., shrublands,

grasslands, and savannas) showed modest levels of disagreement across products (*i.e.*, higher RMSDs; 14.7 ± 3.4 days), reflecting higher variation and uncertainty in land surface phenology in semi-arid land cover types that are characterized by low seasonal amplitude in EVI2. Overall, however, agreement is high and bias is low between phenometrics for the two products. In addition, bias and RMSDs between the products across two consecutive years (2013 and 2014) are consistent across land cover types in each of the tiles (Fig. 2.5).

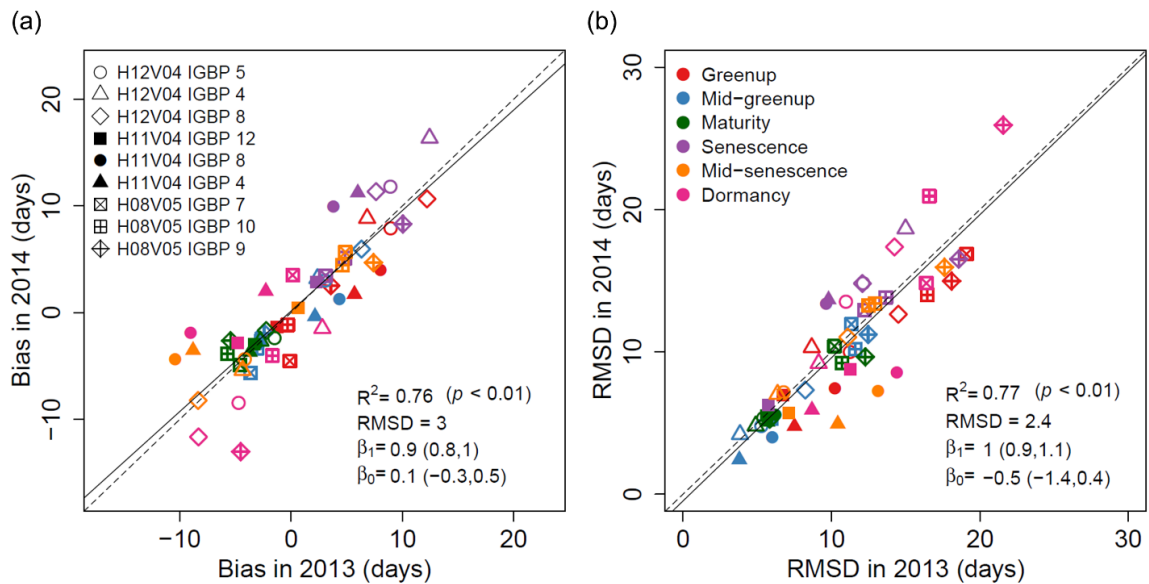


Fig. 2.5. Comparison of (a) bias and (b) RMSD between phenometrics from the VIIRS LSP and MODIS LCD products from consecutive two years (2013 and 2014). Bias is calculated as VIIRS – MODIS; RMSD is the root mean squared deviation. Different symbols denote different land cover types in different tiles, and different colors denote different phenometrics. Values in parentheses indicate ± 1 standard deviation. The solid and dashed lines are regression fits and 1:1 lines, respectively. See caption of Table 2.1 for IGBP class names.

2.3.2. Analysis and attribution of differences across products

Comparison of time series derived from VIIRS and MODIS clearly shows that EVI2 time series from each instrument are highly similar, but that MODIS EVI2 time series are smoother and have less high frequency noise relative to VIIRS EVI2 time series. To illustrate, Fig. 2.6 presents representative EVI2 time series from each sensor for a single pixel from each of six land cover classes. To provide a more comprehensive and quantitative assessment, Table 2.3 shows results for linear regressions between MODIS and VIIRS EVI2 times series (where MODIS EVI2 is the independent variable in each linear regression), along with the agreement index (AI) for spline and double-logistic model fits to MODIS and VIIRS EVI2 time series (respectively), based on a sample of 10,000 pixels stratified by land cover type from each tile. The estimated regression models have slopes that range from 0.986 to 1.051, intercepts that range from -0.004 to 0.012, and RMSDs range from 0.020 to 0.062, which demonstrate that the EVI2 time series from MODIS and VIIRS are highly comparable with no significant biases. However, estimated AI values for penalized cubic splines fit to MODIS EVI2 time series have slightly higher agreement than double logistic functions fit to VIIRS EVI2 time series, which reflects the greater flexibility of cubic splines relative to logistic functions, in combination with modestly higher noise levels in EVI2 data from VIIRS.

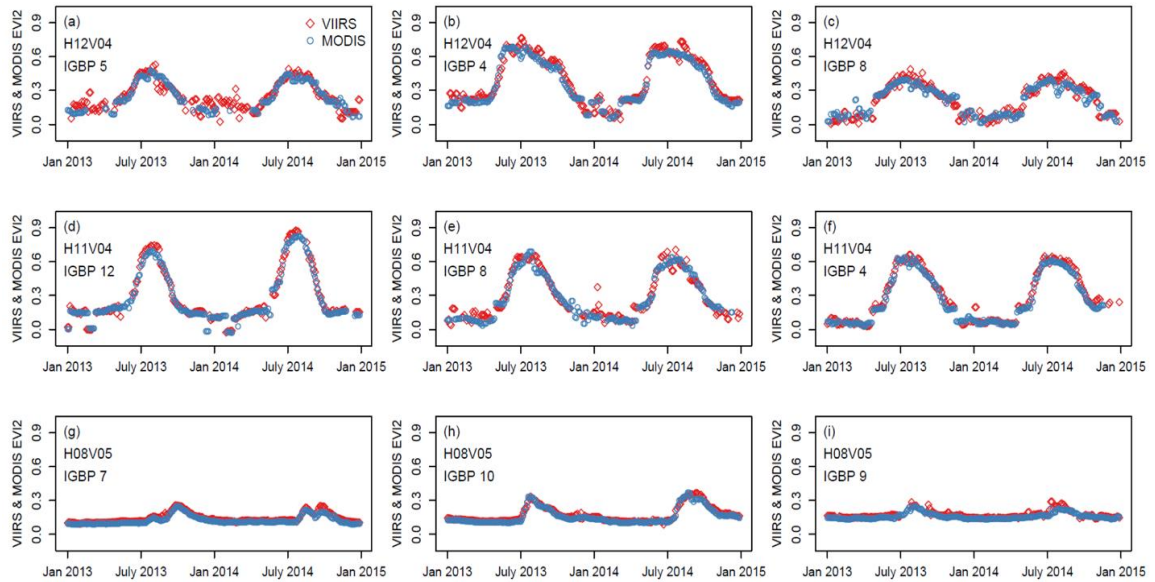


Fig. 2.6. NBAR EVI2 time series from VIIRS (diamonds) and MODIS (circles), stratified by the three most common land cover types in each tile during 2013 and 2014. Each dot represents 3-day composites NBAR EVI2 value from each instrument. See caption of Table 2.1 for IGBP class names.

Table 2.3 Linear regression and AI statistics for EVI2 time series from VIIRS and MODIS, stratified by the three most common land cover types in each tile. See caption of Table 2.1 for IGBP class names. RMSD is the root mean squared deviation; 25%, 50%, 75% represent the 1st quartile, median, and 3rd quartile, respectively.

Tile ID	IGBP	Linear Regression				Agreement Index				
		Slope	Intercept	R ²	RMSD	Product	Mean	25%	50%	75%
Forests	5	0.986	0.007	0.809	0.058	VIIRS	95.6	94.6	96.9	98.1
						MODIS	98.7	98.5	99.0	99.3
	4	1.016	0.012	0.880	0.062	VIIRS	97.9	97.5	98.4	98.9
						MODIS	99.0	98.8	99.1	99.4
	8	1.051	-0.004	0.889	0.057	VIIRS	96.7	96.0	97.6	98.4
						MODIS	98.8	98.7	99.2	99.4
Croplands	12	1.015	0.002	0.960	0.043	VIIRS	98.3	98.0	98.6	99.1
						MODIS	99.4	99.3	99.5	99.7
	8	1.024	-0.002	0.933	0.046	VIIRS	97.9	98.0	98.9	99.3
						MODIS	99.3	99.3	99.5	99.6
	4	1.014	0.002	0.942	0.044	VIIRS	98.8	98.8	99.2	99.4
						MODIS	99.5	99.4	99.5	99.6
Shrublands /Grasslands	7	1.018	0.011	0.913	0.020	VIIRS	86.9	84.4	93.0	96.9
						MODIS	95.2	94.4	97.3	98.5
	10	1.018	0.009	0.934	0.023	VIIRS	91.5	90.5	96.6	98.5
						MODIS	96.6	96.5	98.5	99.4
	9	1.016	0.008	0.899	0.024	VIIRS	89.8	87.1	94.4	97.7
						MODIS	96.5	95.7	98.2	99.3

To more fully explore the sources of disagreement between phenometrics from the VIIRS LSP and MODIS LCD products, Fig. 2.7 shows four scatterplots that attribute observed bias and RMSDs between phenometrics from each product (Table 2.2) to two key sources: (1) those arising from differences in the input data (i.e., MODIS versus VIIRS); and (2) those arising from differences in the algorithm used to estimate phenometrics (i.e., the MODIS LCD algorithm versus the VIIRS LSP algorithm). To generate these results, I compute phenometrics using the VIIRS LSP algorithm applied to EVI2 time series from both MODIS and VIIRS, and I compute phenometrics from both

algorithms using MODIS EVI2 time series (i.e., thereby isolating the magnitude of bias and variance introduced by the algorithm). I use the VIIRS LSP algorithm in the former case because the VIIRS LSP product is designed to replace the MODIS LCD product, and I use MODIS data in the latter case because MODIS EVI2 data are less noisy than VIIRS EVI2 data. In Figure 2.7, the vertical axes correspond to the biases (Fig. 2.7a and 2.7c) and RMSDs (Fig. 2.7b and 2.7d) between the MODIS LCD and VIIRS LSP products from Table 2.2. In Fig. 2.7a and 2.7b, the horizontal axes correspond to biases and RMSDs computed using phenometrics estimated using the VIIRS LSP algorithm applied to both VIIRS and MODIS EVI2 data (isolating the effect of input data). In Fig. 2.7c and 2.7d, on the other hand, the horizontal axes correspond to differences computed using phenometrics derived from the VIIRS LSP and MODIS LCD algorithms applied to MODIS EVI2 data (isolating the effect of the algorithms).

The results shown in Fig. 2.7a demonstrate that bias in phenometrics between the two products (i.e., bias in the product-to-product comparison) are uncorrelated with bias induced from input data, and that the magnitude of bias derived from input data is much smaller than the magnitude of bias between the two products. Fig. 2.7c, however, shows that biases induced by algorithm differences have the same magnitude and are correlated with the biases found in the product-to-product comparison. These results imply that the majority of systematic bias between the two products can be attributed to differences in the algorithms, not the input data (see also, Figs. A1 and A2 in the Appendix). Fig. 2.7b and 2.7d, on the other hand, show that RMSDs are correlated and have similar magnitude, and

so differences in input data and algorithms contribute equally to non-systematic differences (i.e., random errors) between the products.

To further quantify how noise in input data affects errors in estimated phenometrics, Fig. 2.8 shows results from the statistical simulation described in Section 2.3, where the vertical axes in Fig. 2.8a and 2.8b correspond to the RMSD values from the two products in Table 2.2, and the horizontal axes correspond to the RMSDs in phenometric retrievals induced by the inherent uncertainties in both VIIRS and MODIS NBAR data across land cover types within each tile. These results show that despite high agreement between NBAR EVI2 time series from MODIS and VIIRS, and excellent model fits to time series, errors arising from noise in EVI2 time series can introduce considerable uncertainty into the phenometrics. More specifically, when noise levels in input data are low, differences in phenometrics are mostly due to algorithmic uncertainty; as noise levels increase, errors in phenometrics are mostly caused by noise in the input data. Overall, errors from phenometrics estimated using MODIS NBAR data are marginally (but consistently) lower than those from VIIRS NBAR data (7.3 versus 8.7 days on overall means, respectively), and these errors are strongly correlated ($R^2 = 0.98$, $p < 0.001$; Fig. 2.8c).

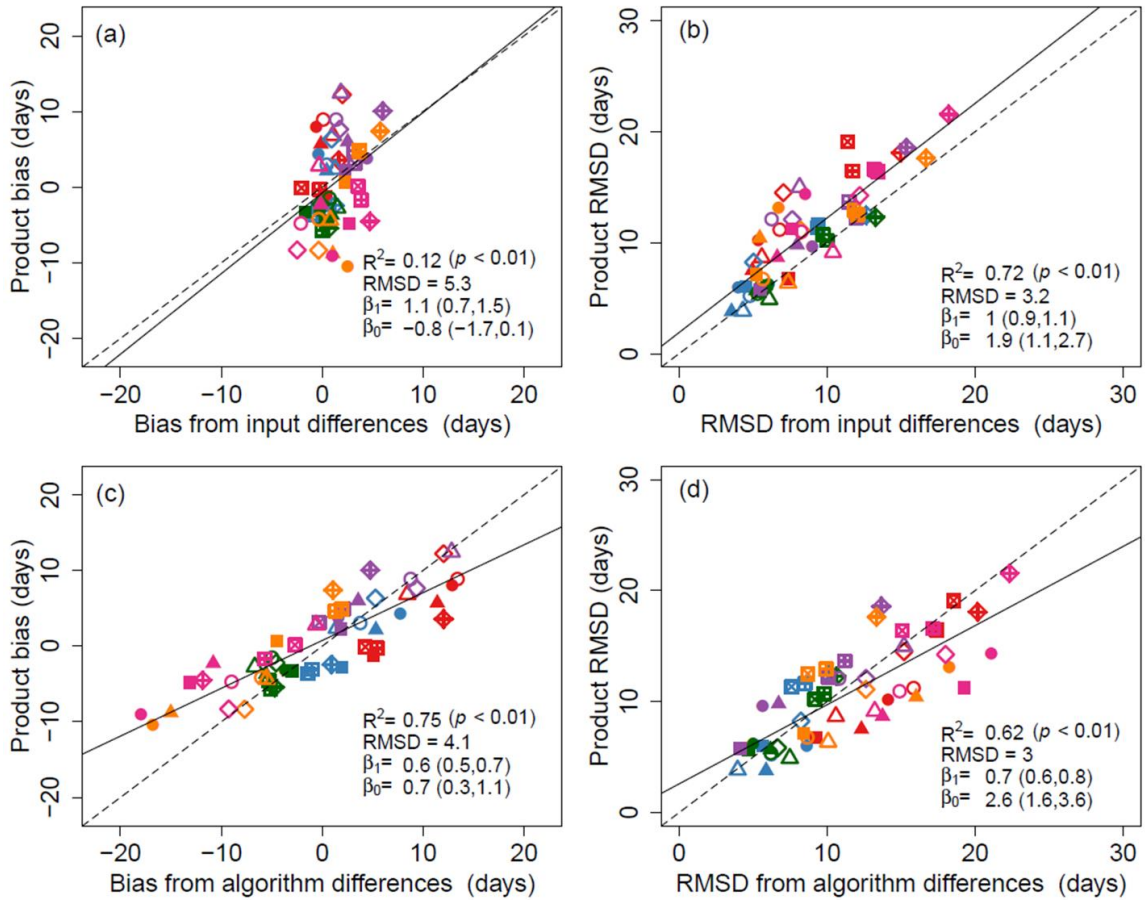


Fig. 2.7. Differences in phenometrics from MODIS LCD versus VIIRS LSP derived from differences in input (EVI2 time series) versus algorithms. Panels (a) and (b) illustrate differences in phenometrics arising from different input data, while panels (c) and (d) illustrate differences in phenometrics arising from the different algorithms. Bias represents differences in phenometrics; RMSD is the root mean squared deviation. Values in parentheses indicate ± 1 standard deviation. The solid and dashed lines are the regression and 1:1 lines, respectively. Different shapes denote different land cover types in different tiles and different colors denote different phenometrics. See Fig. 2.5 for symbols and color legends.

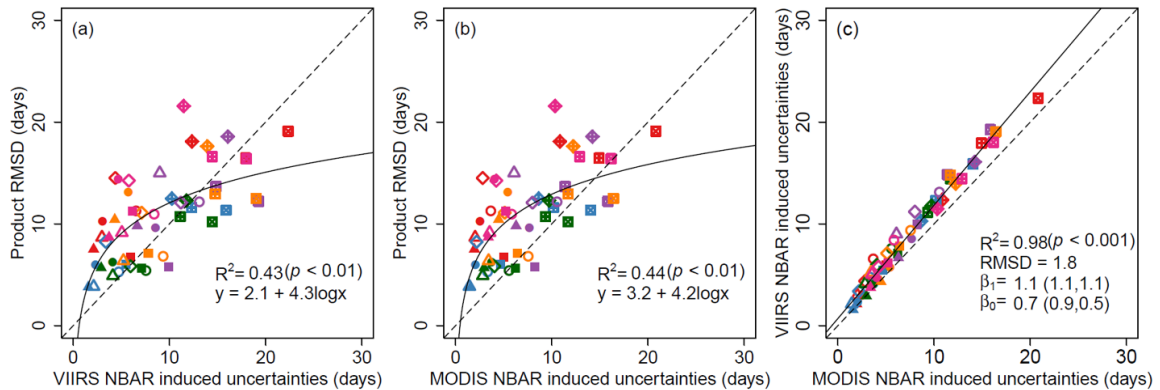


Fig. 2.8. Analysis of errors in phenometrics between the VIIRS LSP and MODIS LCD products versus errors introduced by uncertainties in input data. Panels (a) and (b) illustrate errors in phenometrics between the two products versus errors arising from uncertainties in VIIRS and MODIS input data, respectively; panel (c) illustrates relationship between errors arising from uncertainties in VIIRS and MODIS input data. Values in parentheses in panel (c) indicate ± 1 standard deviation. The solid and dashed lines are the regression and 1:1 lines, respectively. Different shapes denote different land cover types in different tiles and different colors denote different phenometrics. See Fig. 2.5 for symbols and colors legends.

2.3.3. Comparison with Landsat phenology

Fig. 2.9 presents a comparison between phenometrics derived from Landsat with corresponding dates derived from the VIIRS LSP and MODIS LCD products. It shows that results from all three instruments are in close agreement across all 22 sidelaps examined in this study. For SOS, both products show strong agreement with results from Landsat ($R^2 = 0.94$ and 0.95 for VIIRS and MODIS, respectively), with VIIRS results tending to be biased

later relative to Landsat for earlier greenup dates, and biased earlier for later dates (95% confidence interval for the slope of the regression = 1.2 ± 0.10). RMSD values are less than five days for both VIIRS and MODIS SOS dates relative to Landsat. For EOS, both products again show good agreement, but not quite as strong as those observed for SOS. EOS from MODIS exhibit better agreement with Landsat than EOS from VIIRS ($R^2 = 0.57$ and 0.82 for VIIRS and MODIS, respectively). Further, EOS dates from VIIRS are biased early relative to those from Landsat. Nevertheless, overall RMSD values were less than one week for both products. At regional scale (i.e., aggregated to EPA level II ecoregions), both products showed good agreement with Landsat. For SOS, RMSDs across six different ecoregions ranged from 2.8 to 13.2 with a mean of 7.1 for VIIRS, and from 3.0 to 16.4 with a mean of 6.8 for MODIS (Table 2.4). For EOS, RMSDs ranged from 4.2 to 14.9 with a mean of 8.5 for VIIRS and from 3.3 to 10.9 with a mean of 6.4 for MODIS (Table 2.5).

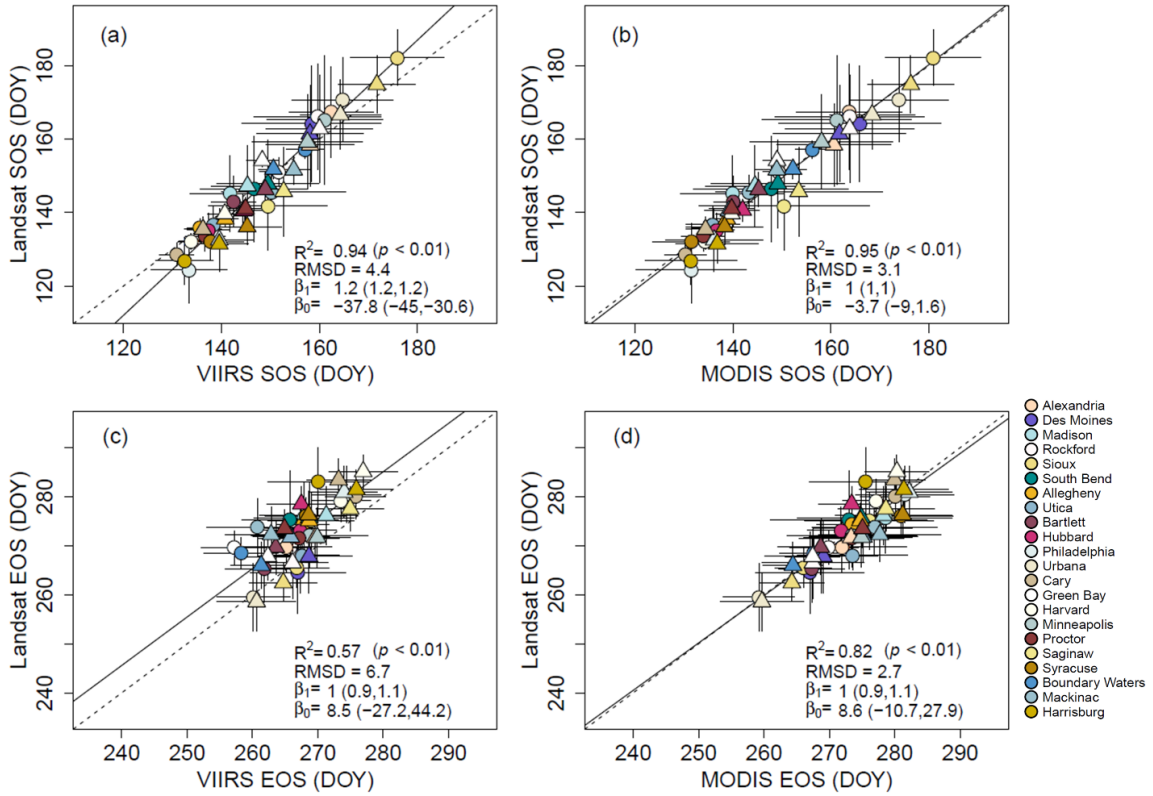


Fig. 2.9. Comparison of the VIIRS LSP and MODIS LCD products with phenometrics derived from Landsat in 2013 and 2014. Different colors denote different Landsat sidelaps and different shapes denote different years (circles: 2013; triangles: 2014). Values in parentheses indicate ± 1 standard deviation. The solid and dashed lines are the regression and 1:1 lines, respectively. See Table 2.4 and 2.5 for statistical summaries for each product in each sidelap.

Table 2.4 Statistical agreement of the VIIRS LSP and MODIS LCD products with SOS transition dates derived from Landsat in 2013. Bias is calculated as VIIRS – Landsat and MODIS – Landsat; RMSD is the root mean squared deviation; \bar{x} is the mean and σ is one standard deviation. Ecoregions are the EPA Level 2 ecoregions: AH: Atlantic Highlands; CUP: Central USA Plains; MWP: Mixed Woods Plains; MWS: Mixed Woods Shield; OA: Ozark/Ouachita-Appalachian Forests; TP: Temperate Prairies.

Spring												
Site name	Ecoregion	Latitude/ Longitude	Landsat		VIIRS				MODIS			
			\bar{x}	σ	\bar{x}	σ	Bias	RMSD	\bar{x}	σ	Bias	RMSD
Bartlett	AH	44.62/ -71.19	143	6.9	142	4.6	-0.5	5.8	140	4.0	-2.9	7.0
Hubbard	AH	43.90/ -71.40	135	4.6	137	4.4	2.1	4.6	137	3.6	1.4	4.0
Philadelphia	AH	40.52/ -75.63	124	9.1	133	7.8	9.0	11.5	131	11.3	7.1	11.5
Utica	AH	43.19/ -74.73	137	5.1	138	3.8	1.6	4.2	136	5.5	-0.9	4.4
Rockford	CUP	41.76/ -89.11	166	14.4	160	13	-6.5	8.9	164	15.2	-2.3	6.4
Urbana	CUP	40.51/ -87.99	171	11.5	165	10.3	-5.9	9.5	174	10.1	3.2	7.3
Alexandria	MWP	46.03/ -95.34	167	12.4	162	8.6	-5.0	9.6	164	10.8	-3.7	8.4
Allegheny	MWP	41.76/ -78.29	136	2.5	136	2.6	-0.3	2.9	135	3.5	-0.8	3.0
Cary	MWP	41.77/ -73.66	129	3.1	131	3.6	2.3	3.5	130	4.3	1.8	3.6
Green Bay	MWP	46.04/ -89.16	151	4.0	152	3.9	0.6	4.1	149	3.1	-1.8	4.2
Harvard	MWP	42.47/ -71.89	132	2.2	134	2.5	1.6	2.8	134	2.6	2.1	3.1
Madison	MWP	43.19/ -90.18	145	10.3	142	8.1	-3.4	7.4	140	10.6	-5.2	8.2
Minneapolis	MWP	44.61/ -92.77	165	17.5	161	11.8	-4.1	10.9	161	15.3	-4.0	9.9
Proctor	MWP	44.62/ -72.68	134	4.1	137	4.1	3.1	4.6	134	4.5	0.4	4.2
Saginaw	MWP	43.19/ -84.00	142	11.9	150	12.1	7.8	13.2	150	17.4	8.7	16.4
South Bend	MWP	41.76/ -86.02	146	14.3	147	11	0.3	8.3	148	15.8	1.4	8.2
Syracuse	MWP	43.19/ -76.27	132	5.0	138	6.7	5.8	9.0	132	7.9	-0.5	7.2
Boundary Waters	MWS	47.46/ -91.71	157	2.5	157	3.7	-0.1	3.4	156	3.5	-0.9	3.6
Mackinac	MWS	46.04/ -84.53	146	4.5	150	5.5	4.7	5.9	143	5.8	-2.3	4.4
Harrisburg	OA	40.52/ -77.17	127	6.4	132	5.9	5.6	8.9	131	9.3	4.5	10.3
Des Moines	TP	41.76/ -92.20	164	15.8	158	14.2	-5.8	9.4	166	16.6	1.7	8.0
Sioux	TP	43.19/ -94.78	182	7.5	176	9.6	-6.2	8.3	181	9.7	-1.3	5.2
Average	-	-	147	8.0	147	7.2	0.3	7.1	147	8.7	0.3	6.8

Table 2.5 Statistical agreement between the VIIRS LSP and MODIS LCD products with EOS transition dates derived from Landsat in 2013. Bias is calculated as VIIRS – Landsat and MODIS – Landsat; RMSD is the root mean squared deviation; \bar{x} is the mean and σ is one standard deviation. See Table 2.4 for the ecoregions.

Autumn											
Site name	Ecoregion	Landsat		VIIRS				MODIS			
		\bar{x}	σ	\bar{x}	σ	Bias	RMSD	\bar{x}	σ	Bias	RMSD
Bartlett	AH	265	6.8	262	6.1	-3.4	6.1	267	5.0	2.0	5.7
Hubbard	AH	273	4.7	267	5.6	-5.8	7.4	272	5.1	-1.3	3.3
Philadelphia	AH	280	5.8	274	5.3	-6.1	8.5	282	7.5	1.1	7.1
Utica	AH	268	3.0	268	5.6	-0.4	4.8	274	8.4	5.5	9.5
Rockford	CUP	268	7.6	267	6.5	-0.5	5.0	269	8.7	0.8	4.5
Urbana	CUP	259	6.8	260	5.6	0.6	4.4	259	5.5	-0.3	4.1
Alexandria	MWP	270	5.1	265	6.9	-4.6	8.2	272	9.9	2.2	8.1
Allegheny	MWP	274	3.0	268	4.0	-6.6	7.6	273	5.3	-0.9	5.2
Cary	MWP	280	4.7	276	4.6	-4.3	6.1	280	5.3	0.0	5.3
Green Bay	MWP	270	3.5	257	5.0	-12.4	13.6	270	4.5	0.2	4.3
Harvard	MWP	279	4.3	273	4.5	-5.7	6.7	277	5.1	-2.0	3.5
Madison	MWP	276	7.2	268	7.6	-7.8	11.2	279	10.1	2.9	9.0
Minneapolis	MWP	272	6.4	269	8.9	-3.4	9.3	273	9.9	1.3	7.9
Proctor	MWP	271	3.6	267	6.2	-4.4	6.7	273	8.0	2.0	7.3
Saginaw	MWP	275	5.9	269	6.6	-6.2	9.2	276	9.9	1.0	8.2
South Bend	MWP	275	10.0	266	7.4	-9.6	12.4	273	12.0	-2.3	7.4
Syracuse	MWP	276	3.8	268	6.3	-7.9	9.6	281	7.9	4.9	8.2
Boundary Waters	MWS	268	3.1	258	5.7	-10.2	11.6	268	5.2	-0.9	4.7
Mackinac	MWS	274	5.9	261	7.7	-13.0	14.9	277	9.5	3.2	8.0
Harrisburg	OA	283	7.0	270	7.7	-13.0	14.6	276	8.5	-7.6	10.9
Des Moines	TP	264	8.3	267	7.3	2.5	5.4	267	8.3	2.5	4.9
Sioux	TP	266	4.1	267	4.9	1.2	4.2	266	4.4	0.5	3.6
Average	-	272	5.5	267	6.2	-5.5	8.5	273	7.5	0.7	6.4

2.3.4. Comparison with PhenoCam phenology

Phenometrics derived from VIIRS and MODIS show generally strong agreement with phenometrics estimated from PhenoCam imagery, but with more scatter relative to dates estimated from Landsat (Fig. 2.10). Disagreement is highest for evergreen needleleaf sites, where phenological amplitude is low and difficult to detect using vegetation indices such as the G_{CC} and EVI2. Thus, I do not expect strong correspondence between ground-based and satellite-derived retrievals in these systems. Other land cover types (e.g., deciduous broadleaf forests and croplands), on the other hand, show agreement that is comparable to those obtained with Landsat-derived SOS and EOS dates (Table 2.6).

It is important to understand that PhenoCam and coarse spatial resolution sensors, such as VIIRS and MODIS, observe the surface with very different fields of view. Hence, comparison of VIIRS LSP and MODIS LCD products with PhenoCam results depends heavily on the representativeness of the region of interest in PhenoCam imagery used to generate G_{CC} time series relative to the field of view captured by 500 m MODIS and VIIRS pixels. Fig. 2.11 illustrates this issue at the Jasper Ridge PhenoCam site, which provides a good illustration of this challenge. Specifically, Fig. 2.11a shows the 500 m MODIS and VIIRS pixel overlain on 30 m Landsat imagery centered over the Jasper Ridge PhenoCam site, and Fig. 2.11b shows the region of interest used to generate G_{CC} time series from PhenoCam imagery. As these two panels show, a large portion of the land cover located within the 500 m pixel consists of tree cover. The PhenoCam region of interest (Fig. 2.11b), however, includes only herbaceous vegetation. As a result, the PhenoCam G_{CC} time series (Fig. 2.11c) captures the phenology of grasses at the site, which is different from the

phenology measured in EVI2 time series from VIIRS and MODIS that includes substantial contributions from over-story tree phenology. This target mismatch leads to clear differences in observed phenology, especially during the green-down phase.

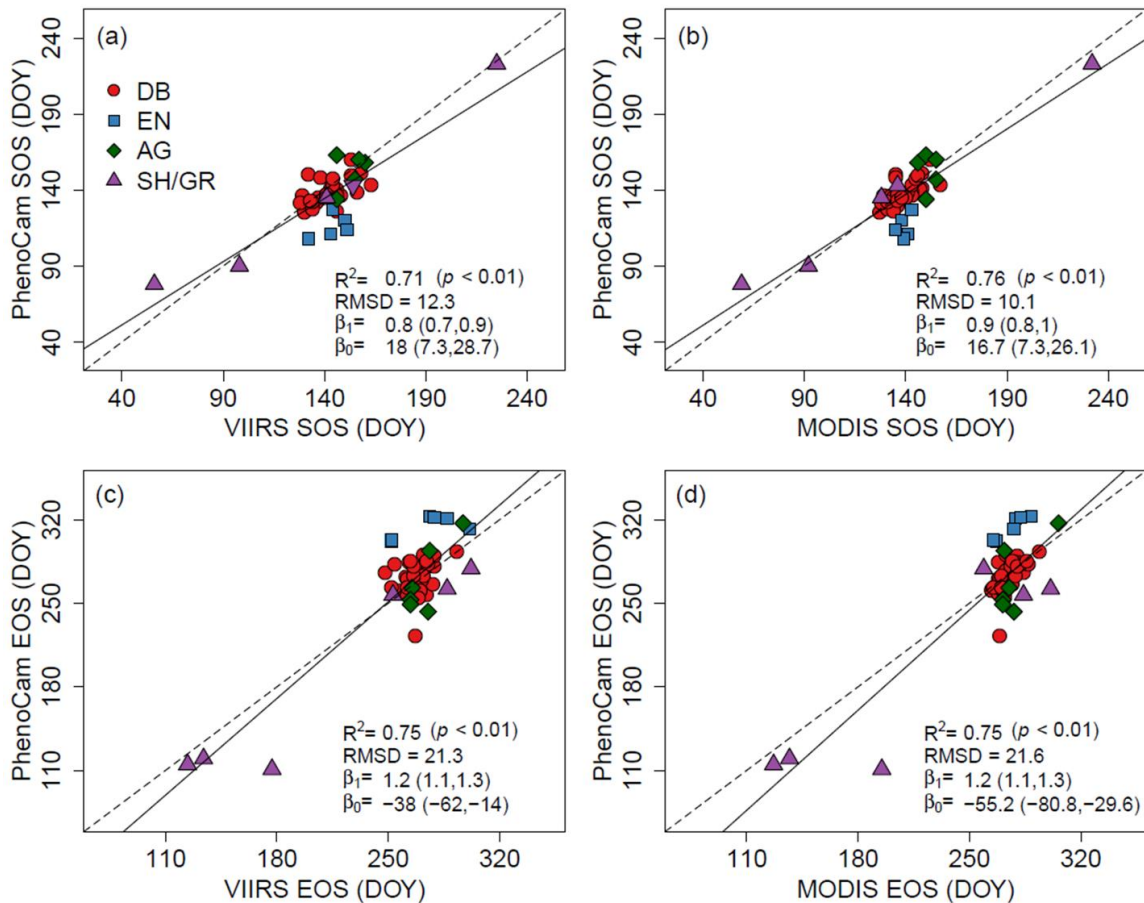


Fig. 2.10. Comparison of the VIIRS LSP and MODIS LCD products with phenometrics derived from PhenoCam imagery in 2013 and 2014. SOS and EOS represent the DOY at mid-greenup and mid-down for the VIIRS and MODIS products, respectively. Different colors denote different vegetation types (see panel a) at each PhenoCam site (DB: deciduous broadleaf; EN: evergreen needleleaf; AG: agricultural; GR: grassland; SH:

shrubland). Values in parentheses indicate ± 1 standard deviation. The solid and dashed lines are the regression and 1:1 lines, respectively. See Table 2.6 for the statistical agreement between PhenoCam and both VIIRS and MODIS SOS and EOS dates, for each vegetation type.

Table 2.6 Statistical agreement between the VIIRS LSP and MODIS LCD products with phenometrics derived from PhenoCam imagery. n is the number of site-years; Bias is calculated as VIIRS – PhenoCam and MODIS – PhenoCam; RMSD is the root mean squared deviation. See Fig. 2.10 for the vegetation type.

Spring											
Vegetation type	n	PhenoCam		VIIRS				MODIS			
		\bar{x}	σ	\bar{x}	σ	Bias	RMSD	\bar{x}	σ	Bias	RMSD
DB	38	137	7.7	141	8.3	4.2	8.3	138	7.1	1.4	5.8
EN	5	116	7.6	144	7.6	28.0	28.8	139	3.0	23.2	24.0
AG	5	152	11.9	153	6.5	0.4	10.1	151	3.8	-1.2	11.5
GR/SH	5	134	57.2	135	63.5	1.0	11.9	129	65.1	-4.4	10.4
Autumn											
Vegetation type	n	PhenoCam		VIIRS				MODIS			
		\bar{x}	σ	\bar{x}	σ	Bias	RMSD	\bar{x}	σ	Bias	RMSD
DB	38	271	13.7	268	8.3	-2.9	13.7	274	6.7	3.1	11.2
EN	6	314	9.6	275	19.5	39.3	41.7	277	9.1	37.2	37.3
AG	6	270	29.3	274	12.8	3.7	18.7	279	13.6	9.0	21.5
GR/SH	6	191	82.9	213	78.0	22.2	31.1	217	75.2	26.5	41.1

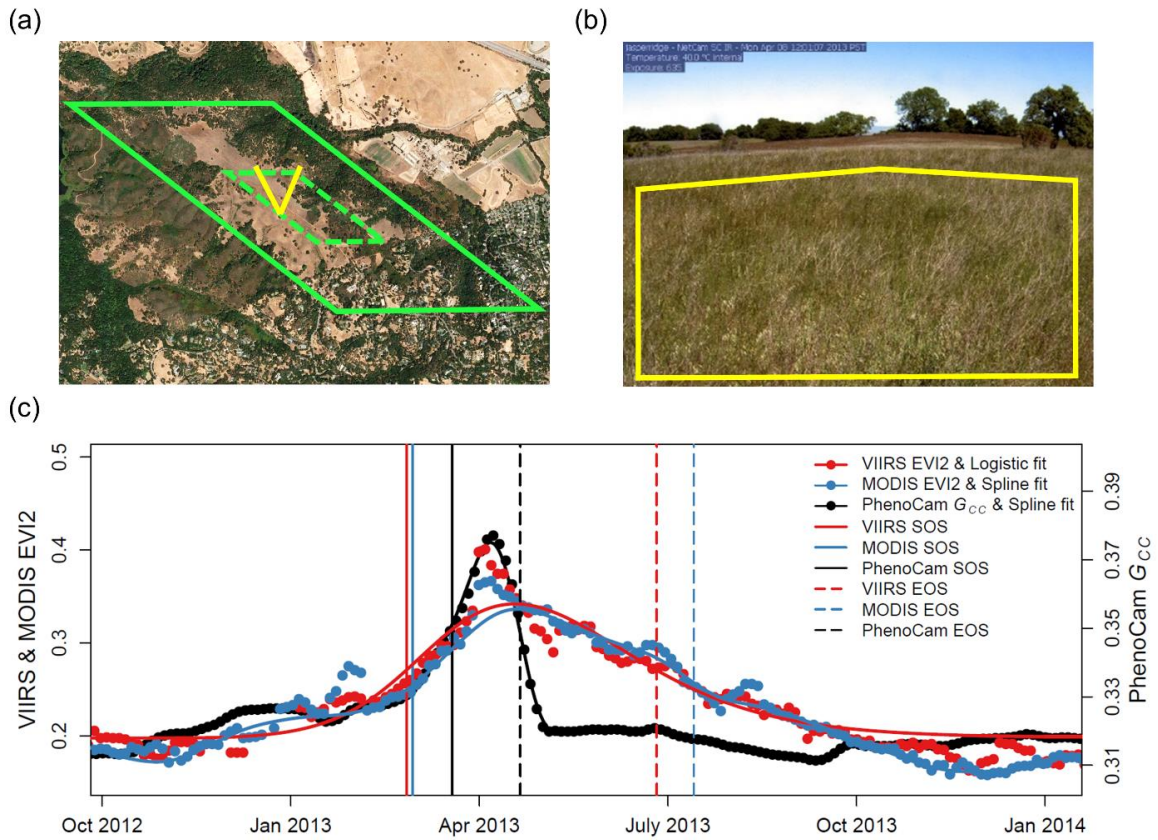


Fig. 2.11. VIIRS and MODIS pixels over the Jasper Ridge PhenoCam site (a), a PhenoCam image and region of interest used to generate G_{CC} time series (b), and time series of EVI2 from VIIRS, and MODIS, along with G_{CC} from PhenoCam (c). Phenometrics from each time series are shown as vertical lines. In panel (a), the solid and dashed green lines represent a 3 by 3 window and the 500 m pixel centered at the camera's location, respectively; the yellow lines indicate the field of view of the PhenoCam. In panel (b), the yellow box represents the extracted region of interest from PhenoCam imagery.

2.4. Discussion

The land product suite from MODIS provides an 18-year (and growing) record of global land properties and processes during an era when global environmental change has been accelerating. Originally designed as a research mission, MODIS has evolved to provide a critical source of time series observations supporting operational environmental monitoring and global change science. With the MODIS era approaching its end, the VIIRS instrument has been designated to provide continuity with measurements and products from MODIS. In this paper, I evaluated the suitability of the VIIRS Land Surface Phenology product for providing long-term continuity with the MODIS Land Cover Dynamics product, focusing on two main elements. First, I performed an extensive comparison of the MODIS LCD and VIIRS LSP products, focusing on the nature, magnitude, and sources of differences between the products. Second, I compared both products against two independent sources of land surface phenology data.

2.4.1 Comparison of MODIS LCD and VIIRS LSP products

The results from this study indicate that the MODIS LCD and VIIRS LSP products are qualitatively and quantitatively similar, but also identify subtle differences arising from three key sources:

(i) *Instrument differences.* Although VIIRS was originally conceived to provide observation continuity with MODIS (Justice et al., 2013), the properties of these two sensors are different, which results in modest discrepancies between operational products from each instrument. Most importantly in the context of this work, both the VIIRS LSP

and MODIS LCD products use NBAR surface reflectance as their primary input. My analysis identified modest differences in NBAR EVI2 time series from VIIRS versus MODIS that propagate into the VIIRS LSP and MODIS LCD products (Fig. 2.7 and 2.8). Consistent with Liu et al. (2017), who reported that the VIIRS NBAR product is comparable with the MODIS NBAR product, my results suggest that NBAR EVI2 time series from each sensor are in good agreement and do not show systematic differences or biases (Fig. 2.6 and Table 2.3). However, similar to Zhang et al. (2017a), AI values computed from VIIRS and MODIS NBAR EVI2 time series indicate that EVI2 time series from MODIS are more stable than those from VIIRS. In addition, errors in phenometrics induced by uncertainty in VIIRS NBAR data are larger than those induced by uncertainty in MODIS NBAR data (Fig. 2.8). While I am not able to conclusively attribute this difference to a specific source, the most likely explanation for observed differences in EVI2 time series is lower data density available from VIIRS relative to MODIS. Specifically, NBAR data from VIIRS are based on a single (1:30 pm equatorial) overpass, whereas MODIS NBAR data are computed using observations from both the morning (10:30 am equatorial) MODIS-Terra and afternoon (1:30 pm equatorial) MODIS-Aqua overpasses (Zhang et al., 2017a).

(ii) *Differences in NBAR EVI2 pre-processing.* Both algorithms depend on successful retrieval of a “background” or seasonal minimum EVI2 value at each pixel. The VIIRS LSP algorithm uses land surface temperature in addition to snow flags from the VIIRS NBAR product to identify and remove snow-contaminated pixels, while the MODIS LCD algorithm only uses snow flags from the MODIS NBAR product in combination with NDSI

values. These approaches reflect modestly different assumptions regarding the quality of NBAR snow flags, and have the potential to induce subtle differences between the two products. In particular, the MODIS LCD product tends to have slightly longer growing season lengths than corresponding values from the VIIRS LSP product in temperate regions (e.g., forests and croplands tiles, Table 2.2 and Fig. 2.4). This effect appears to be limited to temperate regions, and I did not find other examples or evidence of significant and systematic differences between phenometrics from each product. In addition, disagreement between VIIRS LSP and MODIS LCD phenometrics is more prevalent in semi-arid land cover types (i.e., higher RMSDs for shrublands and grasslands in Table 2.2). This issue is not unexpected because low seasonal amplitude in the EVI2 time series (as shown in Fig. 2.6) tends to increase uncertainty in estimated LSP metrics (Fig. 2.8), and because subtle differences in smoothing and gap filling will lead to differences in estimated phenometrics (Fig. 2.7).

(iii) Differences in the method used for EVI2 time series modeling. Currently, there is no consensus in the land surface phenology community regarding optimal methods and algorithms for deriving land surface phenology metrics. The algorithm used to generate the VIIRS LSP product uses a logistic model to provide a simple, bounded, and continuous function for modeling EVI2 variation associated with leaf emergence, maturation, and senescence (Zhang, 2015). This approach is widely used for modeling phenological dynamics in biological systems, and provides a framework that is widely accepted and interpretable. The Collection 6 MODIS LCD product, on the other hand, uses penalized cubic splines to model temporal variation in NBAR EVI2 time series (Gray et al., 2020).

Unlike logistic models, local fitting techniques such as splines are more flexible and are therefore able to capture a broader range of temporal dynamics (e.g., asymmetric phenology; Verma et al., 2016). At the same time, because penalized cubic splines provide local fits to data, they are more sensitive to gaps and high frequency variation in EVI2 time series. Hence, in situations where missing data are pervasive, penalized cubic splines are less robust than logistic models (Zhang et al., 2018b). Further, the different methods for selecting transition dates in each algorithm (i.e., the curvature change rate versus amplitude threshold) can introduce differences between the two products, and Klosterman et al. (2014) report that landscape heterogeneity can introduce uncertainty in curve fit estimates during green-down. Consistent with these results, my analyses show that differences between MODIS LCD and VIIRS LSP results in mixed forests were marginally larger than those found in deciduous broadleaf forests during the green-down phase, especially for senescence onset (IGBP 5 versus 4; Table 2.2), and I found larger differences in EOS than in SOS (e.g., Fig. 2.11).

2.4.2 Comparisons with independent data

In addition to comparing results from each algorithm and product, I also assessed agreement of each product with LSP measurements from Landsat and PhenoCam data. Results from Landsat have the advantage of being estimated from remote sensing using instrumentation with similar spectral properties to MODIS and VIIRS, but at finer spatial resolution. The PhenoCam Dataset V1.0 (Richardson et al., 2018a) based on digital repeat photography, on the other hand, provides a source of “near-surface” remote sensing that

covers a wide range of biomes. Results from these comparisons show that the VIIRS LSP and MODIS LCD products both agree well with phenometrics derived from Landsat (Fig. 2.9). Across six ecoregions spanning the Central and Northeastern U.S, the mean RMSD for SOS was roughly one week for both products (Table 2.4). RMSDs between Landsat EOS and corresponding metrics from MODIS and VIIRS are modestly higher, but are also on the order of one week (Table 2.5). Interestingly, even though agreement with Landsat SOS is lower at local scale for both the MODIS LCD and VIIRS LSP products, overall mean RMSD at the scale of ecosystems is comparable across instruments, which suggests that even though local uncertainty in SOS retrievals is significant, they do not appear to be biased. EOS values for the MODIS LCD product show modestly higher agreement with Landsat EOS dates relative to VIIRS LSP values. However, closer inspection indicates that overall bias for both products is similar and quite low, which implies that such differences may be explained by the fact that the LPA uses cubic splines to fit EVI time series from Landsat (i.e., similar to the MODIS LCD product), while the VIIRS LSP does not.

Evaluation of satellite-derived land surface phenology products with PhenoCam-derived phenometrics is challenging, and lower agreement between phenometrics from PhenoCam and both the MODIS LCD and VIIRS LSP products can be explained by two main factors. First, because PhenoCams do not generally provide imagery acquired in near infrared wavelengths (Yang et al., 2014), phenometrics from PhenoCam are estimated using a vegetation index based on visible bands (i.e., G_{CC} , Sonnentag et al., 2012). Richardson et al. (2018b) performed a comprehensive assessment of G_{CC} time series and phenometrics derived from PhenoCam against both MODIS NDVI and LCD data using

the PhenoCam Dataset V1.0, and showed good agreement in both cases. However, similar to my results, they identified differences in the sensor field of view, in combination with landscape heterogeneity, as key sources of disagreement. Consistent with Richardson et al. (2018b), my results show that, with the exception of evergreen needleleaf sites, phenometrics derived from PhenoCam G_{CC} time series agree reasonably well with the VIIRS LSP and MODIS LCD products, but that sub-pixel heterogeneity within satellite-based remote sensing pixels can cause substantial discrepancies in estimated phenometrics (Fig. 2.11).

2.5. Conclusion

In this paper, I evaluate and quantify similarities and differences between two operational LSP products. The specific motivation for this work is to address the question of whether the VIIRS LSP product provides continuity with the MODIS LCD product for long-term studies of land surface phenology. As part of my analysis, I compare EVI2 time series from each instrument, quantify random and systematic differences between phenometrics from each sensor, and conduct a multi-scale comparison of the VIIRS LSP and MODIS LCD products with phenometrics derived from Landsat and PhenoCam imagery. My results indicate that the VIIRS LSP product is very similar to the MODIS LCD product and can be used to extend the MODIS record, but some modest differences are found that users need to be aware of (and account for) if time series of VIIRS LSP and MODIS and LCD data are used together. In particular, I recommend that studies attempting to create long-term LSP time series by merging phenometrics from the MODIS LCD

product with corresponding phenometrics from the VIIRS LSP product should estimate land cover-specific adjustments (i.e., following the basic procedure I used in this paper) that correct for modest systematic biases in the MODIS LCD product relative to the VIIRS LSP product.

3. CLIMATE CONTROLS ON SPRINGTIME PHENOLOGY IN EASTERN TEMPERATE FORESTS OF NORTH AMERICA

3.1. Introduction

A large body of research has focused on improving understanding of the ecophysiological controls of plant phenology (Piao et al, 2019; Richardson et al., 2013). These efforts have been motivated by observational evidence suggesting that the length of growing seasons is changing (Cleland et al., 2007; Panuelas et al., 2009), and because phenology both controls and is diagnostic of important ecosystem functions and services. Hence, understanding how ecological and bioclimatic factors control phenology is critical to understanding how ecosystems will respond to future climate change.

Unfortunately, despite extensive efforts devoted to this topic over the last two decades, mechanistic understanding of how to accurately model plant phenology remains incomplete. Results from experimental studies using seedlings, cut twigs, or warming experiments have provided important insights, but are limited by the fact that phenological behavior under such conditions is known to differ from behavior observed in natural ecosystems (Clark et al., 2014a; Gaston and Blackburn, 2008; Tilman, 1989; Wolkovich et al., 2012) and because the phenology of saplings differs from that of mature trees (Augspurger and Bartlett, 2003; Richardson et al., 2009; Uemura, 1994). Further, the manner in which environmental conditions are imposed in most of these experiments (e.g., 2 °C warming) are not representative of changes that are expected in the future, which are predicted to occur gradually (Easterling et al., 2000; Walther et al., 2002). These issues are compounded by the fact that the geographic coverage of samples used in such studies is

generally quite limited and therefore does not reflect the complete bioclimatic range of species examined, which for some species can be quite large (e.g., Basler, 2016; Uemura, 1994; Zohner and Renner, 2017). As a consequence, geographic variation in the sensitivity of phenological cues on spring phenology, both within and across species, is poorly understood.

A different strategy for improving understanding of phenology is to use inverse modeling techniques based on mechanistic models linked to observational records of phenology collected on the ground (e.g., Basler, 2016; Kramer, 1994; Morin et al., 2009) or from remote sensing (e.g., Liu et al., 2017; Melaas et al., 2016, 2013; Yang et al., 2012). For example, Liu et al. (2017) tested several spring phenology models calibrated against satellite-derived observations of phenology that incorporate multiple phenological cues to model the timing of springtime phenology across the Northern Hemisphere circumpolar region. Based on results from their analysis, Liu et al. concluded that photoperiod plays an important role in controlling the onset of vegetation growth. Further, because a simple thermal forcing model performed as well or better than models that include chilling and photoperiodic cues, Liu et al. concluded that chilling requirements are fulfilled across most of the boreal zone. These results support the conclusions of Richardson et al. (2018), who used an experimental approach to show that the timing of leaf-out in tree species at higher latitudes is unaffected by photoperiod, which suggests a likely extension of the period of vegetation activity in the coming decades, and also suggests that the vulnerability to spring frost damage will increase in the coming decades.

Despite significant advances provided via both modeling and experimental approaches, important gaps of understanding remain regarding how the phenology of trees responds to variation in environmental conditions (Hänninen et al., 2019). Further, as Clark et al. (2014b) point out, quantities such as degree-days and winter chilling, which are widely used in phenological models, are impractical for forecasting expected changes in phenology arising from climate change because models that rely these terms generally use prescribed thresholds that are not identifiable, and more generally, most phenology models ignore the impact of observation errors in model estimation. To address this knowledge and methodological gap, the objective of this study is to use a state-space Bayesian modeling framework that includes explicit quantification of uncertainty in model parameters to: (1) quantify how thermal forcing, day-length, and winter chilling affect the timing of springtime phenology; and (2) characterize how these controls vary across large geographic areas. To accomplish these objectives, I develop and apply this modeling framework to Collection 6 MODIS land surface phenology data for a region encompassing the temperate deciduous forest biome of North America for the period 2001 to 2017.

3.2. Data and Methods

3.2.1. Study region and data

The study region includes the Northern Forests and Eastern Temperate forests ecoregions included in level 1 of the US EPA Ecoregions of North America, which encompasses the vast majority of temperate and boreal deciduous forests in North America (Fig. 3.1). To distinguish deciduous forests from evergreen forests and other types of land

cover within the study area, the 500 m Collection 6 MODIS Land Cover Type product was used, which provides annual land cover classifications based on machine learning that are post-processed using a multi-temporal state-space modeling framework to reduce spurious land cover change introduced by classification uncertainty in individual years (Abercrombie and Friedl, 2016; Sulla-Menashe et al., 2019). For this work, each 10° by 10° MODIS tile intersecting the Northern Forests and Eastern Temperate Forests ecoregions was subsetted into 2,018 25 km² cells (i.e., 5 km x 5 km cells, where each cell includes 100 MODIS pixels), which were used as the basic unit of analysis. Only pixels labeled as deciduous broadleaf or mixed forests were included, and to exclude effects unrelated to climate forcing (e.g., from land use and land cover change), only pixels with stable land cover from 2001 to 2017 were used. Finally, to ensure analyses were based on grid cells dominated by deciduous forest cover, only cells where the fraction of MODIS pixels labeled as deciduous broadleaf or mixed forests was greater than 50% were retained (Fig. 3.1).

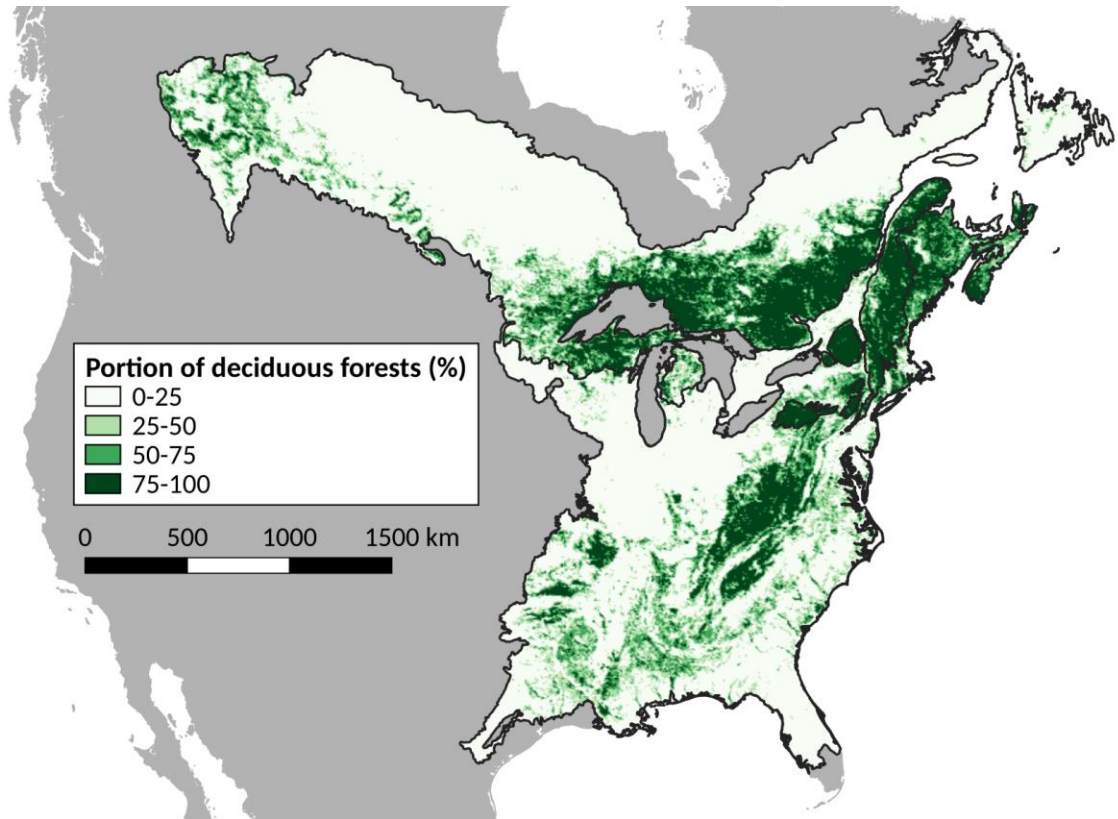


Fig. 3.1. Map of the study area showing the Northern Forest and Eastern Temperate Forest ecoregions defined by the United States Environmental Protection Agency, along with the proportion of deciduous forests in 25 km² grid cells according to the MODIS Land Cover Type product.

To identify the timing of springtime phenology from 2001 to 2017 over the study region, I used the Collection 6 MODIS Land Cover Dynamics product (Moon et al., 2019). This product uses time series of the two-band Enhanced Vegetation Index (EVI2) to identify the timing of six key phenophase transition dates during each growing season in each 500-m MODIS pixel. For this analysis, I use the day of year (DOY) corresponding to

the onset of greenness increase, which is defined in the MODIS Land Cover Dynamics product as the DOY during the greenup phase when the EVI2 time series at each pixel exceeds 15% of its seasonal amplitude.

To provide meteorological data required for model estimation, I used the Version 3 Daymet data set, which includes daily gridded surface meteorological data at 1 km spatial resolution for all of North America (Thornton et al., 2017; <https://daymet.ornl.gov>). The Daymet data set uses digital elevation data in association with a land-water mask and meteorological observations measured at ground-based stations to create gridded time series of surface meteorological data at 1 km spatial resolution spanning the period from 1980 to present. For this work, I used daily maximum and minimum 2-m air temperatures and day-length from 2000 to 2017, extracted for all 25 km² cell included in my analysis.

3.2.2. Springtime phenology model

To estimate the relative importance of different climatological controls on springtime phenology, I used a hierarchical Bayesian state-space model that predicts the timing of springtime phenology based on three key drivers: daylength, thermal forcing, and chilling units. The original form of this model was proposed by Clark et al. (2014b), who used this general approach to show that because more conventional process-based phenology models (e.g., spring warming, sequential, parallel models, etc.; see Liu et al., 2017) collapse temperature time series into cumulative sums or mean values for each year or season, they misrepresent how different forcing variables affect the timing of phenology.

Following the general approach developed by Clark et al. (2014b), the model I use here is designed to track the continuous response of phenological development to variations in environmental forcing at daily time step. To do this, the model uses a state space framework that includes an unobservable latent state in which phenological development responds continuously in response to environmental forcing before observable discrete changes occur (e.g., the onset of springtime phenology via budburst and leaf emergence). This latent state is expressed as follows:

$$h_{g,s,d+1} = h_{g,s,d} + \delta h_{g,s,d} \quad (3.1)$$

where $h_{g,s,d}$ is the latent state for grid cell g and sample s on day d , and $\delta h_{g,s,d}$ is the latent state increment from d to $d + 1$, which defined as

$$\delta h_{g,s,d} = \begin{cases} (X_{g,s,d} \times \beta)(1 - h_{g,s,d}/h_{max}), & \delta h_{g,s,d} \geq 0 \\ 0, & \delta h_{g,s,d} < 0 \end{cases} \quad (3.2)$$

where $X_{g,s,d}$ is the matrix of predictors and β is the vector of estimated model coefficients. Note that Eq. 3.2 implies that: (1) even though a linear formulation is used to describe the relationship between model predictors and coefficients, the model accommodates nonlinear responses in phenological developments to environmental forcing by adopting an asymptotic limit for the latent state (i.e., $h_{g,s,d}/h_{max}$); and (2) the latent state increment is always non-negative.

Using this framework, the continuous scale of the latent state (h), which captures phenological development, is used to identify discrete phenological stages such as the timing of spring greenup onset. To do this, a logit transformation is used:

$$\text{logit}(P_{g,s,d}) = \kappa + \lambda \times h_{g,s,d} \quad (3.3)$$

where $P_{g,s,d}$ is the probability that the onset occurs at sample pixel s in grid g on day d , and κ and λ are the intercept and slope of the transformation, respectively. Because, greenup onset is defined as a discrete event, $P_{g,s,d}$ follows a Bernoulli distribution:

$$Y_{g,s,d} \sim \text{Bernoulli}(P_{g,s,d}) \quad (3.4)$$

where $Y_{g,s,d}$ indicates whether or not greenup onset has occurred for sample s in grid g on day d .

Daily mean temperature, day-length, and chilling units are used as the predictors in this model. For daily average temperature, I computed the average of daily maximum and minimum temperatures from Daymet in each cell, and chilling units ($\text{CU}_{g,s}$) were defined as:

$$\text{CU}_{g,s} = \sum_{d=c_0}^{c_{g,s}} (T_{g,s,d} < T'_c) \quad (3.5)$$

In other words, $\text{CU}_{g,s}$ is defined as the number of days below a prescribed threshold T'_c (= 0 °C) during the period after the onset of dormancy until an unobserved date $c_{g,s}$ when the chilling requirement is assumed to be satisfied. Note that because the main objective of this study is to quantify the relative importance (and geographic variation thereof) among key controls on the timing of springtime phenology, each of the variables is normalized for each of grid g and sample s to have a mean value of 0 with a standard deviation of 1. As a result, only the relative magnitude of day-to-day variations affect model inferences, and

the model provides scaled coefficients that are easily compared to assess the relative importance of each forcing variable.

3.2.3. Model application

To facilitate computational efficiency, I used randomly sampled grid cells from each of the MODIS tiles included in the study region. The number of valid grid cells from each MODIS tile ranged from 30 to 19,888. If less than 300 valid grid cells (i.e., with >50% stable deciduous land cover) were available within a tile, all of the cells are used. If more than 300 were available, I used a random sample of 300 grid cells. This yielded a total of 2,018 grid cells to which the model was applied (Fig. 3.1).

At each grid cell, 100 site-years of data were used to infer model posteriors. To minimize spatial and temporal autocorrelation in the data set used to estimate the model, each sample was randomly selected within each grid cell across the 17-year study period from a total pool of more than 850 sample points (e.g., at least 50 pixels per year in each grid across 17 years). December 1st of the previous year and DOY 250 (~Sept. 7) of the current year were used as the start and end dates of latent state development, respectively. These dates were selected to provide sufficient time for latent stage development. Posterior sampling was performed using the “R2jags” package in R (Su and Yajima, 2015), with 10,000 iterations and 3,000 burn-in periods.

Model results from a representative grid cell are shown in Fig. 3.2. Overall, predicted onset dates are well aligned with observed onset dates, with a root-mean-square error of 3.68 (Fig. 3.2a). The posterior distributions for each model coefficient, which reflect the sensitivity of phenological development to each input variable, show clear

differences that are independent of the unnormalized magnitude or units of each input variable (Fig. 3.2b). In addition, the time series of the latent state generated by the model provide useful information regarding the timing and duration of “preseason-period” prior to greenup onset. Previously, this period has been defined as “as the most temperature-sensitive period preceding the phenological event” (Güsewell et al., 2017) or “the period before leaf unfolding for which the partial correlation coefficient between leaf unfolding and air temperature is highest” from a statistical perspective (Fu et al., 2015). If I assume that this period corresponds to the time interval when phenological development is affected by phenological cues (e.g., air temperature), I can use the model used here to identify the “preseason-period” as starting on the DOY when the latent state starts to increase and ending on the DOY when greenup onset occurs (i.e., the period indicated by the arrow in Fig. 3.2c).

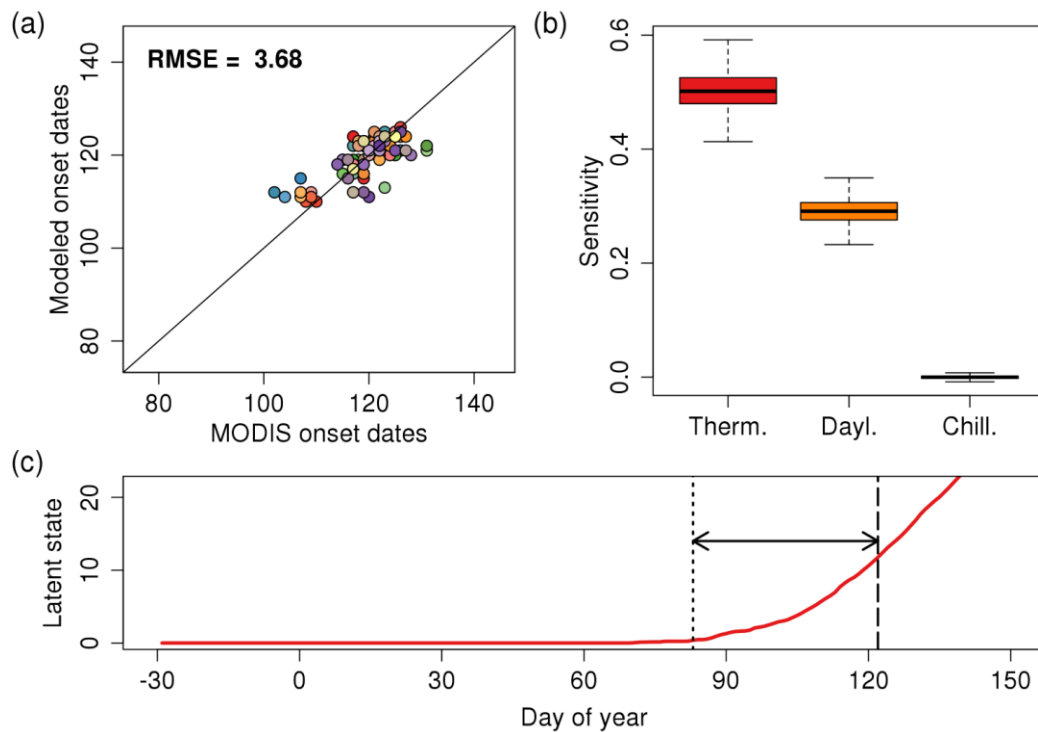


Fig. 3.2. Model estimates from a randomly selected representative grid cell. Panel (a) shows the relationship between the MODIS onset dates and onset dates estimated by the model; panel (b) shows the distribution of posteriors for each forcing variable; and panel (c) shows the time series of the latent state (red line) and length of pre-season (identified by the horizontal arrow).

3.3. Results

Overall, the model performed well across the study region (Fig. 3.3), with RMSEs between predicted versus observed onset of greenup ranging from 2.3 to 20.4 days, with a median of 4.9 days. The realism of these results implies that 1) the three climate variables used as predictors (i.e., daily mean temperature, day-length, and chilling units) represent

the primary controls on the timing of springtime phenology over the study region, and 2) the hierarchical structure of the model, which accommodates continuous changes in environmental forcing at daily time scale, effectively captures the processes underlying phenological events during dormancy and prior to the onset of leaf emergence during springtime. In this context, it's interesting to note that geographical patterns in model performance are clearly evident in these results. Specifically, model RMSEs tend to be slightly lower in northern regions, especially in central and eastern Canada, relative to RMSEs in southern regions (Fig 3.3a).

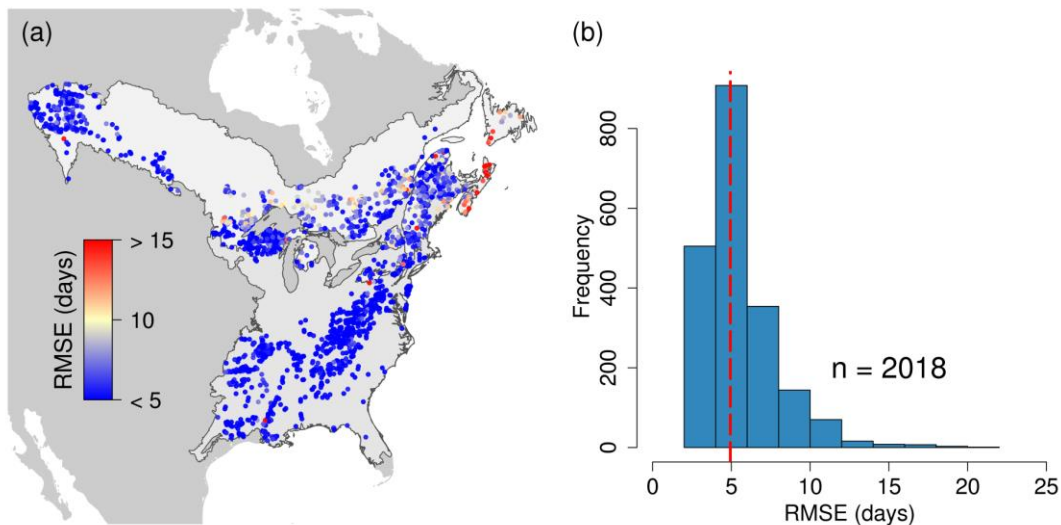


Fig. 3.3. Geographical pattern of model performance. RMSE is the root-mean square-error between the MODIS onset dates and onset dates from the model estimates. Vertical red line in panel (b) represents the median value ($n = 2,018$).

Fig. 3.4 shows the sensitivity of spring onset to each climate control. For thermal forcing, sensitivity is relatively uniform throughout the study region, with no clear geographical pattern aside from slightly lower sensitivity in eastern parts of the Northern Forest ecoregion and southern parts of the Eastern Temperate Forests ecoregion (Fig. 3.4a). Hence, I conclude that there is no meaningful difference in the sensitivity of greenup onset to thermal forcing between these two ecoregions (Fig. 3.4d). In contrast, the sensitivity to day-length shows distinct geographic patterns, with Eastern Temperate Forests showing markedly higher sensitivities relative to sensitivities estimated in Northern Forests (Fig. 3.4b and 3.4d). Central and Eastern Canada and New England, on the other hand, show relatively low sensitivity to day-length. The sensitivity of spring onset to chilling units is uniformly low throughout the study region, which indicates that chilling exerts second-order control on the timing of greenup relative to photoperiod and thermal forcing (Fig. 3.4c and 3.4d).

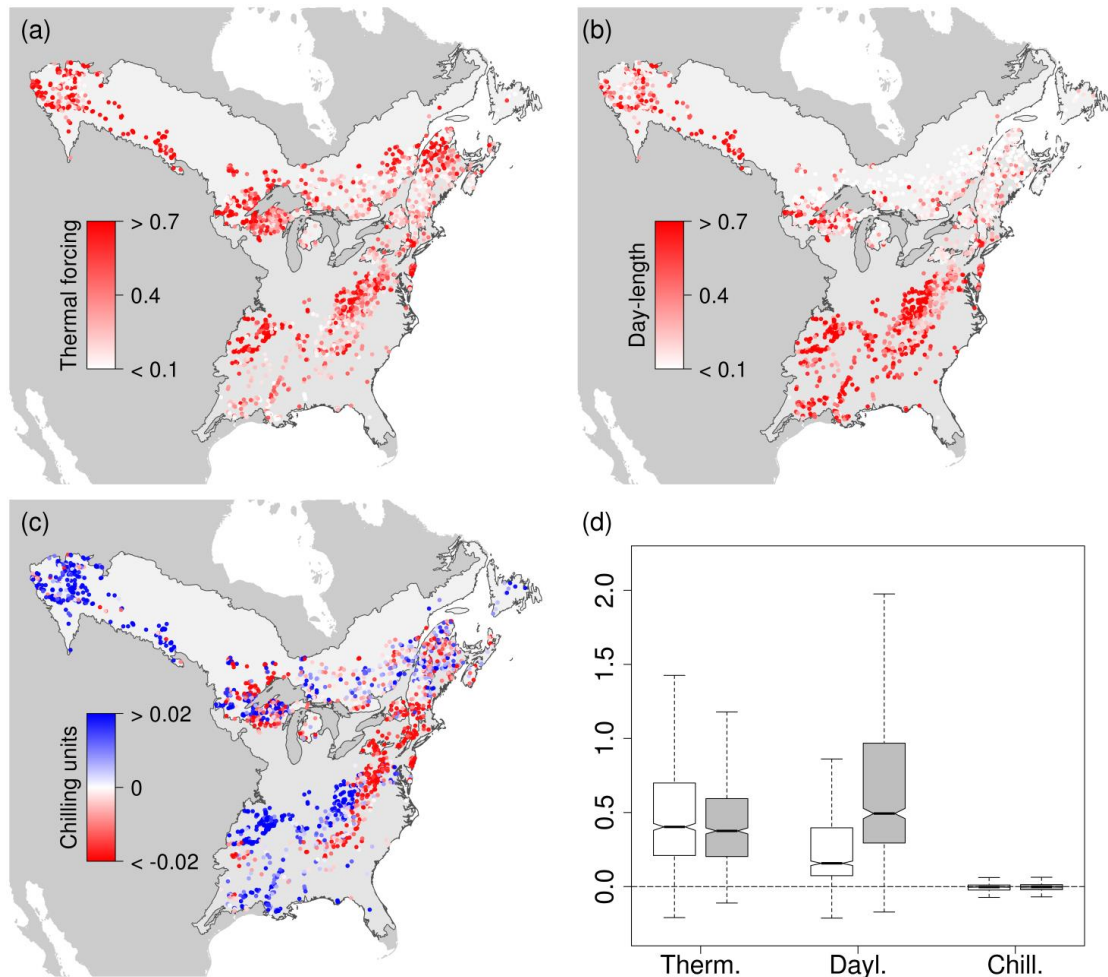


Fig. 3.4. Geographic sensitivity in the timing of greenup onset to different environmental forcing. Panels (a), (b), and (c) show geographical patterns in the sensitivity of greenup to thermal forcing, day-length, and chilling unit, respectively. In panel (d), the white and grey boxplots show the distribution of sensitivity to each forcing variable in Eastern Temperate Forests (grey) and Northern Forests (white); note that only day-length shows a statistically significant difference in sensitivity between the two ecoregions ($p < 0.001$).

To explore and illustrate both overall and geographic patterns in the relative importance of thermal forcing and day-length more deeply, I calculated normalized differences between the model coefficients for each forcing variable. Specifically, I computed this as:

$$\text{Relative Importance} = \frac{\beta_T - \beta_D}{\beta_T + \beta_D}$$

where β_T and β_D are the model coefficients for thermal forcing and day-length, respectively.

In Fig. 3.4a, the red and blue circles identify grid cells where thermal forcing or day-length is more important, respectively, where the size of each circle is proportional to the relative importance of each variable (i.e., the larger the circle, the greater the importance). Geographical patterns evident in Figure 3.5a clearly show that day-length exerts proportionally more control on the timing of springtime phenology in southern parts of the study region, while thermal forcing exerts more control in northern regions. Further, by plotting these results in climate space (i.e., as function of mean annual temperature and precipitation), the pattern becomes even more clear. In regions where mean annual temperature is above roughly 10 °C day-length is the most important control on spring onset. Conversely, in regions where mean annual temperature is less than 10 °C, thermal forcing is more important (Fig. 3.4b). In addition, most normalized differences located in the vicinity of 10 °C of mean annual temperature in Figure 3.5b are relatively small and red, which indicates that even though thermal forcing is more important, day-length exerts nearly equivalent control.

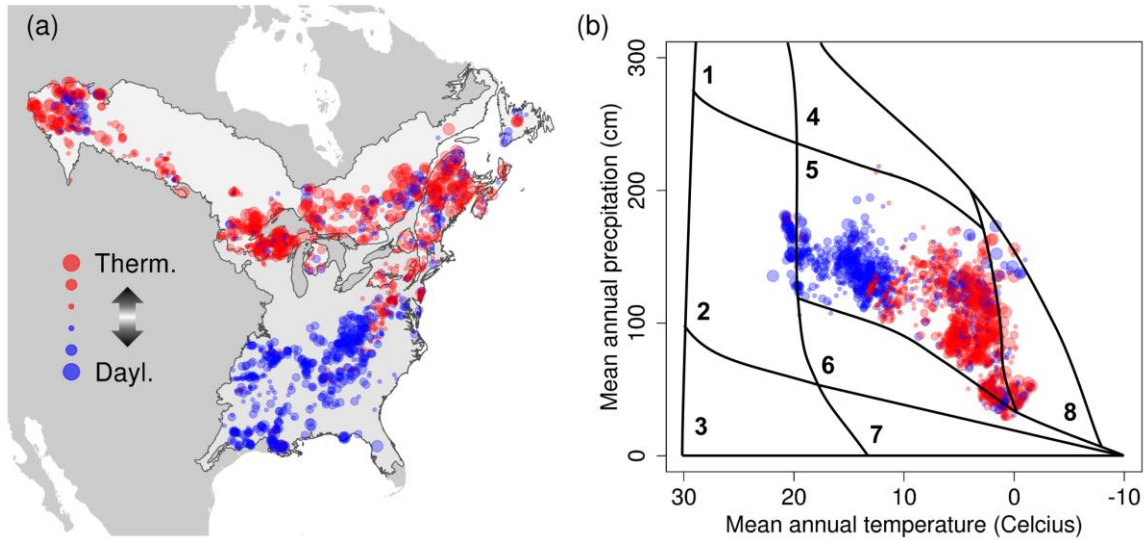


Fig. 3.5. Relative importance of thermal forcing versus day-length. The circles colored in red and blue represent the importance of thermal forcing and day-length, respectively; while the size of circles represents the relative importance of thermal forcing versus day-length (i.e., the bigger the size, the larger the importance). In panel (b), the lines and associated numbers identify the climate space of terrestrial biomes adapted from Gauthier et al. (2015): 1) tropical rain forest; 2) tropical seasonal forest/savanna; 3) subtropical desert; 4) temperate rain forest; 5) temperate seasonal forest; 6) woodland/shrubland; 7) temperate grassland/desert; 8) taiga.

Finally, pre-season period shows geographical patterns that are similar to patterns in the sensitivity of greenup to day-length, but the magnitudes are reversed (i.e., regions with higher sensitivity to day-length have shorter PSL, and vice versa; cf., Figs. 3.4a and 3.6a). Significantly, there is a strong negative correlation between the natural log of PSL and sensitivity to day-length ($R^2 = 0.76$, $p < 0.001$; Fig. 3.6b). In contrast, the relationship

between PSL and sensitivity to thermal forcing shows a much weaker relationship ($R^2 = 0.241$; data not shown).

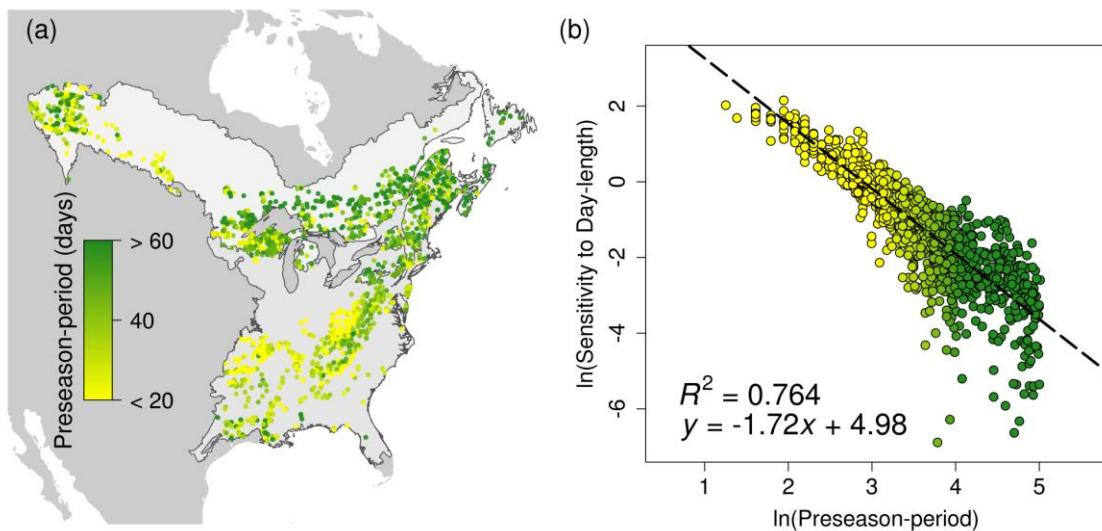


Fig. 3.6. Geographical pattern in pre-season-period (a) and the relationship between pre-season-period and sensitivity to day-length.

3.4. Discussion

3.4.1. Geographical variation in model performance

The model used in this study has two important attributes. First, it provides an effective way to explore how different environmental forcing variables influence the timing of spring greenup. Second, it provides a geographically explicit basis for characterizing uncertainty in the estimated sensitivity of greenup to each forcing variable included in the model. Previous work has shown that uncertainty in greenup onset dates provided by the MODIS Land Cover Dynamics product is relatively modest (i.e., ~5 days; Moon et al.,

2019). Hence, the contribution of uncertainty in MODIS Land Cover Dynamics data to uncertainty in model predictions is probably modest (although see below). At the same time, Fig. 3.3a clearly shows that model performance is markedly lower in central and eastern Canada, which begs the question: what is causing this pattern? While a precise answer is not directly inferable from the model results, two explanations are most likely. First, because of the way the model is defined, it's impossible for the latent state variable (h) to decrease. By definition, photoperiod increases monotonically during spring, which is consistent with the way that h is defined. Air temperatures (i.e., thermal forcing), on the other hand, can exhibit substantial day-to-day variation, including below-freezing temperatures. While not common, below normal temperatures can negatively impede phenological development through, for example, frost events.

In central and eastern Canada, where model uncertainty is highest, normalized sensitivities estimated by the model indicate that thermal forcing is the most important control on spring onset (i.e., relative to day-length and chilling units; Fig. 3.4). Thus, lower model performance in regions with higher sensitivity to thermal forcing may reflect the fact that the model specification does not capture how day-to-day variance in air temperatures affect springtime phenology. Second, challenges associated with detection and removal of pixels whose EVI2 values are affected by snow, especially in more open canopies typical of boreal forests, is a known source of uncertainty in the MODIS Land Cover Dynamics product (Moon et al., 2019). Hence, despite high overall quality in spring onset dates provided by the MODIS product, elevated model uncertainty in eastern and

central Canada in Fig. 3.3 may partly reflect higher uncertainty in the timing of spring onset estimated by the MODIS Land Cover Dynamics product.

3.4.2. The role of photoperiod on springtime phenology in a changing climate

The strong dependency of springtime phenology on air temperature in temperate biomes is well known (e.g., Lechowicz, 1984). However, recent studies have challenged this long-held understanding. In particular, Fu et al. (2015) and Piao et al. (2017) report that the sensitivity of springtime onset to temperature has decreased over the last several decades. Moreover, Fu et al. (2019) suggest that as the sensitivity of springtime onset to air temperatures has decreased the pre-season-period has also become shorter. To explain this result, Fu et al. (2019) hypothesize that the effect of photoperiod on phenological development during springtime has gradually increased as leaf-out dates have advanced, accompanied by diminished temperature control during the pre-season.

The results from this study provide empirical evidence that supports this hypothesis, but also identify several important additional implications. In particular, the results shown in Fig. 3.6 suggest that warmer regions tend to have shorter pre-season-periods, which are strongly and negatively correlated with sensitivity to day-length. In contrast, sensitivity of onset to thermal forcing shows no distinct geographical pattern over the study region and much weaker correlation with pre-season-periods. These results imply that as the climate has continued to warm, the influence of photoperiod on the timing of springtime phenology in temperate and boreal deciduous forests has increased because the

length of the pre-season-period has become shorter and not because the influence of thermal forcing has decreased.

Taking this one step further, if the climate continues to warm, the geographic extent where the influence of day-length on phenological development is dominant is likely to expand. Specifically, based on results shown in Fig. 3.5, regions where the mean annual temperature is at or just below 10 °C (e.g., from southern New England through Appalachia) are most likely to experience stronger photoperiod control on the timing of spring onset in the coming decades. This conclusion is supported by the fact that: (1) the relative importance of thermal forcing versus day-length exhibits a clear gradient that covaries with mean annual temperature (i.e., regions with higher mean annual temperatures have higher sensitivity to day-length) (Fig. 3.5); and (2) regions with mean annual temperature at or just below 10 °C tend to show negative sensitivity to chilling units, which acts to decelerate phenological development during the pre-season-period, thereby delaying spring onset. This suggests that chilling requirements may be unfulfilled in these regions, possibly as a result of recent warming.

The results of this study also raise questions related to the role of so-called safety mechanisms that have been ascribed to photoperiod controls on phenology. In particular, the results in Fig. 3.5a show that the sensitivity of greenup onset to day-length tends to be higher in warmer regions than in colder regions. Further, as I previously discussed, the relative importance of air temperature versus day-length shows clear patterns that follow gradients in mean annual temperature (Fig. 3.5b). These results support the argument posited by Zohner et al. (2016), who reported that temperate tree species with strong

photoperiod control on leaf-out tend to be from warmer regions. Consistent with Zohner et al., results from this study also challenge the idea that photoperiod provides a safeguard against early leaf emergence in temperate woody species (Körner and Basler, 2010; Laube et al., 2014; Saikkonen et al., 2012; Wang et al., 2014).

If this conclusion is correct, the question then becomes: *why is photoperiod relatively more important in controlling the timing of onset during springtime in warmer regions?* One explanation is provided by the “law of minimum”, which states that plant growth is controlled by the scarcest resource rather than by the total resources available (Liebig et al., 1841). In warmer regions (i.e., regions where mean annual temperature is greater than 10 °C; Fig. 3.5), temperature is much less limiting than in colder regions. Hence, another more limited resource may provide the primary control on physiological activities (i.e., light resource in this case). This explanation is supported by several recent studies that have examined the relationship between the seasonality of vegetation and climatic constraints. For example, Jones et al. (2014) suggest that the seasonality of Amazon forests strongly depends on water and light availability. Even though this study was conducted in a very different biome relative to the temperate and boreal forests considered in this paper, it provides a good example of vegetation phenology dependency on resource availability. Similarly, Park et al. (2019) suggest that the seasonality in photosynthetic activity at high latitudes is largely controlled by climatic constraints. More specifically, Park et al. suggest that extensive areas of high-latitude ecosystems that were previously temperature-constrained are increasingly sensitive to photoperiod. As a result, the timing of seasonal peak photosynthetic activity has advanced over the northern

circumpolar region over the last few decades (-1.66 ± 0.30 days/decade). Finally, Keenan and Riley (2018) have suggested that the area of vegetated land that is limited by temperature has declined by 16.4% over the last three decades, implying that temperature constraints and controls on vegetation growth have systematically decreased over much of the globe.

3.5. Conclusions

In this study, I developed and applied a state-space Bayesian modeling framework to address the question of how different climate controls affect the timing of springtime phenology over the entire temperate deciduous forests of North America for the period 2001 to 2017. Results suggest that the Eastern Temperate Forest ecoregion, which is warmer than the Northern Forest ecoregion included in the study, has a shorter pre-season period, which induces higher sensitivity in the timing of greenup onset to climate forcing. Further, I found that day-length is more important in warmer regions than in colder regions, which contradicts the widely held hypothesis that photoperiod provides a key safety mechanism preventing early leaf-out during springtime. These results provide geographically explicit patterns that characterize the magnitude of influence of different controls on springtime phenology, along with spatially explicit insights regarding how the timing of phenological onset during springtime will change as the climate continues to warm in the coming decades.

4. MODIFICATION OF SURFACE ENERGY BALANCE DURING SPRINGTIME: THE RELATIVE IMPORTANCE OF BIOPHYSICAL AND METEOROLOGICAL CHANGES

4.1. Introduction

Changes in the surface energy balance during phenological transition periods have been previously documented (e.g., Fitzjarrald et al., 2001; Moore et al., 1996; Pielke et al., 1998; Ryu et al., 2008; Schwartz and Crawford, 2001; Wilson and Baldocchi, 2000). However, most of these previous studies are empirical, and none provide a physically-based framework for quantifying how the independent and joint contributions of changes in surface biophysical and meteorological properties influence changes in surface energy balance. Development of such a framework is challenging because vegetation phenology modulates a number of biophysical properties and meteorological processes concurrently. In particular, increased available energy from solar radiation during springtime causes air temperatures to increase, which triggers leaf emergence (Chuine et al., 2013; Friedl et al., 2014). At the same time, higher evaporative demand and canopy conductance from leaves in the vegetation canopy lead to greater partitioning of available energy into evaporative fluxes (Monteith & Unsworth, 2013). Changes in surface albedo and roughness associated with leaf emergence introduce additional complexity. For example, increasing (decreasing) albedo will decrease (increase) available energy by reflecting (absorbing) more solar radiation from the surface, while an increase in the roughness length will enable more

efficient transfer of sensible and latent heat from the surface to the atmosphere (Bonan, 2008).

Energy balance-based approaches have been widely used to study how the surface energy balance is modified by land use and land cover change (e.g., deforestation and urbanization; Chen and Dirmeyer, 2016; Devaraju et al., 2018; Lee et al., 2011; Li et al., 2019; Liao et al., 2018; Luysaert et al., 2014; Zhao et al., 2014). Notably, the Intrinsic Biophysical Mechanism (IBM) method proposed by Lee et al. (2011) has been used to separate surface biophysical effects into three components: radiative forcing, aerodynamic resistance, and partitioning of available energy between latent and sensible heat fluxes via the Bowen ratio. However, the IBM method does not account for atmospheric feedbacks to the surface energy balance (Chen & Dirmeyer, 2016). In addition, Rigden & Li (2017) suggested that this method overestimates the contribution of aerodynamic resistance by assuming independence between aerodynamic resistance and the Bowen ratio. To overcome this, Rigden & Li (2017) proposed a new method called the Two-Resistance Mechanism (TRM) method, which replaces the Bowen ratio with the surface resistance. Using the TRM method, Liao et al. (2018) showed that atmospheric feedbacks significantly impact the surface temperature, and therefore need to be accounted for when examining how land use and land cover change affect the surface energy balance. Li & Wang (2019) further demonstrated that atmospheric feedbacks introduce scale-dependence in surface temperature changes induced by land use and land cover change. To date, however, these methods have not been used to study surface energy balance dynamics during springtime,

when the surface radiation and energy balance, atmospheric properties, and surface properties are rapidly changing.

In this study, I address two key questions: (1) how does leaf emergence affect surface properties and meteorological conditions across different vegetation types? And (2) what is the relative importance, contribution, and interactions among different land surface and atmospheric variables on springtime changes in surface energy balance? To address these questions, I present an analytical framework based on the TRM method that diagnoses and quantifies the role of key atmospheric and surface biophysical factors in regulating changes in the surface energy balance that occur during the period of leaf emergence. Compared to the original TRM method used in Rigden & Li (2017) and Liao et al. (2018), changes in atmospheric conditions are explicitly and more thoroughly considered in the approach I use here. I apply this revised method to 212 site-years of data from 42 AmeriFlux sites located in the contiguous United States and Eastern Canada that span a wide range of climate regimes and six vegetation types.

4.2. Methods and data

4.2.1. Attribution method

I focus on changes in the Bowen ratio (β), which is defined as the ratio of sensible heat flux to latent heat flux. To perform my analysis, I modify the TRM method originally described by Rigden & Li (2017) to account for variations in atmospheric properties such that changes in β can be attributed to changes in surface and atmospheric properties.

Specifically, the TRM method starts from the surface radiation and energy balance equations, which are given by

$$R_n = S_{in}(1 - \alpha) + \varepsilon L_{in} - \varepsilon \sigma T_s^4 = H + LE + G \quad (4.1)$$

where R_n is the net surface radiation, S_{in} is the incoming shortwave radiation, α is the surface albedo, ε is the emissivity, L_{in} is the incoming longwave radiation, σ is the Stefan-Boltzmann constant, T_s is the land surface temperature, H is the sensible heat flux, LE is the latent heat flux, and G is the ground heat flux. The sensible and latent heat fluxes are then parameterized using the resistance concepts as follows

$$H = \frac{\rho c_p}{r_a} (T_s - T_a) \quad (4.2)$$

$$LE = \frac{\rho L_v}{(r_a + r_s)} (q_s^*(T_a) - q_a) \quad (4.3)$$

where ρ is the air density, c_p is the specific heat of air at constant pressure, r_a is the aerodynamic resistance, T_a is the air temperature, L_v is the latent heat of vaporization, q_s^* is the saturated specific humidity at T_a , q_a is the atmosphere specific humidity, and r_s is the surface or canopy resistance. Substituting H and LE into equation (4.1) and linearizing the outgoing longwave radiation term and the saturated specific humidity term yields analytical expressions for T_s and β

$$T_s = \frac{\lambda_o \left[S_{in}(1 - \alpha) + \varepsilon L_{in} - \varepsilon \sigma T_a^4 - G - \frac{\rho L_v}{(r_a + r_s)} (q_a^*(T_a) - q_a) \right]}{1 + \frac{r_o}{r_a} \left[1 + \frac{\delta}{\gamma} \left(\frac{r_a}{r_a + r_s} \right) \right]} + T_a \quad (4.4)$$

$$\beta = \frac{c_p(T_s - T_a)}{\left(\frac{r_a}{r_a + r_s}\right) L_v(q_s^*(T_a) - q_a)} \quad (4.5)$$

where $\lambda_o = \frac{1}{4\varepsilon\sigma T_a^3}$, $r_o = \rho c_p \lambda_o$, $\delta = \left. \frac{\partial e^*}{\partial T} \right|_{T_a}$, $\gamma = \frac{c_p P}{0.622 L_v}$, e^* is the saturation vapor pressure, and P is the air pressure. Substituting T_s into equation (4.5) and taking the first-order derivative of equation (4.5), I obtain the following equation:

$$\begin{aligned} \Delta\beta = & \frac{\partial\beta}{\partial S_{in}} \Delta S_{in} + \frac{\partial\beta}{\partial L_{in}} \Delta L_{in} + \frac{\partial\beta}{\partial q_a} \Delta q_a + \frac{\partial\beta}{\partial T_a} \Delta T_a + \frac{\partial\beta}{\partial G} \Delta G + \frac{\partial\beta}{\partial r_a} \Delta r_a \\ & + \frac{\partial\beta}{\partial r_s} \Delta r_s + \frac{\partial\beta}{\partial \alpha} \Delta \alpha \end{aligned} \quad (4.6)$$

In this equation, Δ refers to changes in each variable over time (e.g., $\Delta\alpha = \alpha_{after} - \alpha_{before}$; in this case before and after springtime emergence of leaves) and the partial derivatives (e.g., $\partial\beta/\partial\alpha$) quantify the sensitivity of β to changes in each variable. The analytical expressions for the partial derivatives are too complex to be included here but can be easily obtained numerically. The novelty of this attribution method is that this approach considers biophysical and atmospheric changes more comprehensively (i.e., inclusion of contributions from changes in specific humidity, albedo, and incoming long- and short-wave radiation) relative to the methods used in Liao et al. (2018) and Rigden & Li (2017).

4.2.2. Estimation of changes in surface and atmospheric properties

I apply the refined TRM method to 212 site-years of meteorological and flux data from 42 eddy covariance sites located in the conterminous United States and Eastern Canada that span a wide range of climates and six vegetation types: deciduous broadleaf forest, evergreen needleleaf forest, mixed forest, croplands, grasslands, and shrublands (Table 4.1). Liao et al. (2018) found that the TRM-based attribution cannot be applied to data at half-hourly time scale because the available energy (i.e., the sum of sensible and latent heat fluxes) outside of the mid-day periods can be quite low, thus some modeled quantities during these periods, especially the aerodynamic and surface resistance terms, can have high uncertainties in the 30-min data. By computing daily averages, these uncertainties are reduced. Hence, in this study, I aggregate the 30-min data to daily averages using data from daytime conditions when incoming shortwave radiation is larger than 25 W m^{-2} . I also remove any data for which the estimated resistances are negative at daily scale. To measure changes before and after leaf emergence, I use the daily data to estimate mean daily values for 30-day periods before and after leaf emergence at each site, and perform the attribution analysis based on these data.

Table 4.1 List of AmeriFlux sites. IGBP denotes the International Geosphere-Biosphere Program land cover type classification: CRO: cropland; DBF: deciduous broadleaf forest; ENF: evergreen needleleaf forest; GRA: grassland; MF: mixed forest; SH: shrubland.

Site Name	Latitude	Longitude	IGBP	Reference
Bondville (US-Bo1)	40.006	-88.290	CRO	Meyers & Hollinger (2004) doi:10.17190/AMF/1246036

Bondville Companion site (US-Bo2)	40.009	-88.290	CRO	Bernacchi et al. (2005) doi:10.17190/AMF/1246037
Brooks Field Site 10 (US-Br1)	41.975	-93.691	CRO	Chu et al. (2018) doi:10.17190/AMF/1246038
Brooks Field Site 11 (US-Br3)	41.975	-93.694	CRO	Chu et al. (2018) doi:10.17190/AMF/1246039
Curtice Walter-Berger cropland (US-CRT)	41.629	-83.347	CRO	Chu et al. (2018) doi:10.17190/AMF/1246156
Mead Irrigated Continuous Maize (US-Ne1)	41.165	-96.477	CRO	Suyker et al. (2005) doi:10.17190/AMF/1246084
Mead Irrigated Maize-Soybean Rotation (US-Ne2)	41.165	-96.470	CRO	Suyker et al. (2005) doi:10.17190/AMF/1246085
Mead Rainfed Maize-Soybean Rotation (US-Ne3)	41.18	-96.440	CRO	Suyker et al. (2005) doi:10.17190/AMF/1246086
Rosemount G21 (US-Ro1)	44.714	-93.090	CRO	Baker & Griffis (2005) doi:10.17190/AMF/1246092
Sioux Falls Portable (US-SFP)	43.241	-96.902	CRO	Euskirchen et al. (2017) doi:10.17190/AMF/1246126
Twitchell Alfalfa (US-Tw3)	38.116	-121.647	CRO	Hemes et al. (2019) doi:10.17190/AMF/1246149
Twitchell Corn (US-Tw2)	38.105	-121.643	CRO	Baldocchi & Penuelas (2019) doi:10.17190/AMF/1246148
Chestnut Ridge (US-ChR)	35.931	-84.332	DBF	Euskirchen et al. (2017) doi:10.17190/AMF/1246044
Duke Forest Hardwoods (US-Dk2)	35.974	-79.100	DBF	Oishi et al. (2008) doi:10.17190/AMF/1246047
Missouri Ozark Site (US-MOz)	38.744	-92.200	DBF	Wood et al. (2019) doi:10.17190/AMF/1246081
Morgan Monroe State Forest (US-MMS)	39.323	-86.413	DBF	Zhang et al. (2018) doi:10.17190/AMF/1246080
Oak Openings (US-Oho)	41.555	-83.844	DBF	Chu et al. (2016) doi:10.17190/AMF/1246089
Ontario Turkey Point Mature Deciduous (CA-TPD)	42.635	-80.558	DBF	Chu et al. (2018) doi:10.17190/AMF/1246152
Silas Little New Jersey (US-Slt)	39.914	-74.596	DBF	Clark et al. (2018) doi:10.17190/AMF/1246096
UMBS Disturbance (US-UMd)	45.563	-84.698	DBF	Gough et al. (2013) doi:10.17190/AMF/1246134
Michigan Biological Station (US-UMB)	45.56	-84.714	DBF	Gough et al. (2013) doi:10.17190/AMF/1246107
Walker Branch Watershed (US-WBW)	35.959	-84.287	DBF	Gu et al. (2008) doi:10.17190/AMF/1246109
Duke Forest Loblolly Pine (US-Dk3)	35.978	-79.094	ENF	Oishi et al. (2008) doi:10.17190/AMF/1246048
GLEES (US-GLE)	41.367	-106.24	ENF	Frank et al. (2014) doi:10.17190/AMF/1246056
GLEES Brooklyn Tower (US-GBT)	41.366	-106.24	ENF	Zeller (2000) doi:10.17190/AMF/1375200
Howland Forest (harvest site, US-Ho3)	45.207	-68.725	ENF	Thornton et al. (2002) doi:10.17190/AMF/1246063
Howland Forest (main tower, US-Ho1)	45.204	-68.740	ENF	Hollinger et al. (2004) doi:10.17190/AMF/1246061
Howland Forest (west tower, US-Ho2)	45.209	-68.747	ENF	Xiao et al. (2004) doi:10.17190/AMF/1246062
Mary's River (Fir) site (US-MRf)	44.647	-123.552	ENF	Kwon et al. (2018) doi:10.17190/AMF/1246049
NC Clearcut#3 (US-NC3)	35.799	-76.656	ENF	Euskirchen et al. (2017) doi:10.17190/AMF/1419506
NC Loblolly Plantation (US-NC2)	35.803	-76.669	ENF	Noormets et al. (2010) doi:10.17190/AMF/1246083
Ontario Turkey Point 1939 Plantation (CA-TP4)	42.710	-80.357	ENF	Peichl et al. (2010) doi:10.17190/AMF/1246012
Brookings (US-Bkg)	44.345	-96.836	GRA	Gilmanov et al. (2005) doi:10.17190/AMF/1246040
Canaan Valley (US-CaV)	39.063	-79.421	GRA	Euskirchen et al. (2017) doi:10.17190/AMF/1246042
Cottonwood (US-Ctn)	43.95	-101.847	GRA	Euskirchen et al. (2017) doi:10.17190/AMF/1246117

Duke Forest Open Field (US-Dk1)	35.971	-79.093	GRA	Oren et al. (2006) doi:10.17190/AMF/1246046
Goodwin Creek (US-Goo)	34.255	-89.874	GRA	Runkle et al. (2017) doi:10.17190/AMF/1246058
Kansas Field Station (US-KFS)	39.056	-95.191	GRA	Wolf et al. (2016) doi:10.17190/AMF/1246132
KUOM Turfgrass Field (US-KUT)	44.995	-93.186	GRA	Hiller et al. (2011) doi:10.17190/AMF/1246145
Ontario Groundhog River (CA-Gro)	48.217	-82.156	MF	McCaughey et al. (2006) doi:10.17190/AMF/1245996
RCEW Mountain Big Sagebrush (US-Rms)	43.065	-116.749	SH	Euskirchen et al. (2017) doi:10.17190/AMF/1375202
NC Clearcut (US-NC1)	35.812	-76.712	SH	Noormets et al. (2012) doi:10.17190/AMF/1246082

All the inputs needed for the attribution analysis are estimated using data from the AmeriFlux database (<https://ameriflux.lbl.gov>; Table 4.1) following Wang et al. (2019). In particular, aerodynamic and surface resistances are inferred from sensible and latent heat flux measurements, as well as temperature and humidity measurements, using Eqs. (4.2) and (4.3). Ground heat fluxes are assigned the residual of the surface energy balance to ensure surface energy budget closure. Hence the contribution of ground heat flux implicitly includes the role of surface energy imbalance or non-closure (see Foken 2008 for review). Where available, I use the soil heat flux measurements to represent ground heat flux, which are available at 34 out of 42 sites. As I show below, the results are not significantly affected in either case due to the small sensitivity of Bowen ratio to changes in ground heat flux.

4.2.3. Optimization of attribution method

Prior to applying the attribution method, I optimize my procedure for estimating partial derivatives using a weighted average approach described by Liao et al. (2018). This is needed because the attribution method is based on first-order Taylor series expansions

that neglect higher-order and cross-order terms. Hence, this approach is acceptable only if changes in the attribution variables are small. However, because changes in land surface and atmospheric properties can be significant during springtime, the partial derivatives estimated at the reference state (in this case before the emergence of leaves) can cause large errors in modeled changes in the Bowen ratio (Liao et al., 2018). To account for this, I optimize the partial derivatives for each site so that the calculated root-mean-square errors for changes in β are minimized. Specifically, the partial derivatives in the attribution model are calculated as

$$X = \frac{X_{before} + mX_{after}}{1 + m} \quad (4.7)$$

where X is the final partial derivative used in the model, m is the average weight, and X_{before} and X_{after} are the partial derivatives calculated only using data from time periods before and after springtime phenology, respectively.

4.2.4. Springtime phenology

The timing of springtime leaf emergence is identified at each site using the Collection 6 MODIS Land Cover Dynamics (i.e., land surface phenology) product (MCD12Q2; Moon et al., 2019). A number of studies have evaluated the MODIS phenology algorithm and have demonstrated that it shows good agreement with ground-based phenophase transition observations (Ganguly et al., 2010; Richardson et al., 2018c). The algorithm uses panelized cubic splines to interpolate daily time series of the two-band

Enhanced Vegetation Index (EVI2) at each 500 m pixel, which is computed from the Collection 6 MODIS normalized BRDF-adjusted surface reflectance (NBAR) values (MDC43A4; Wang et al., 2018). In the MCD12Q2 product, phenological transition dates are estimated to occur when the EVI2 time series at each pixel cross assigned thresholds in the seasonal amplitude of EVI2. In this study, I define the timing of leaf emergence as the day of year when EVI2 time series cross 50% of the seasonal amplitude during the “green-up” phase. Note that even though the timing of 15% of the seasonal amplitude provides a closer approximation of the timing of leaf emergence (as shown Fig. 4.1a), I use 50% as the threshold because sensible and latent heat fluxes around the 15% threshold tend to be small, which can introduce large uncertainties in the inferred variables, especially aerodynamic and surface resistances. Lastly, to minimize errors from geolocation and product uncertainty, I use the average green-up date from 3 by 3 windows of MODIS pixels centered over each flux tower location.

4.2.5. Attribution of changes in aerodynamic resistance

In section 4.3.3, I attribute changes in aerodynamic resistance (r_a) following the basic approach used to attribute changes in β (Eq. 4.6). Using Monin-Obukhov similarity theory, r_a can be parameterized as a function of wind speed (u), momentum roughness length (z_o), and thermal roughness length (z_{oh}):

$$r_a = \frac{1}{\kappa^2 u} \left[\log \left(\frac{z-d}{z_o} \right) - \Psi_m \left(\frac{z-d}{L} \right) + \Psi_m \left(\frac{z_o}{L} \right) + \hat{\Psi}_m(z, L) \right] \quad (4.8)$$

$$\left[\log \left(\frac{z-d}{z_{oh}} \right) - \Psi_m \left(\frac{z-d}{L} \right) + \Psi_h \left(\frac{z_{oh}}{L} \right) + \hat{\Psi}_h(z, L) \right]$$

where κ is the von-Karman constant, z is the measurement height, d is the displacement height (assumed to be 70% of the vegetation height), L is the Obukhov length, and Ψ_m and Ψ_h are stability correction functions for momentum and heat, respectively, based on the Businger-Dyer relations (Brutsaert, 2005; Garratt, 1992). The correction functions $\hat{\Psi}_m(z, L)$ and $\hat{\Psi}_h(z, L)$ are included to account for roughness sublayer effects for momentum and heat, respectively (Arnqvist and Bergström, 2015; Harman and Finnigan, 2007). To use equation (4.8), I need to estimate the changes in roughness lengths, atmospheric stabilities, and roughness sublayers. The roughness lengths are estimated following Rigden et al. (2018), but including the correction for roughness sublayer. For atmospheric stabilities, the Obukhov length is defined as

$$L = \frac{-u_*^3 \rho T_a (1 + \eta q_a) c_p}{\kappa g H} \quad (4.9)$$

where η ($= 0.61$) is the dimensionless ratio of the gas constants for dry air to water vapor, and g is the gravitational acceleration. The stability correction functions Ψ_m and Ψ_h are then calculated from the dimensionless stability parameter ξ ($= z/L$) as follows, with $x = (1 - 16\xi)^{1/4}$:

$$\Psi_m = \begin{cases} \ln \left[\left(\frac{1+x^2}{2} \right) \left(\frac{1+x}{2} \right)^2 \right] - 2 \tan^{-1} x + \frac{\pi}{2} & \text{for } \xi < 0 \\ -5\xi & \text{for } \xi \geq 0 \end{cases} \quad (4.10)$$

$$\Psi_h = \begin{cases} 2 \ln \left(\frac{1+x^2}{2} \right) & \text{for } \xi < 0 \\ -5\xi & \text{for } \xi \geq 0 \end{cases} \quad (4.11)$$

The roughness sublayer correction functions $\hat{\Psi}_m(z, L)$ and $\hat{\Psi}_h(z, L)$ are calculated following De Ridder (2010) as

$$\hat{\Psi}_i(z, L) = \Phi_i \left[\left(1 + \frac{\nu}{\mu_i z / z_*} \right) \frac{z}{L} \right] \frac{1}{\lambda} \ln \left(1 + \frac{\lambda}{\mu_i z / z_*} \right) e^{-\mu_i z / z_*} \quad (4.12)$$

where i is an index indicating momentum (m) or heat (h) and Φ is the surface-layer stability function defined in De Ridder (2010). ν , μ , and λ are the correction coefficients and z_* is the roughness sublayer height above the displacement height, and I use these parameters as constants with values from De Ridder (2010). Taking the derivative of equation (4.8), I obtain the following equation:

$$\begin{aligned} \Delta r_a = & \frac{\partial r_a}{\partial u} \Delta u + \left(\frac{\partial r_a}{\partial \Psi_m} \Delta \Psi_m + \frac{\partial r_a}{\partial \Psi_h} \Delta \Psi_h + \frac{\partial r_a}{\partial L} \Delta L + \frac{\partial r_a}{\partial \hat{\Psi}_m} \Delta \hat{\Psi}_m + \frac{\partial r_a}{\partial \hat{\Psi}_h} \Delta \hat{\Psi}_h \right) \\ & + \left(\frac{\partial r_a}{\partial z_o} \Delta z_o + \frac{\partial r_a}{\partial z_{oh}} \Delta z_{oh} \right) \end{aligned} \quad (4.13)$$

Hence, Eq. 4.13 quantifies the relative contributions from changes in wind speed (the first term, right-hand side of Eq. 4.13), atmospheric stability including roughness sublayer corrections (second term), and roughness lengths for heat and momentum (third term) to changes in aerodynamic resistance. I apply this method to data from 10 deciduous broadleaf forest sites, where vegetation height information is available and where vegetation heights are relatively stable compared to other vegetation types (e.g., croplands) during springtime.

4.3. Results and discussion

4.3.1. Changes in surface and atmospheric properties during springtime

To illustrate springtime dynamics typical of those observed at AmeriFlux sites included in my analysis, Fig. 1 shows daily values of biophysical and meteorological properties during a 120-day period centered on the timing of leaf emergence at the Morgan-Monroe State Forest site (US-MMS, DBF), averaged from 2001 to 2014. Vegetation index (i.e., EVI2) values estimated from MODIS are also shown, which increase gradually throughout the springtime. Land surface temperature (T_s) increases throughout the springtime, although the rate of change decreases around the time when EVI2 values start to increase (i.e., around -15 days on the x-axis of Fig. 4.1). Similarly, the daytime Bowen ratio (β) decreases monotonically throughout the spring period, with a distinct drop around the time that the rate of change in T_s decreases. Radiation forcing (i.e., incoming shortwave and longwave radiation) and specific humidity also increase monotonically during springtime, and ground heat flux and albedo are relatively constant. Surface resistance and wind speed decrease sharply after leaf emergence, while aerodynamic resistance increases after leaf emergence (i.e., around 0 on the x-axis of Fig. 4.1). Note that the surface resistance drops consistently (over more than a month) during the springtime in proportion to EVI2 increase, which is consistent with the pattern previously reported by Sakai et al. (1997).

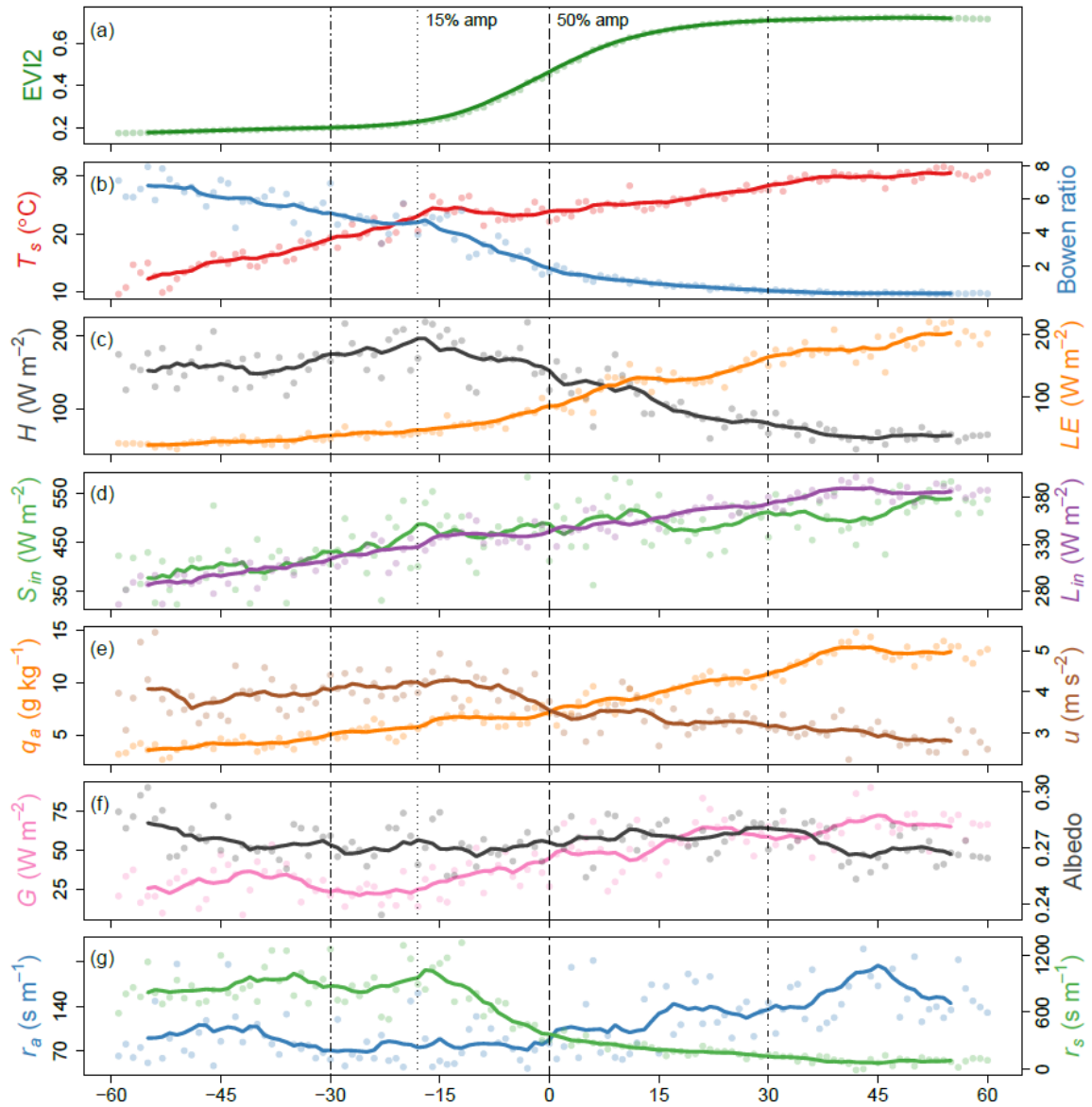


Fig. 4.1. Changes in biophysical and meteorological properties 60 days before and after leaf emergence at the Morgan-Monroe State Forest site averaged from 2001 to 2014. EVI2, T_s , H , LE , S_{in} , L_{in} , q_a , u , G , r_a , and r_s represent vegetation index, land surface temperature, sensible heat flux, latent heat flux, incoming shortwave radiation, incoming longwave radiation, specific humidity, wind speed, ground heat flux, aerodynamic resistance, and surface resistance, respectively. Dots and lines represent 14-year averaged values and 10-

day moving averages, respectively. Vertical dotted lines near 15 days before leaf emergence represent 15% of the seasonal EVI2 amplitude. Note that the values are estimated from daytime conditions.

In general, the patterns shown in Fig. 4.1 are consistent across all of the plant functional types included in my analysis (Table 4.2). On average, incoming longwave radiation, air temperature, specific humidity, and aerodynamic resistance all increase during springtime, while surface resistance decreases. Changes in ground heat flux and albedo are fairly small. In addition, wind speed generally decreases during springtime across all vegetation types, including evergreen needleleaf forest sites where changes in surface properties are modest.

Table 4.2 Springtime phenology and changes in biophysical and meteorological properties after leaf emergence.

Vegetation Type	n	SOS	ΔS_{in}	ΔL_{in}	Δq_a	ΔT_a	ΔG	Δr_a	Δr_s	$\Delta \alpha$	Δu
DBF	66	125(12)	25(62)	31(15)	3.1(1.5)	4.9(3.1)	14(19)	15(18)	-315(95)	-0.001(0.020)	-0.6(0.4)
ENF	43	142(21)	15(76)	31(17)	2.8(1.4)	4.8(2.4)	-9(8)	3(8)	-43(82)	-0.015(0.021)	-0.4(0.5)
MF	10	154(6)	0(42)	38(11)	3.3(1.0)	5.9(2.2)	10(9)	23(9)	-138(83)	-0.001(0.009)	-0.5(0.5)
CRO	68	160(21)	34(50)	23(14)	3.2(1.7)	3.6(2.4)	13(39)	36(39)	-232(214)	-0.019(0.033)	-1.2(0.9)
GRA	20	124(16)	-15(80)	32(19)	3.2(1.7)	4.1(3.0)	10(49)	43(49)	-132(70)	-0.034(0.024)	-0.6(0.6)
SH	5	123(7)	-35(65)	35(15)	3.1(1.0)	3.0(2.0)	13(8)	17(8)	-142(102)	-0.022(0.017)	-0.4(0.4)

DBF: deciduous broadleaf forest; ENF: evergreen needleleaf forest; MF: mixed forest; CRO: cropland; GRA: grassland; SH: shrubland; n: number of site-year; SOS: springtime phenology (day of year); S_{in} : incoming shortwave radiation (W m^{-2}); L_{in} : incoming longwave radiation (W m^{-2}); q_a : specific humidity (g kg^{-1}); T_a : air temperature ($^{\circ}\text{C}$); G : ground heat flux (W m^{-2}); r_a : aerodynamic resistance (s m^{-1}); r_s : surface resistance (s m^{-1}); α : albedo (-); u : wind speed (m s^{-1}). Values in parentheses indicate one standard deviation.

However, there are notable differences in specific terms across vegetation types. In particular, deciduous broadleaf forests and croplands exhibited the largest decreases in surface resistance, followed by shrublands, mixed forests, grasslands, and evergreen needleleaf forests (Table 4.2). Unsurprisingly, some of these differences are caused by differences in the magnitude of seasonal variation in leaf area across vegetation types. Fig. 4.2 shows that observed decreases in surface resistance across vegetation types are strongly correlated with the amplitude of seasonal variation in EVI2 values over the growing season ($R^2 = 0.754, p = 0.025$).

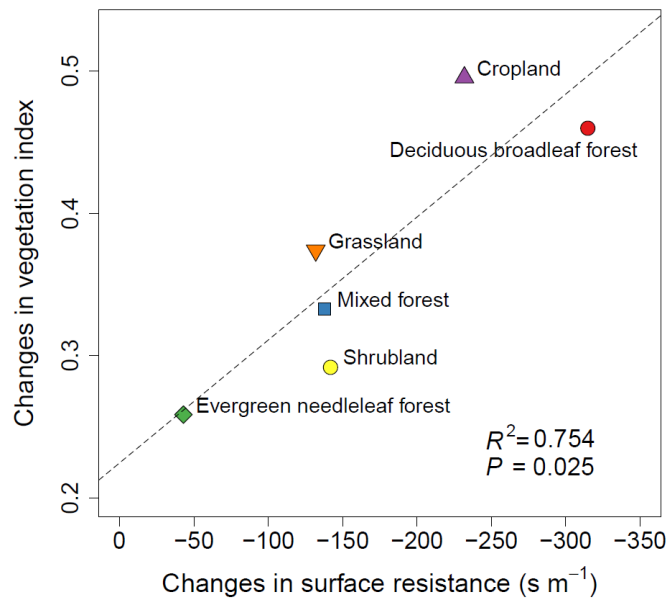


Fig. 4.2. Relationship between changes in surface resistance and vegetation index (EVI2). Each point represents the average change for each vegetation type. Changes in EVI2 values are computed based on the average EVI2 value in 3 by 3 MODIS pixel windows centered over each flux tower.

4.3.2. Attribution of decreases in the Bowen ratio

The TRM framework provides an effective framework for decomposing and quantifying the relative contributions of land surface and atmospheric properties to changes in the surface energy balance (e.g., Li et al., 2019; Liao et al., 2018). In this study, I refine the TRM method to incorporate associated changes in surface properties as well as atmospheric conditions more thoroughly (i.e., inclusion of the effects of changes in specific humidity, albedo, and two incoming radiations). Fig. 4.3 shows results from this method that attribute changes in β to contributions from changes in surface properties and atmospheric conditions. Each panel presents results summarized by vegetation type.

As leaves emerge, partitioning of available energy increasingly favors latent heat flux from transpiration. This is reflected in the strong negative contributions from changes in surface resistance to the Bowen ratio as shown in Fig. 4.3. In this study, the surface resistance is parameterized using a simple big-leaf representation and hence includes both soil and vegetation conditions, which has been traditionally parameterized as a function of leaf area and various stressors (e.g., soil water content and vapor pressure deficit; Jarvis et al., 1976; Monteith and Unsworth, 2013; Stewart, 1988). Fig. 4.2 shows that the observed springtime decrease in surface resistance is largely caused by increases in leaf area, suggesting that the surface resistance in my analysis primarily reflects the surface biophysical conditions instead of atmospheric conditions.

My results also demonstrate that decreases in β are the product of interplay among a number of related variables rather than being regulated by a single element such as changes in leaf area. For example, atmospheric evaporative demand increases as air

temperature increases, which increases evapotranspiration and decreases β . Concurrently, increases in specific humidity impose a negative feedback on evaporative fluxes, which partly offsets the influence of higher air temperatures and lower surface resistances. The contributions of aerodynamic resistance are consistently negative (i.e., they act to decrease β), implying that larger aerodynamic resistance tends to inhibit sensible heat flux more strongly than latent heat flux. While these features are quite consistent across vegetation types, the magnitude of $\Delta\beta$ is quite different, with deciduous broadleaf forests showing the largest changes in β versus other vegetation types (i.e., larger decreases in DBF and MF than in ENF, CRO, CRA, and SH, Fig. 4.3). This result is partly related to the fact that different vegetation types have different magnitudes of increase in leaf area (see Fig. 4.2) and also that β tends to be larger prior to leaf emergence at forested sites (especially at DBF sites) than at non-forest sites (Table 4.3).

In contrast, the influence of changes in shortwave and longwave radiation, ground heat flux, and albedo on β are small. For radiative fluxes, because β is the ratio of the two turbulent flux terms (i.e. the Bowen ratio), the impact of changes in radiation on β is expected to be small. In addition, the small influence from ground heat flux suggests that lack of surface energy balance closure is not important in my attribution analysis. Recall that I calculated the ground heat flux at each site as residual of the surface energy. In parallel, I also conducted the same analysis using soil heat flux measurements for the 34 sites where soil heat flux measurements were available, which yielded almost identical results (c.f. Fig. B1 and Fig. 4.3). Hence, I conclude that the energy closure (or lack thereof) is not a significant factor in my analysis.

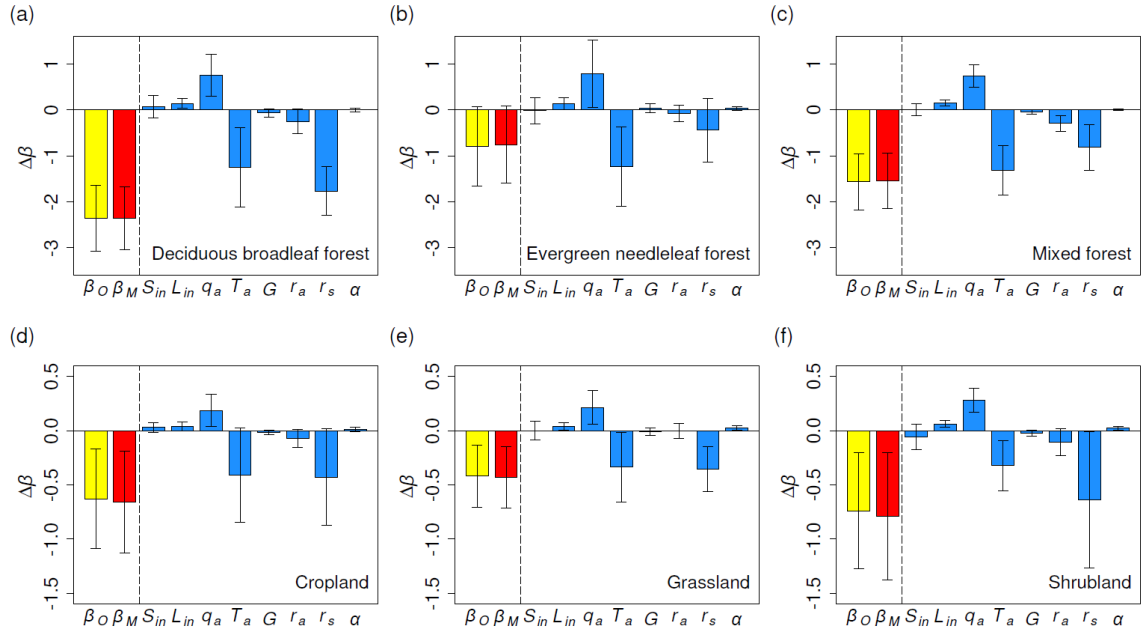


Fig. 4.3. Attribution of the Bowen ratio change after springtime phenology. β_O and β_M are the observed and modeled changes in Bowen ratio, respectively. S_{in} , L_{in} , q_a , T_a , G , r_a , r_s , and α represent contributions from changes in incoming shortwave radiation, incoming longwave radiation, specific humidity, air temperature, ground heat flux, aerodynamic resistance, surface resistance, and albedo, respectively. Different panels present results for different vegetation types. The error bars show one standard deviation from the mean. Note the difference in the scale of the y-axis between panels a-c and panels d-f.

Table 4.3 The 30-days averaged daytime Bowen ratio before and after springtime phenology and their differences for different vegetation types. Values in parentheses indicate one standard deviation.

Vegetation type	Before	After	Difference
Deciduous broadleaf forest	3.20 (0.79)	0.85 (0.27)	-2.35 (0.72)
Evergreen needleleaf forest	2.01 (1.12)	1.22 (0.49)	-0.79 (0.87)
Mixed forest	2.39 (0.71)	0.83 (0.20)	-1.56 (0.61)
Cropland	1.13 (0.62)	0.50 (0.37)	-0.63 (0.46)
Grassland	0.86 (0.44)	0.44 (0.24)	-0.42 (0.29)
Shrubland	1.39 (0.72)	0.65 (0.20)	-0.74 (0.53)

The results presented in this section are consistent with existing theory and results from previous empirical studies (e.g., Moore et al., 1996; Schwartz and Crawford, 2001; Wilson and Baldocchi, 2000), but reveal several interesting features regarding the impact of changing atmospheric conditions on the surface energy balance. For example, changes in specific humidity impose a positive contribution to the Bowen ratio, implying that increases in specific humidity reduce the evaporative fluxes. This is unsurprising because increasing specific humidity arising from increasing evapotranspiration causes the gradient of specific humidity between the land surface and the boundary layer to decrease, thereby imposing a negative feedback on evapotranspiration (Brutsaert, 1982; Heerwaarden et al., 2009; Jarvis and McNaughton, 1986; Monteith and Unsworth, 2013; Santanello et al., 2018). However, the degree to which changes in specific humidity are solely attributable to local processes versus larger-scale weather patterns is unclear.

To address whether changes in near-surface atmospheric properties reflect local boundary layer feedbacks or changes in large-scale forcing, I compared 10-year averaged

annual patterns (from 2001 to 2010) in specific humidity and wind speed at the Morgan-Monroe State Forest flux site against corresponding values at 500 hPa (~5,500m above sea level) across the northeastern United States (i.e., Latitude: 35° ~ 45° ; Longitude: -99° ~ -78°) from the Modern-Era Retrospective analysis for Research and Applications (MERRA) Version 2 data set (Rienecker et al., 2011). As shown in Fig. 4.4, seasonal variation in these variables are quite similar (i.e., low in wintertime and high in summertime for specific humidity, and vice versa for wind speed). Note that I also examined wind patterns based on MERRA data at 850 hPa (not shown) and found similar results. At 500 hPa, atmospheric properties are expected to be unaffected by local-scale surface properties. Hence I assert that the changes in specific humidity and wind speed that I observe in AmeriFlux data are not entirely controlled by local boundary layer feedbacks. Although this type of empirical analysis does not provide a direct attribution of local versus large-scale influences on near-surface atmospheric properties, it strongly implies that changes in atmospheric properties are not exclusively determined locally by changes in surface properties (Fitzjarrald et al., 2001; McNaughton and Spriggs, 1986).

Characterization and quantification of the functional relationship between near-surface atmospheric properties and large-scale forcing by atmospheric processes (i.e., above the boundary layer) are complex and beyond the scope of this study. Doing so empirically would require (at a minimum) vertical profile measurements of potential temperature, specific humidity, and wind speed (van Heerwaarden et al., 2010; Wouters et al., 2019; Zhang et al., 2019), which were not available at the flux tower sites included in this study. Model-based approaches using (for e.g.) convective boundary layer models

have previously been used to link near-surface atmospheric properties with land surface conditions and large-scale atmospheric forcing (e.g., Gentine et al., 2016; Jacobs and De Bruin, 1992; Juang et al., 2007; McNaughton and Spriggs, 1986; van Heerwaarden et al., 2010). The application of these models, combined with observations collected at flux tower sites, have potential to shed further insight into this question but is left for future research.

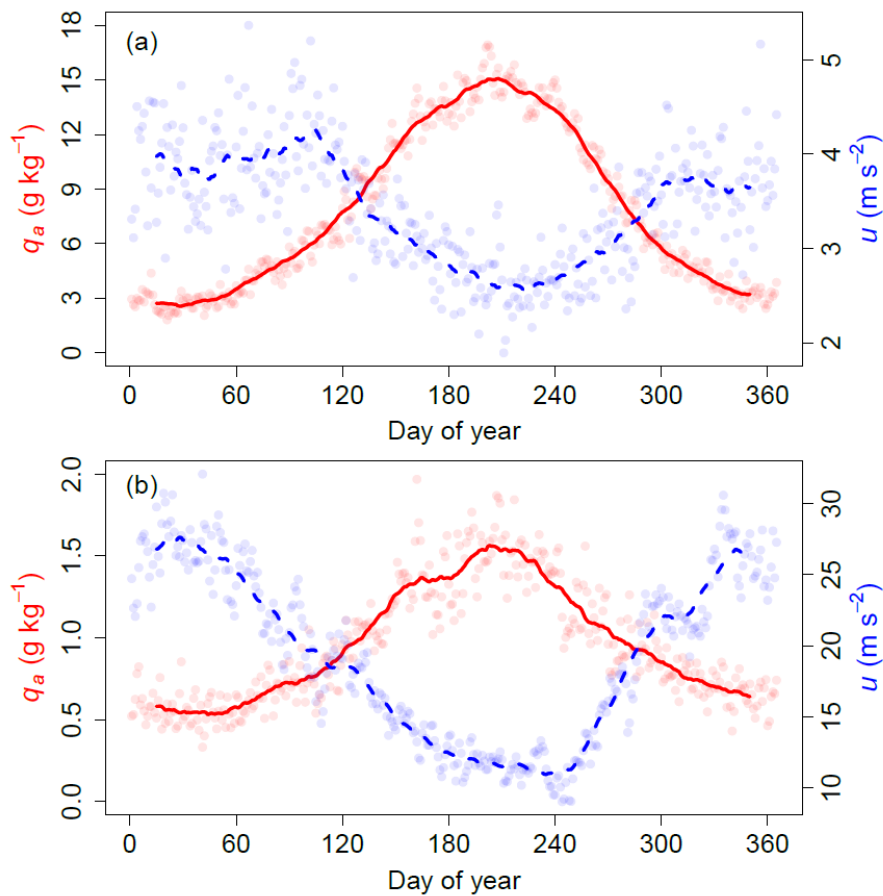


Fig. 4.4. Annual patterns in specific humidity (q_a ; red dots and solid lines) and wind speed (u ; blue dots and dashed lines) at the Morgan-Monroe State Forest site measured from a flux tower (a) and at 500 hPa across the northeastern United States from the MERRA

reanalysis data (b). Dots and lines represent 10-year averaged values (i.e., from 2001 to 2010) and 30-day moving averages, respectively. Note the values are estimated from daytime conditions.

4.3.3. Attribution of increases in aerodynamic resistance: the role of wind speed

An additional important empirical result from my analysis is that aerodynamic resistance increases during springtime across all six vegetation types (Table 4.2). Previous studies have interpreted this change to reflect increases in the surface roughness length, which lowers aerodynamic resistance (e.g., Bonan, 2015; Peñuelas et al., 2009). To illustrate why this is not the case, Fig. 4.5a plots changes in aerodynamic resistance against changes in wind speed across all site-years included in my analysis, and clearly shows that wind speed decreases for almost every site-year and that increases in aerodynamic resistance are negatively correlated with decreases in wind speed. One interpretation of this result is that the emergence of leaves and associated changes in surface three-dimensional structure act to effectively increase surface roughness (via, e.g., increasing the momentum roughness length), leading to lower near-surface wind speeds.

However, this does not appear to be the case. Fig. 4.5b shows results from applying the attribution method described in section 4.2.5 to data from the 10 deciduous broadleaf forest sites included in my analysis. As this figure shows, changes in aerodynamic resistance are mainly attributable to changes in wind speed, with only small contributions from changes in atmospheric stability and roughness length. Further, I find no consistent

pattern of springtime changes in the momentum roughness length across these ten deciduous broadleaf forests sites (Fig. 4.5c), which contradicts traditional models that the momentum roughness length increases after leaf emergence (Peñuelas et al., 2009; Richardson et al., 2013). Conversely, my results are consistent with previous studies demonstrating that the momentum roughness length does not increase monotonically with leaf area index (Blanken and Black, 2004; Garratt, 1992; Parker and Russ, 2004; Sakai et al., 1997; Shaw and Pereira, 1982). When vegetation density is low, increasing leaf area does generally increase the momentum roughness length. In forests, however, where the vegetation density is already high, increasing leaf area index may cause the momentum roughness length to decrease because the vegetation canopy becomes more compact and the surface effectively becomes smoother. In other words, mature canopies can be aerodynamically smoother than their leafless state, depending on the canopy surface rugosity (Blanken and Black, 2004; Parker and Russ, 2004). As a consequence, I conclude that observed increases in aerodynamic resistance after leaf emergence are mainly induced by seasonal decreases in synoptic-scale wind speed (Fig. 4.4) rather than by changes in land surface roughness lengths.

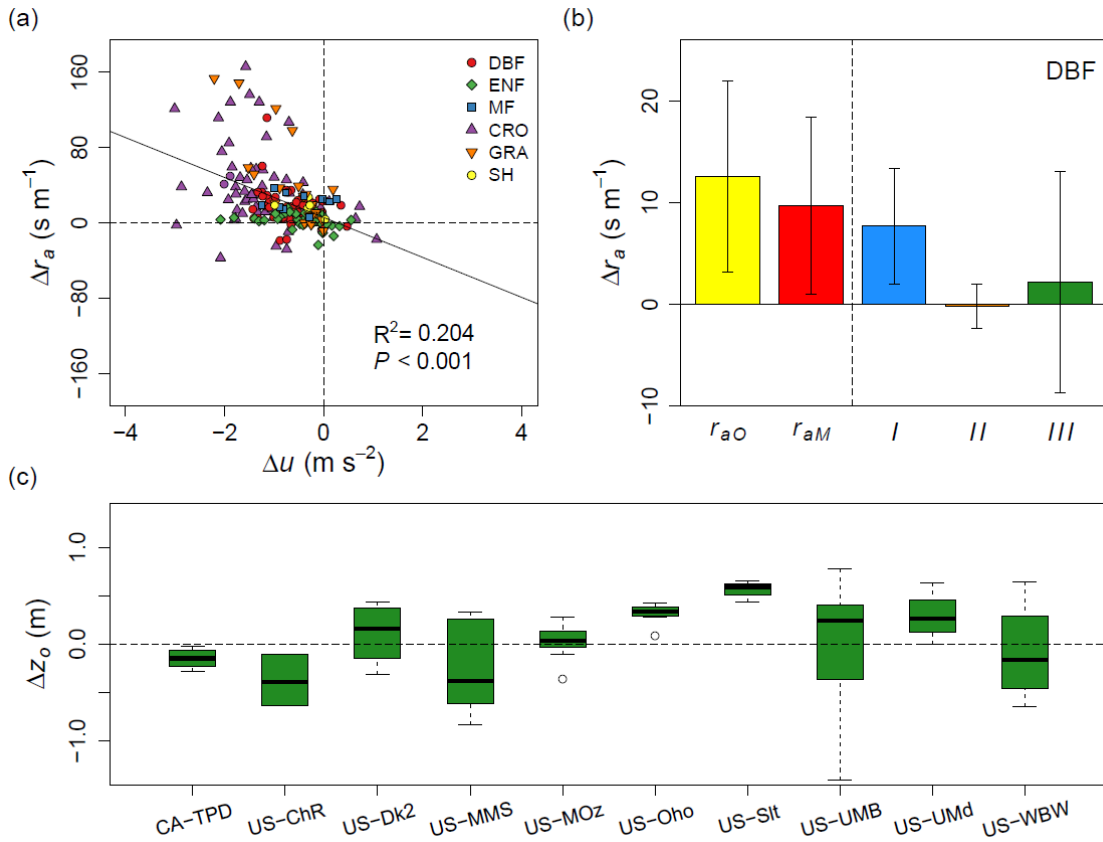


Fig. 4.5. The relationship between changes in wind speed (Δu) and changes in aerodynamic resistance (Δr_a) (a), attribution of changes in aerodynamic resistance (b), and changes in momentum roughness length (Δz_o) (c) at 10 deciduous broadleaf forest sites. Note that the aerodynamic resistance was estimated from sensible heat flux, land surface temperature, and air temperature; hence Δu and Δr_a are quantified independently from each other. In panel (b), r_{aO} and r_{aM} represent the observed and modeled aerodynamic resistance changes, respectively, and I , II , and III represent contributions from changes in wind speed, atmospheric stability including roughness sublayer corrections, and roughness length (see Eq. 4.13); the error bars show one standard deviation from the mean.

4.4. Conclusions

In this chapter, I present a physically-based attribution method, which provides a powerful approach for separating and quantifying the differential impacts of concurrent and interacting changes in surface and atmospheric properties on the surface energy balance, and apply it to data from a large number of sites covering a wide range of climates and vegetation types. The results presented here suggest that changes in surface biophysical properties and energy balance during springtime phenology are strongly coupled with atmospheric processes. Specifically, the springtime decrease in the Bowen ratio, which quantifies energy partitioning into sensible and latent heat fluxes, is the result of interactions among changes in surface conditions and atmospheric properties. While changes in surface resistance and air temperature effectively decrease the Bowen ratio, increases in near-surface specific humidity impose a negative feedback on evaporative fluxes. Further, observed increases in aerodynamic resistance are mainly attributable to reductions in wind speed that are not solely related to changes in surface properties. This study highlights that observed changes in near-surface meteorological properties such as specific humidity and wind speed are not entirely controlled by local processes but seem to strongly follow changes in large-scale atmospheric properties. More broadly, the physically-based method used in this study provides a useful way to unravel the relative importance of different variables on surface energy balance dynamics.

5. CONCLUSIONS

Phenology is a fundamental regulator of many ecological processes, is readily observable and easily understood by the public, and is widely viewed to be an important diagnostic of ecosystem response to climate change. Thus, high-quality long-term records related to phenology, including those derived from satellite remote sensing, are essential. However, despite significant advances derived from both observing and modeling approaches, significant gaps of understanding remain regarding how the phenology of trees responds to variation in environmental conditions and the role of vegetation phenology in land-atmosphere interactions.

To help address these knowledge gaps, this dissertation includes three main research chapters. First, I evaluate land surface phenology products from two remote sensing instruments that are designed to provide long-term continuity of land surface phenology measurements. Second, I use historical remote sensing data in combination with climate data to improve understanding of climate controls on the timing of springtime phenology. Third, I use a physically-based attribution method to quantify the differential impacts of concurrent and interacting changes in surface and atmospheric properties on the surface energy balance, and apply this method to data from a large number of sites covering a wide range of climates and vegetation types.

5.1. Summary of key findings

In chapter 2, I used data from VIIRS and MODIS to evaluate the agreement and characterize the similarities and differences between LSP metrics estimated from each instrument. To do this, I assessed the overall agreement between time series of vegetation indices from VIIRS and MODIS, evaluated the correspondence between retrieved phenometrics from each instrument, and analyzed sources of differences between phenometrics from each product. Results show that EVI2 values from VIIRS and MODIS are similar, but that VIIRS EVI2 time series show more high frequency variation than time series from MODIS. Further, systematic differences between phenometrics from the two products are generally less than one week for most phenometrics across different land cover classes. Comparison of VIIRS and MODIS LSP data with corresponding metrics estimated from Landsat and PhenoCam data consistently showed high agreement among the data sets. Overall, results from this analysis indicate that the VIIRS LSP product provides excellent continuity with the MODIS record.

In chapter 3, I used a model-based analysis to address questions related to how different climate controls affect the timing of springtime phenology. To do this, I developed a state-space Bayesian modeling framework that explicitly includes uncertainty quantification. I applied this model to MODIS land surface phenology data encompassing temperate and boreal deciduous forests of North America for the period 2001 to 2017, using gridded daily meteorological data as forcing. Results show that the model performed well, and demonstrate how each of the three climate variables used in the model (thermal forcing, day-length, and chilling unit) control springtime phenology over the study region.

In the Eastern Temperate Forest ecoregion, which is warmer than the Northern Forest ecoregion included in the study, the preseason period is shorter, which results in higher sensitivity to photoperiod during phenological development. These results suggest that day-length is more important for springtime phenology in Eastern Temperate Forests compared to Northern Forests. More generally, the results from this chapter provide a geographically explicit representation of the relative influence of different controls on springtime phenology in North American deciduous forests, yielding insights regarding how the timing of phenological onset during springtime will change as the climate continues to warm in the coming decades.

In chapter 4, I presented a physically-based attribution method to quantify the relative importance and interactions among surface biophysical and atmospheric variables in modifying the surface energy balance during springtime. The method is applied to data from a large number of sites covering a wide range of climates and vegetation types. Results show that the widely observed decrease in the Bowen ratio that occurs with leaf emergence is not solely attributable to sharp decreases in surface resistance caused by increasing leaf area. Rather, decreases in the Bowen ratio reflect the combined effects of changes in surface properties and atmospheric conditions. Specifically, decreasing surface resistance and increasing air temperature both act to reduce the Bowen ratio, while concurrent increases in specific humidity provide a negative feedback that constrains evaporative fluxes. In parallel, aerodynamic resistance tends to increase after leaf emergence largely because wind speed tends to decrease during springtime. These findings provide a refined characterization of surface energy balance dynamics during springtime

when both surface and atmospheric conditions are changing rapidly and reveal previously understudied properties of the near-surface atmosphere that influence surface Bowen ratio and aerodynamic resistance.

5.2. Future research

5.2.1. Moderate spatial resolution land surface phenology

Long-term records of vegetation phenology observed from satellite observations at coarse spatial resolutions such as those provided by AVHRR and MODIS have greatly contributed to improved understanding of the biological responses to climate change at regional to global scales. However, information at finer spatial resolutions is required for many applications. Landsat provides a more than 30-year record of satellite remote sensing data at moderate spatial resolution (i.e., 30 m). However, the relatively infrequent repeat frequency of Landsat, especially prior to the launch of Landsat 7 in 1999, significantly limits the utility of the Landsat archive in studies of long term changes in LSP. Fortunately, the launch of Sentinel 2A and 2B, in combination with data from Landsat 8, largely resolves this constraint. Therefore, the development of LSP algorithms and products that exploit the high quality 30 m imagery provided by these sensors is now feasible, and creates exciting new opportunities to study landscape-scale patterns and processes related to phenology at regional to continental scales.

5.2.2. Data-driven phenology models with high performance computing systems

The development and usage of process-based phenology models have become essential tools for understanding environmental controls on phenological phenomena and responses to climate variability and change. However, the scientific utility of these models has been questioned because their simplified framework are not sufficiently nuanced to capture interactions and consequences of phenological change processes in the context of a changing climate (Clark et al., 2014b; Hänninen et al., 2019). The explosive growth of data related to ecosystem and climate change processes dictate the need for new approaches and modeling paradigms that not only are able to accommodate and exploit newly available (and very large) data sets, but that also realistically capture the complicated and nuanced nature of phenological responses to environmental forcing and climate change. By exploiting compute power available from cloud-based computing systems in combination with new data sets, data-driven phenological modeling frameworks, such as the state-space based hierarchical Bayesian model used in chapter 3 (or alternatively, deep-learning algorithms from the domain of machine learning), are likely to provide important new insights and modeling approaches that will improve both understanding and our ability to forecast how phenology is expected to change in the coming decades.

5.2.3. Feedbacks between vegetation phenology shifts and biogeochemical cycles

Climate system feedbacks resulting from phenological shifts influence the seasonal course of surface biophysical and atmospheric properties. However, our ability to perform attribution of observed changes in state variables to specific mechanisms or feedback

processes is relatively immature. For example, how carbon, water, and energy budgets will be affected by changes in vegetation phenology arising from climate change at different spatial and temporal scales, and the relative contributions of associated variables to such changes, are not well understood. To resolve this knowledge gap, more work is needed to understand the nature and magnitude of coupling between the atmosphere and terrestrial ecosystems via phenology. In this context, the growing high quality record of long term measurements of phenology (e.g., the MODIS record is now 20 years long), ecosystem processes (e.g., from eddy covariance networks), and weather data, provide the foundation for continued development of improved models and deeper understanding of coupled biosphere-atmosphere interactions.

APPENDIX A

Table A1. Site information of the PhenoCam sites used in the study

Camera name	Latitude (°)	Longitude (°)	Veg.	Full site name
ahwahnee	37.7467	-119.5816	EN	Ahwahnee Meadow, Yosemite National Park, California
arbutuslake	43.9821	-74.2332	DB	Arbutus Lake, Huntington Wildlife Forest, Newcomb, New York
bartlettir	44.0646	-71.2881	DB	Bartlett Experimental Forest, Bartlett, New Hampshire
boundarywaters	47.9467	-91.4955	DB	Boundary Waters Canoe Area Wilderness, Superior National Forest, Minnesota
caryinstitute	41.7839	-73.7341	DB	Cary Institute of Ecosystem Studies, Millbrook, NY
farewellgap	36.4530	-118.5900	EN	Farewell Gap / Mineral King, Sequoia National Park, California
groundhog	48.2174	-82.1555	EN	Groundhog River, Ontario, Canada
harvard	42.5378	-72.1715	DB	EMS Tower, Harvard Forest, Petersham, Massachusetts
harvardbarn	42.5353	-72.1899	EN	Barn Tower, Camera 1, Harvard Forest, Petersham, Massachusetts
harvardlph	42.5420	-72.1850	DB	LPH Tower, Harvard Forest, Petersham, Massachusetts
hubbardbrook	43.9438	-71.7010	DB	Hubbard Brook Experimental Forest, USDA Forest Service Headquarters
hubbardbrooknfw	42.9580	-71.7762	DB	North Facing Watersheds, Hubbard Brook Experimental Forest
hubbardbrooksfw	43.9269	-71.7407	DB	South Facing Watersheds, Hubbard Brook Experimental Forest
ibp	32.5890	-106.8470	GR	Jornada Experimental Range, New Mexico
jasperidge	37.4020	-122.2210	GR	Jasper Ridge Biological Preserve, Woodside, California
laurentides	45.9881	-74.0055	DB	Station de biologie des Laurentides, University of Montreal, Canada
merbleue	45.4094	-75.5187	WL	Mer Bleue Conservation Area, Ottawa, Canada
proctor	44.5250	-72.8660	DB	University of Vermont, Proctor Maple Research Center, Underhill, Vermont
shalehillsczo	40.6500	-77.9000	DB	Susquehanna Shale Hills Critical Zone Observatory (CZO), Pennsylvania
snakerivermn	46.1206	-93.2447	DB	Hay-Snake State Wildlife Management Area, near Woodland, Minnesota
thompsonfarm2N	43.1086	-70.9505	DB	University of New Hampshire, Thompson Farm Observatory, Durham, New Hampshire
tonzi	38.4309	-120.9659	DB	Tonzi Ranch, Amador County, California
turkeypointdbf	42.6353	-80.5576	DB	Mature Deciduous Site, Turkey Point Carbon Cycle Research Project, Ontario, Canada
turkeypointenf02	42.6609	-80.5595	EN	2002 White Pine, Turkey Point Carbon Cycle Research Project, Ontario, Canada
turkeypointenf39	42.7098	-80.3574	EN	1939 White Pine, Turkey Point Carbon Cycle Research Project, Ontario, Canada
turkeypointenf74	42.7068	-80.3483	EN	1974 White Pine, Turkey Point Carbon Cycle Research Project, Ontario, Canada
twitchellalfalfa	38.1154	-121.6467	AG	Twitchell Island, Antioch, California, USA
uiefmaize	40.0628	-88.1961	AG	Maize/Soybean agroecosystem at the University of Illinois Energy Farm
uiefmiscanthus	40.0628	-88.1984	GR	Miscanthus agroecosystem at the University of Illinois Energy Farm
uiefswitchgrass	40.0637	-88.1973	GR	Switchgrass agroecosystem at the University of Illinois Energy Farm
umichbiological	45.5598	-84.7138	DB	University of Michigan Biological Station, near Pellston, Michigan
vaira	38.4133	-120.9506	GR	Vaira Ranch, Amador County, California
willowcreek	45.8060	-90.0791	DB	Willow Creek, Chequamegon-Nicolet National Forest, Wisconsin
woodshole	41.5495	-70.6432	DB	Woods Hole Research Center, Falmouth, Massachusetts

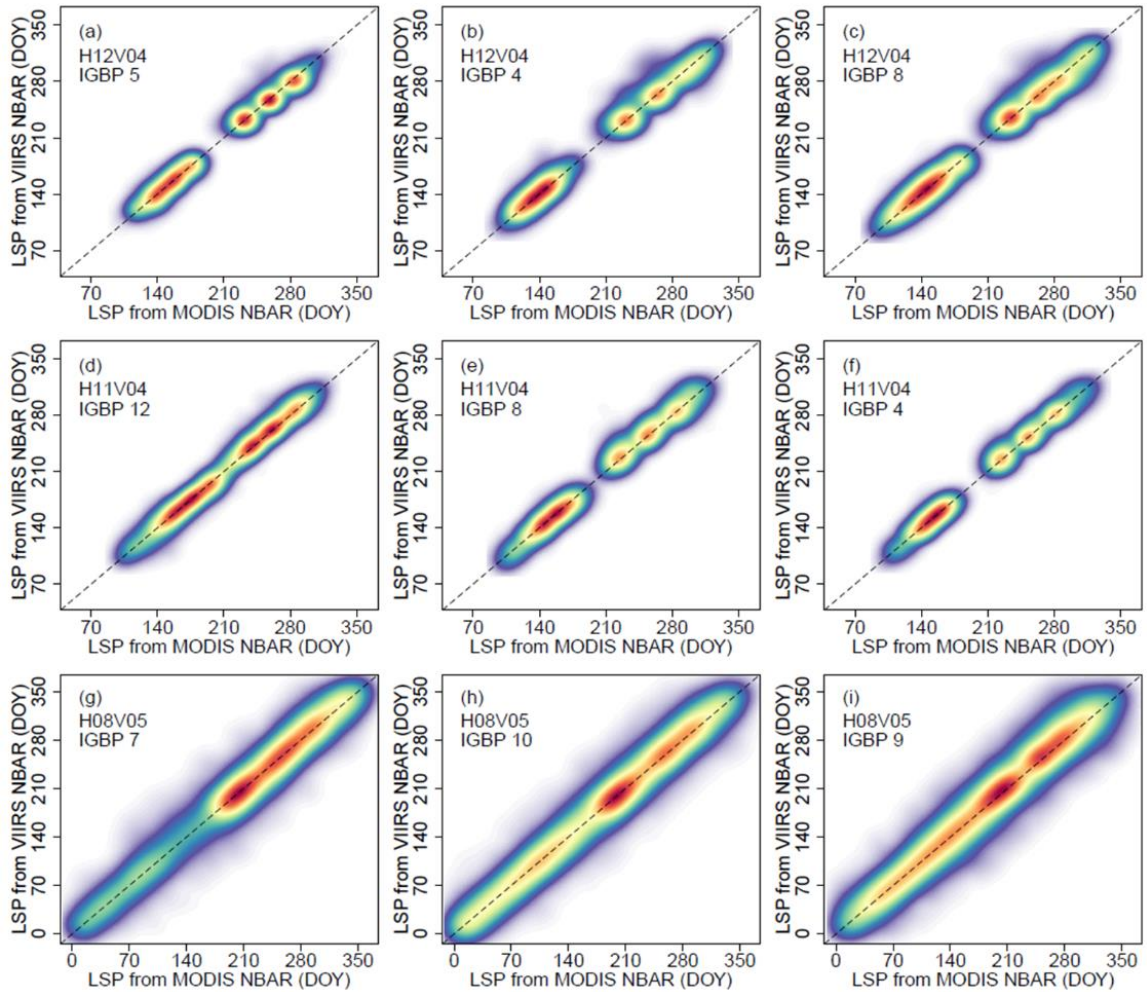


Fig. A1. Comparison of phenometrics retrieved from VIIRS and MODIS NBAR EVI2 time series using the VIIRS LSP algorithm in 2013, stratified by the three most common land cover types in each tile. IGBP land cover was derived from the Collection 6 MODIS Land Cover Type product: 4: deciduous broadleaf forests; 5: mixed forests; 7: open shrublands; 8: woody savannas; 9: savannas; 10: grasslands; 12: croplands. Red indicates high density and light purple indicates low density of observations. The dashed lines show 1:1 agreement.

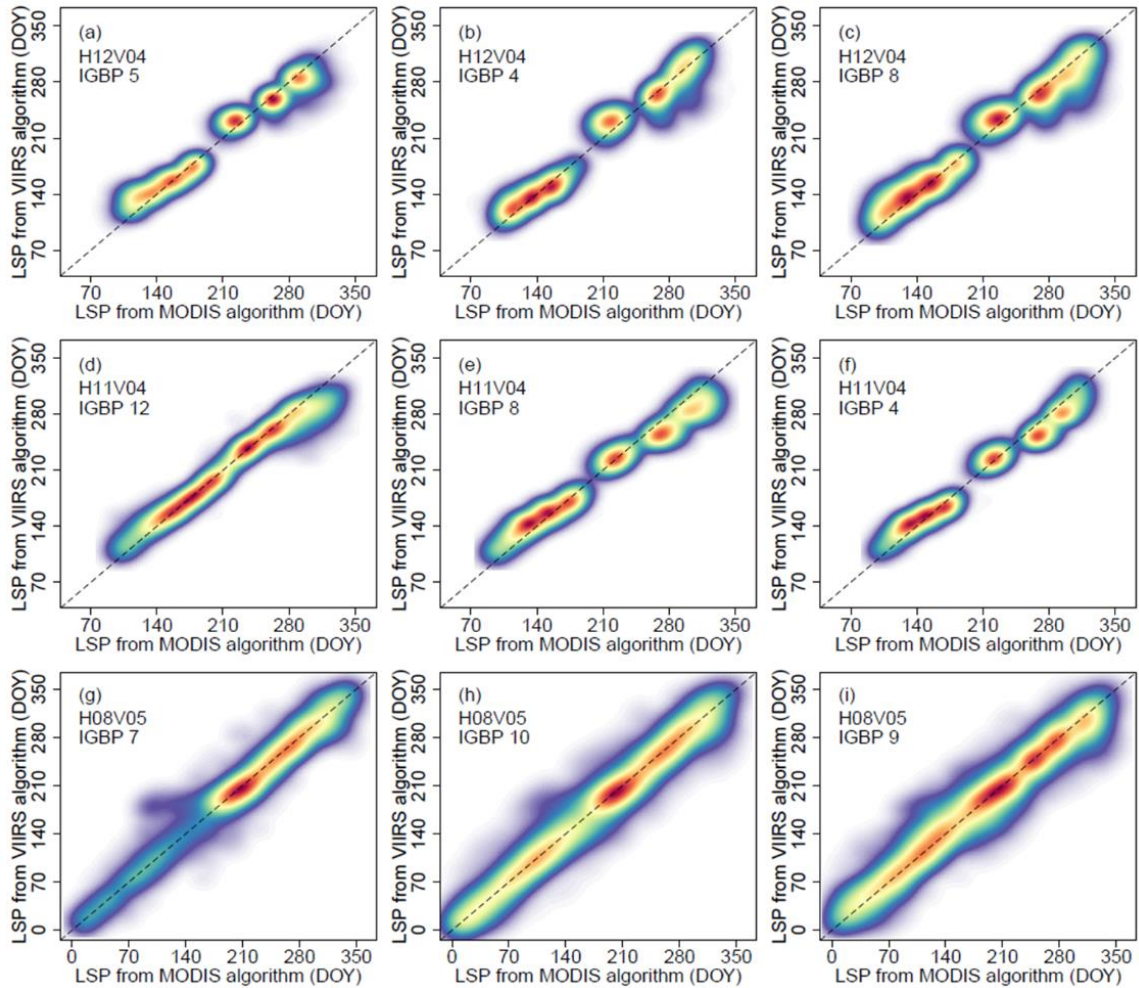


Fig. A2. Comparison of phenometrics retrieved from MODIS NBAR EVI2 time series using the VIIRS LSP and MODIS LCD algorithms in 2013, stratified by the three most common land cover types in each tile. IGBP land cover was derived from the Collection 6 MODIS Collection 6 Land Cover Type product: 4: deciduous broadleaf forests; 5: mixed forests; 7: open shrublands; 8: woody savannas; 9: savannas; 10: grasslands; 12: croplands. Red indicates high density and light purple indicates low density of observations. The dashed lines show 1:1 agreement.

APPENDIX B

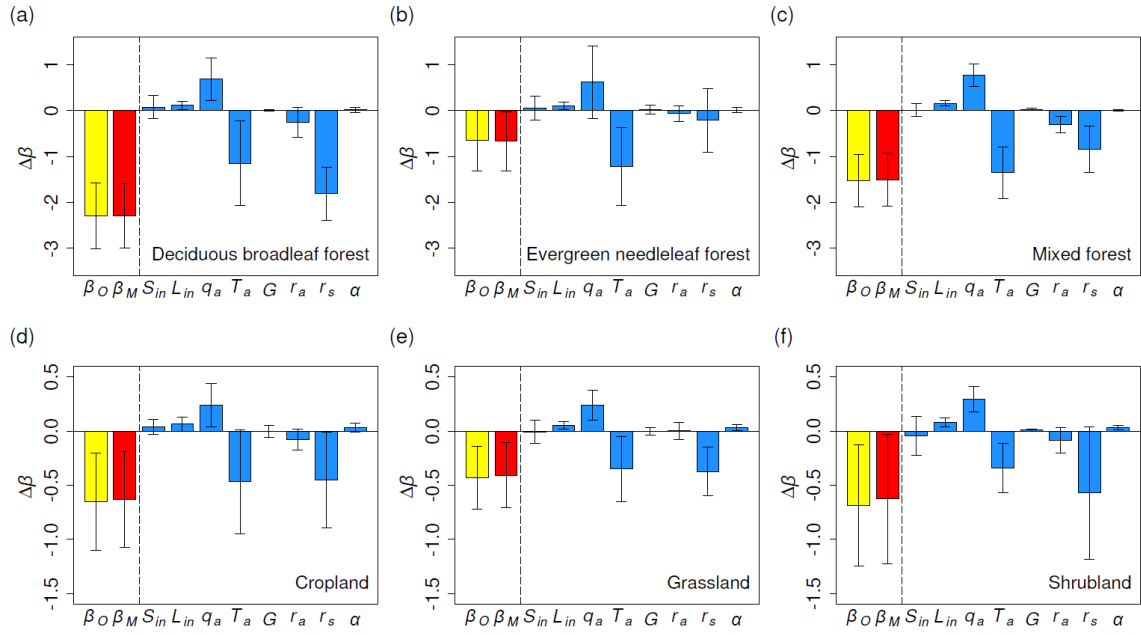


Fig. B1. Same as Fig. 4.3. but the analysis is conducted using measured soil heat fluxes for G , which are only available at 34 out of 42 sites.

BIBLIOGRAPHY

- Abercrombie, S.P., Friedl, M.A., 2016. Improving the Consistency of Multitemporal Land Cover Maps Using a Hidden Markov Model. *IEEE Transactions on Geoscience and Remote Sensing* 54, 703–713. <https://doi.org/10.1109/TGRS.2015.2463689>
- Arnqvist, J., Bergström, H., 2015. Flux-profile relation with roughness sublayer correction. *Quarterly Journal of the Royal Meteorological Society* 141, 1191–1197. <https://doi.org/10.1002/qj.2426>
- Augspurger, C.K., Bartlett, E.A., 2003. Differences in leaf phenology between juvenile and adult trees in a temperate deciduous forest. *Tree Physiology* 23, 517–525. <https://doi.org/10.1093/treephys/23.8.517>
- Baker, J.M., Griffis, T.J., 2005. Examining strategies to improve the carbon balance of corn/soybean agriculture using eddy covariance and mass balance techniques. *Agricultural and Forest Meteorology* 128, 163–177. <https://doi.org/10.1016/j.agrformet.2004.11.005>
- Baldocchi, D., Penuelas, J., n.d. The Physics and Ecology of Mining Carbon Dioxide from the Atmosphere by Ecosystems. *Global Change Biology* 0. <https://doi.org/10.1111/gcb.14559>
- Basler, D., 2016. Evaluating phenological models for the prediction of leaf-out dates in six temperate tree species across central Europe. *Agricultural and Forest Meteorology* 217, 10–21. <https://doi.org/10.1016/j.agrformet.2015.11.007>
- Bernacchi, C.J., Hollinger, S.E., Meyers, T., 2005. The conversion of the corn/soybean ecosystem to no-till agriculture may result in a carbon sink. *Global Change Biology* 11, 1867–1872. <https://doi.org/10.1111/j.1365-2486.2005.01050.x>
- Blanken, P.D., Black, T.A., 2004. The canopy conductance of a boreal aspen forest, Prince Albert National Park, Canada. *Hydrological Processes* 18, 1561–1578. <https://doi.org/10.1002/hyp.1406>
- Bonan, G., 2015. *Ecological Climatology: Concepts and Applications*, 3rd ed. Cambridge University Press.
- Bonan, G.B., 2008. Forests and Climate Change: Forcings, Feedbacks, and the Climate Benefits of Forests. *Science* 320, 1444–1449. <https://doi.org/10.1126/science.1155121>
- Brutsaert, W., 2005. *Hydrology: an introduction*. Cambridge University Press, Cambridge ; New York.
- Brutsaert, W., 1982. *Evaporation into the Atmosphere: Theory, History and Applications*. Springer Science & Business Media.
- Buitenwerf, R., Rose, L., Higgins, S.I., 2015. Three decades of multi-dimensional change in global leaf phenology. *Nature Climate Change* 5, 364–368. <https://doi.org/10.1038/nclimate2533>
- Campagnolo, M.L., Sun, Q., Liu, Y., Schaaf, C., Wang, Z., Román, M.O., 2016. Estimating the effective spatial resolution of the operational BRDF, albedo, and nadir reflectance products from MODIS and VIIRS. *Remote Sensing of Environment* 175, 52–64. <https://doi.org/10.1016/j.rse.2015.12.033>
- Caprio, J.M., 1957. Phenology of Lilac Bloom in Montana. *Science* 126, 1344–1345. <https://doi.org/10.1126/science.126.3287.1344>
- Chen, L., Dirmeyer, P.A., 2016. Adapting observationally based metrics of biogeophysical feedbacks from land cover/land use change to climate modeling. *Environmental Research Letters* 11, 034002. <https://doi.org/10.1088/1748-9326/11/3/034002>
- Chen, M., Melaas, E.K., Gray, J.M., Friedl, M.A., Richardson, A.D., 2016. A new seasonal-deciduous spring phenology submodel in the Community Land Model 4.5: impacts on

- carbon and water cycling under future climate scenarios. *Global Change Biology* 22, 3675–3688. <https://doi.org/10.1111/gcb.13326>
- Chu, H., Baldocchi, D.D., Poindexter, C., Abraha, M., Desai, A.R., Bohrer, G., Arain, M.A., Griffis, T., Blanken, P.D., O'Halloran, T.L., Thomas, R.Q., Zhang, Q., Burns, S.P., Frank, J.M., Christian, D., Brown, S., Black, T.A., Gough, C.M., Law, B.E., Lee, X., Chen, J., Reed, D.E., Massman, W.J., Clark, K., Hatfield, J., Prueger, J., Bracho, R., Baker, J.M., Martin, T.A., 2018. Temporal Dynamics of Aerodynamic Canopy Height Derived From Eddy Covariance Momentum Flux Data Across North American Flux Networks. *Geophysical Research Letters* 45, 9275–9287. <https://doi.org/10.1029/2018GL079306>
- Chu, H., Chen, J., Gottgens, J.F., Desai, A.R., Ouyang, Z., Qian, S.S., 2016. Response and biophysical regulation of carbon dioxide fluxes to climate variability and anomaly in contrasting ecosystems in northwestern Ohio, USA. *Agricultural and Forest Meteorology* 220, 50–68. <https://doi.org/10.1016/j.agrformet.2016.01.008>
- Chuine, I., de Cortazar-Atauri, I.G., Kramer, K., Hänninen, H., 2013. Plant Development Models, in: Schwartz, M.D. (Ed.), *Phenology: An Integrative Environmental Science*. Springer Netherlands, Dordrecht, pp. 275–293. https://doi.org/10.1007/978-94-007-6925-0_15
- Clark, J.S., Gelfand, A.E., Woodall, C.W., Zhu, K., 2014a. More than the sum of the parts: forest climate response from joint species distribution models. *Ecological Applications* 24, 990–999. <https://doi.org/10.1890/13-1015.1>
- Clark, J.S., Salk, C., Melillo, J., Mohan, J., 2014b. Tree phenology responses to winter chilling, spring warming, at north and south range limits. *Functional Ecology* 28, 1344–1355. <https://doi.org/10.1111/1365-2435.12309>
- Clark, K.L., Renninger, H.J., Skowronski, N., Gallagher, M., Schäfer, K.V.R., 2018. Decadal-Scale Reduction in Forest Net Ecosystem Production Following Insect Defoliation Contrasts with Short-Term Impacts of Prescribed Fires. *Forests* 9, 145. <https://doi.org/10.3390/f9030145>
- Dardel, C., Kergoat, L., Hiernaux, P., Mougin, E., Grippa, M., Tucker, C.J., 2014. Re-greening Sahel: 30years of remote sensing data and field observations (Mali, Niger). *Remote Sensing of Environment* 140, 350–364. <https://doi.org/10.1016/j.rse.2013.09.011>
- de Beurs, K.M., Henebry, G.M., 2005. Land surface phenology and temperature variation in the International Geosphere–Biosphere Program high-latitude transects. *Global Change Biology* 11, 779–790. <https://doi.org/10.1111/j.1365-2486.2005.00949.x>
- De Ridder, K., 2010. Bulk Transfer Relations for the Roughness Sublayer. *Boundary-Layer Meteorology* 134, 257–267. <https://doi.org/10.1007/s10546-009-9450-y>
- Devaraju, N., de Noblet-Ducoudré, N., Quesada, B., Bala, G., 2018. Quantifying the Relative Importance of Direct and Indirect Biophysical Effects of Deforestation on Surface Temperature and Teleconnections. *Journal of Climate* 31, 3811–3829. <https://doi.org/10.1175/JCLI-D-17-0563.1>
- Dorman, J.L., Sellers, P.J., 1989. A Global Climatology of Albedo, Roughness Length and Stomatal Resistance for Atmospheric General Circulation Models as Represented by the Simple Biosphere Model (SiB). *Journal of Applied Meteorology* 28, 833–855. [https://doi.org/10.1175/1520-0450\(1989\)028<0833:AGCOAR>2.0.CO;2](https://doi.org/10.1175/1520-0450(1989)028<0833:AGCOAR>2.0.CO;2)
- Easterling, D.R., Meehl, G.A., Parmesan, C., Changnon, S.A., Karl, T.R., Mearns, L.O., 2000. Climate Extremes: Observations, Modeling, and Impacts. *Science* 289, 2068–2074. <https://doi.org/10.1126/science.289.5487.2068>
- Efron, B., 1979. Bootstrap Methods: Another Look at the Jackknife. *Annals of Statistics* 7, 1–26. <https://doi.org/10.1214/aos/1176344552>

- Euskirchen, E.S., Bret-Harte, M.S., Shaver, G.R., Edgar, C.W., Romanovsky, V.E., 2017. Long-Term Release of Carbon Dioxide from Arctic Tundra Ecosystems in Alaska. *Ecosystems* 20, 960–974. <https://doi.org/10.1007/s10021-016-0085-9>
- Fang, J., Piao, S., Tang, Z., Peng, C., Ji, W., 2001. Interannual Variability in Net Primary Production and Precipitation. *Science* 293, 1723–1723. <https://doi.org/10.1126/science.293.5536.1723a>
- Fensholt, R., Proud, S.R., 2012. Evaluation of Earth Observation based global long term vegetation trends — Comparing GIMMS and MODIS global NDVI time series. *Remote Sensing of Environment* 119, 131–147. <https://doi.org/10.1016/j.rse.2011.12.015>
- Fensholt, R., Rasmussen, K., 2011. Analysis of trends in the Sahelian ‘rain-use efficiency’ using GIMMS NDVI, RFE and GPCP rainfall data. *Remote Sensing of Environment* 115, 438–451. <https://doi.org/10.1016/j.rse.2010.09.014>
- Fitzjarrald, D.R., Acevedo, O.C., Moore, K.E., 2001. Climatic Consequences of Leaf Presence in the Eastern United States. *Journal of Climate* 14, 598–614. [https://doi.org/10.1175/1520-0442\(2001\)014<0598:CCOLPI>2.0.CO;2](https://doi.org/10.1175/1520-0442(2001)014<0598:CCOLPI>2.0.CO;2)
- Foken, T., 2008. THE ENERGY BALANCE CLOSURE PROBLEM: AN OVERVIEW. *Ecological Applications* 18, 1351–1367. <https://doi.org/10.1890/06-0922.1>
- Frank, J.M., Massman, W.J., Ewers, B.E., Huckaby, L.S., Negrón, J.F., 2014. Ecosystem CO₂/H₂O fluxes are explained by hydraulically limited gas exchange during tree mortality from spruce bark beetles. *Journal of Geophysical Research: Biogeosciences* 119, 1195–1215. <https://doi.org/10.1002/2013JG002597>
- Friedl, M.A., Gray, J.M., Melaas, E.K., Richardson, A.D., Hufkens, K., Keenan, T.F., Amey Bailey, O’Keefe, J., 2014. A tale of two springs: using recent climate anomalies to characterize the sensitivity of temperate forest phenology to climate change. *Environmental Research Letters* 9, 054006. <https://doi.org/10.1088/1748-9326/9/5/054006>
- Fu, Y.H., Zhao, H., Piao, S., Peaucelle, M., Peng, S., Zhou, G., Ciais, P., Huang, M., Menzel, A., Peñuelas, J., Song, Y., Vitasse, Y., Zeng, Z., Janssens, I.A., 2015. Declining global warming effects on the phenology of spring leaf unfolding. *Nature* 526, 104–107. <https://doi.org/10.1038/nature15402>
- Ganguly, S., Friedl, M.A., Tan, B., Zhang, X., Verma, M., 2010. Land surface phenology from MODIS: Characterization of the Collection 5 global land cover dynamics product. *Remote Sensing of Environment* 114, 1805–1816. <https://doi.org/10.1016/j.rse.2010.04.005>
- Garratt, J.R., 1992. *The atmospheric boundary layer*. Cambridge University Press, New York.
- Gaston, K., Blackburn, T., 2008. *Pattern and Process in Macroecology*. John Wiley & Sons.
- Gauthier, S., Bernier, P., Kuuluvainen, T., Shvidenko, A.Z., Schepaschenko, D.G., 2015. Boreal forest health and global change. *Science* 349, 819–822. <https://doi.org/10.1126/science.aaa9092>
- Gentine, P., Chhang, A., Rigden, A., Salvucci, G., 2016. Evaporation estimates using weather station data and boundary layer theory. *Geophysical Research Letters* 43, 11,661–11,670. <https://doi.org/10.1002/2016GL070819>
- Gilmanov, T.G., Tieszen, L.L., Wylie, B.K., Flanagan, L.B., Frank, A.B., Haferkamp, M.R., Meyers, T.P., Morgan, J.A., 2005. Integration of CO₂ flux and remotely-sensed data for primary production and ecosystem respiration analyses in the Northern Great Plains: potential for quantitative spatial extrapolation. *Global Ecology and Biogeography* 14, 271–292. <https://doi.org/10.1111/j.1466-822X.2005.00151.x>
- Gough, C.M., Hardiman, B.S., Nave, L.E., Bohrer, G., Maurer, K.D., Vogel, C.S., Nadelhoffer, K.J., Curtis, P.S., 2013. Sustained carbon uptake and storage following moderate

- disturbance in a Great Lakes forest. *Ecological Applications* 23, 1202–1215. <https://doi.org/10.1890/12-1554.1>
- Gray, J.M., Melaas, E.K., Sulla-Menashe, D., Moon, M., Friedl, M.A., 2020. Global Land Surface Phenology from MODIS: Collection 6 Products. In Preparation.
- Gu, L., Hanson, P.J., Post, W.M., Kaiser, D.P., Yang, B., Nemani, R., Pallardy, S.G., Meyers, T., 2008. The 2007 Eastern US Spring Freeze: Increased Cold Damage in a Warming World? *BioScience* 58, 253–262. <https://doi.org/10.1641/B580311>
- Guay, K.C., Beck, P.S.A., Berner, L.T., Goetz, S.J., Baccini, A., Buermann, W., 2014. Vegetation productivity patterns at high northern latitudes: a multi-sensor satellite data assessment. *Global Change Biology* 20, 3147–3158. <https://doi.org/10.1111/gcb.12647>
- Güsewell, S., Furrer, R., Gehrig, R., Pietragalla, B., 2017. Changes in temperature sensitivity of spring phenology with recent climate warming in Switzerland are related to shifts of the pre-season. *Global Change Biology* 23, 5189–5202. <https://doi.org/10.1111/gcb.13781>
- Gutman, G.G., 1999. On the use of long-term global data of land reflectances and vegetation indices derived from the advanced very high resolution radiometer. *Journal of Geophysical Research: Atmospheres* 104, 6241–6255. <https://doi.org/10.1029/1998JD200106>
- Hänninen, H., Kramer, K., Tanino, K., Zhang, R., Wu, J., Fu, Y.H., 2019. Experiments Are Necessary in Process-Based Tree Phenology Modelling. *Trends in Plant Science* 24, 199–209. <https://doi.org/10.1016/j.tplants.2018.11.006>
- Hansen, M.C., Potapov, P.V., Moore, R., Hancher, M., Turubanova, S.A., Tyukavina, A., Thau, D., Stehman, S.V., Goetz, S.J., Loveland, T.R., Kommareddy, A., Egorov, A., Chini, L., Justice, C.O., Townshend, J.R.G., 2013. High-Resolution Global Maps of 21st-Century Forest Cover Change. *Science* 342, 850–853. <https://doi.org/10.1126/science.1244693>
- Harman, I.N., Finnigan, J.J., 2007. A simple unified theory for flow in the canopy and roughness sublayer. *Boundary-Layer Meteorology* 123, 339–363. <https://doi.org/10.1007/s10546-006-9145-6>
- Heerwaarden, C.C. van, Arellano, J.V.-G. de, Moene, A.F., Holtslag, A.A.M., 2009. Interactions between dry-air entrainment, surface evaporation and convective boundary-layer development. *Quarterly Journal of the Royal Meteorological Society* 135, 1277–1291. <https://doi.org/10.1002/qj.431>
- Hemes, K.S., Chamberlain, S.D., Eichelmann, E., Anthony, T., Valach, A., Kasak, K., Szutu, D., Verfaillie, J., Silver, W.L., Baldocchi, D.D., 2019. Assessing the carbon and climate benefit of restoring degraded agricultural peat soils to managed wetlands. *Agricultural and Forest Meteorology* 268, 202–214. <https://doi.org/10.1016/j.agrformet.2019.01.017>
- Hiller, R.V., McFadden, J.P., Kljun, N., 2011. Interpreting CO₂ Fluxes Over a Suburban Lawn: The Influence of Traffic Emissions. *Boundary-Layer Meteorology* 138, 215–230. <https://doi.org/10.1007/s10546-010-9558-0>
- Hogg, E.H., Price, D.T., Black, T.A., 2000. Postulated Feedbacks of Deciduous Forest Phenology on Seasonal Climate Patterns in the Western Canadian Interior. *Journal of Climate* 13, 4229–4243. [https://doi.org/10.1175/1520-0442\(2000\)013<4229:PFODFP>2.0.CO;2](https://doi.org/10.1175/1520-0442(2000)013<4229:PFODFP>2.0.CO;2)
- Hollinger, D.Y., Aber, J., Dail, B., Davidson, E.A., Goltz, S.M., Hughes, H., Leclerc, M.Y., Lee, J.T., Richardson, A.D., Rodrigues, C., Scott, N.A., Achuatavariar, D., Walsh, J., 2004. Spatial and temporal variability in forest–atmosphere CO₂ exchange. *Global Change Biology* 10, 1689–1706. <https://doi.org/10.1111/j.1365-2486.2004.00847.x>
- Huete, A.R., 1988. A soil-adjusted vegetation index (SAVI). *Remote Sensing of Environment* 25, 295–309. [https://doi.org/10.1016/0034-4257\(88\)90106-X](https://doi.org/10.1016/0034-4257(88)90106-X)

- Hufkens, K., Friedl, M., Sonnentag, O., Braswell, B.H., Milliman, T., Richardson, A.D., 2012. Linking near-surface and satellite remote sensing measurements of deciduous broadleaf forest phenology. *Remote Sensing of Environment, Remote Sensing of Urban Environments* 117, 307–321. <https://doi.org/10.1016/j.rse.2011.10.006>
- Jacobs, C.M.J., De Bruin, H. a. R., 1992. The Sensitivity of Regional Transpiration to Land-Surface Characteristics: Significance of Feedback. *Journal of Climate* 5, 683–698. [https://doi.org/10.1175/1520-0442\(1992\)005<0683:TSORTT>2.0.CO;2](https://doi.org/10.1175/1520-0442(1992)005<0683:TSORTT>2.0.CO;2)
- Jarvis, P.G., McNaughton, K.G., 1986. Stomatal Control of Transpiration: Scaling Up from Leaf to Region, in: MacFadyen, A., Ford, E.D. (Eds.), *Advances in Ecological Research*. Academic Press, pp. 1–49. [https://doi.org/10.1016/S0065-2504\(08\)60119-1](https://doi.org/10.1016/S0065-2504(08)60119-1)
- Jarvis, P.G., Monteith, J.L., Weatherley, P.E., 1976. The interpretation of the variations in leaf water potential and stomatal conductance found in canopies in the field. *Philosophical Transactions of the Royal Society of London. B, Biological Sciences* 273, 593–610. <https://doi.org/10.1098/rstb.1976.0035>
- Jiang, Z., Huete, A.R., Didan, K., Miura, T., 2008. Development of a two-band enhanced vegetation index without a blue band. *Remote Sensing of Environment* 112, 3833–3845. <https://doi.org/10.1016/j.rse.2008.06.006>
- Jones, M.O., Kimball, J.S., Nemani, R.R., 2014. Asynchronous Amazon forest canopy phenology indicates adaptation to both water and light availability. *Environmental Research Letters* 9, 124021. <https://doi.org/10.1088/1748-9326/9/12/124021>
- Ju, J., Masek, J.G., 2016a. The vegetation greenness trend in Canada and US Alaska from 1984–2012 Landsat data. *Remote Sensing of Environment* 176, 1–16. <https://doi.org/10.1016/j.rse.2016.01.001>
- Ju, J., Masek, J.G., 2016b. The vegetation greenness trend in Canada and US Alaska from 1984–2012 Landsat data. *Remote Sensing of Environment* 176, 1–16. <https://doi.org/10.1016/j.rse.2016.01.001>
- Juang, J.-Y., Katul, G.G., Porporato, A., Stoy, P.C., Siqueira, M.S., Detto, M., Kim, H.-S., Oren, R., 2007. Eco-hydrological controls on summertime convective rainfall triggers. *Global Change Biology* 13, 887–896. <https://doi.org/10.1111/j.1365-2486.2007.01315.x>
- Justice, C.O., Román, M.O., Csiszar, I., Vermote, E.F., Wolfe, R.E., Hook, S.J., Friedl, M., Wang, Z., Schaaf, C.B., Miura, T., Tschudi, M., Riggs, G., Hall, D.K., Lyapustin, A.I., Devadiga, S., Davidson, C., Masuoka, E.J., 2013. Land and cryosphere products from Suomi NPP VIIRS: Overview and status. *Journal of Geophysical Research: Atmospheres* 118, 9753–9765. <https://doi.org/10.1002/jgrd.50771>
- Keenan, T.F., Gray, J., Friedl, M.A., Toomey, M., Bohrer, G., Hollinger, D.Y., Munger, J.W., O’Keefe, J., Schmid, H.P., Wing, I.S., Yang, B., Richardson, A.D., 2014. Net carbon uptake has increased through warming-induced changes in temperate forest phenology. *Nature Climate Change* 4, 598–604. <https://doi.org/10.1038/nclimate2253>
- Keenan, T.F., Riley, W.J., 2018. Greening of the land surface in the world’s cold regions consistent with recent warming. *Nature Climate Change* 1. <https://doi.org/10.1038/s41558-018-0258-y>
- Klosterman, S.T., Hufkens, K., Gray, J.M., Melaas, E., Sonnentag, O., Lavine, I., Mitchell, L., Norman, R., Friedl, M.A., Richardson, A.D., 2014. Evaluating remote sensing of deciduous forest phenology at multiple spatial scales using PhenoCam imagery. *Biogeosciences* 11, 4305–4320. <https://doi.org/10.5194/bg-11-4305-2014>
- Körner, C., Basler, D., 2010. Phenology Under Global Warming. *Science* 327, 1461–1462. <https://doi.org/10.1126/science.1186473>

- Kramer, K., 1994. Selecting a Model to Predict the Onset of Growth of *Fagus sylvatica*. *Journal of Applied Ecology* 31, 172–181. <https://doi.org/10.2307/2404609>
- Kwon, H., Law, B.E., Thomas, C.K., Johnson, B.G., 2018. The influence of hydrological variability on inherent water use efficiency in forests of contrasting composition, age, and precipitation regimes in the Pacific Northwest. *Agricultural and Forest Meteorology* 249, 488–500. <https://doi.org/10.1016/j.agrformet.2017.08.006>
- Laube, J., Sparks, T.H., Estrella, N., Höfler, J., Ankerst, D.P., Menzel, A., 2014. Chilling outweighs photoperiod in preventing precocious spring development. *Global Change Biology* 20, 170–182. <https://doi.org/10.1111/gcb.12360>
- Lee, X., Goulden, M.L., Hollinger, D.Y., Barr, A., Black, T.A., Bohrer, G., Bracho, R., Drake, B., Goldstein, A., Gu, L., Katul, G., Kolb, T., Law, B.E., Margolis, H., Meyers, T., Monson, R., Munger, W., Oren, R., U, K.T.P., Richardson, A.D., Schmid, H.P., Staebler, R., Wofsy, S., Zhao, L., 2011. Observed increase in local cooling effect of deforestation at higher latitudes. *Nature* 479, 384–387. <https://doi.org/10.1038/nature10588>
- Li, D., Liao, W., Rigden, A.J., Liu, X., Wang, D., Malyshev, S., Shevliakova, E., 2019. Urban heat island: Aerodynamics or imperviousness? *Science Advances* 5, eaau4299. <https://doi.org/10.1126/sciadv.aau4299>
- Li, D., Wang, L., 2019. Sensitivity of Surface Temperature to Land Use and Land Cover Change-Induced Biophysical Changes: The Scale Issue. *Geophysical Research Letters* 46, 9678–9689. <https://doi.org/10.1029/2019GL084861>
- Liang, L., Schwartz, M.D., Fei, S., 2011. Validating satellite phenology through intensive ground observation and landscape scaling in a mixed seasonal forest. *Remote Sensing of Environment* 115, 143–157. <https://doi.org/10.1016/j.rse.2010.08.013>
- Liao, W., Rigden, A.J., Li, D., 2018. Attribution of Local Temperature Response to Deforestation. *Journal of Geophysical Research: Biogeosciences*. <https://doi.org/10.1029/2018JG004401>
- Liebig, J.F. von, Playfair, L.P.B., Webster, J.W., 1841. *Organic Chemistry in Its Applications to Agriculture and Physiology*. J. Owen.
- Liu, Q., Fu, Y.H., Liu, Y., Janssens, I.A., Piao, S., 2017. Simulating the onset of spring vegetation growth across the Northern Hemisphere. *Global Change Biology* 24, 1342–1356. <https://doi.org/10.1111/gcb.13954>
- Liu, Y., Wang, Z., Sun, Q., Erb, A.M., Li, Z., Schaaf, C.B., Zhang, X., Román, M.O., Scott, R.L., Zhang, Q., Novick, K.A., Syndonia Bret-Harte, M., Petroy, S., SanClements, M., 2017. Evaluation of the VIIRS BRDF, Albedo and NBAR products suite and an assessment of continuity with the long term MODIS record. *Remote Sensing of Environment* 201, 256–274. <https://doi.org/10.1016/j.rse.2017.09.020>
- Luyssaert, S., Jammert, M., Stoy, P.C., Estel, S., Pongratz, J., Ceschia, E., Churkina, G., Don, A., Erb, K., Ferlicoq, M., Gielen, B., Grünwald, T., Houghton, R.A., Klumpp, K., Knohl, A., Kolb, T., Kuemmerle, T., Laurila, T., Lohila, A., Loustau, D., McGrath, M.J., Meyfroidt, P., Moors, E.J., Naudts, K., Novick, K., Otto, J., Pilegaard, K., Pio, C.A., Rambal, S., Rebmann, C., Ryder, J., Suyker, A.E., Varlagin, A., Wattenbach, M., Dolman, A.J., 2014. Land management and land-cover change have impacts of similar magnitude on surface temperature. *Nature Climate Change* 4, 389–393. <https://doi.org/10.1038/nclimate2196>
- McCaughey, J.H., Pejam, M.R., Arain, M.A., Cameron, D.A., 2006. Carbon dioxide and energy fluxes from a boreal mixedwood forest ecosystem in Ontario, Canada. *Agricultural and Forest Meteorology, The Fluxnet-Canada Research Network: Influence of Climate and Disturbance on Carbon Cycling in Forests and Peatlands* 140, 79–96. <https://doi.org/10.1016/j.agrformet.2006.08.010>

- McNaughton, K.G., Spriggs, T.W., 1986. A mixed-layer model for regional evaporation. *Boundary-Layer Meteorology* 34, 243–262. <https://doi.org/10.1007/BF00122381>
- Melaas, E.K., Friedl, M.A., Richardson, A.D., 2016a. Multiscale modeling of spring phenology across Deciduous Forests in the Eastern United States. *Global Change Biology* 22, 792–805. <https://doi.org/10.1111/gcb.13122>
- Melaas, E.K., Friedl, M.A., Zhu, Z., 2013a. Detecting interannual variation in deciduous broadleaf forest phenology using Landsat TM/ETM+ data. *Remote Sensing of Environment* 132, 176–185. <https://doi.org/10.1016/j.rse.2013.01.011>
- Melaas, E.K., Richardson, A.D., Friedl, M.A., Dragoni, D., Gough, C.M., Herbst, M., Montagnani, L., Moors, E., 2013b. Using FLUXNET data to improve models of springtime vegetation activity onset in forest ecosystems. *Agricultural and Forest Meteorology* 171–172, 46–56. <https://doi.org/10.1016/j.agrformet.2012.11.018>
- Melaas, E.K., Sulla-Menashe, D., Friedl, M.A., 2018. Multidecadal Changes and Interannual Variation in Springtime Phenology of North American Temperate and Boreal Deciduous Forests. *Geophysical Research Letters* 45, 2679–2687. <https://doi.org/10.1002/2017GL076933>
- Melaas, E.K., Sulla-Menashe, D., Gray, J.M., Black, T.A., Morin, T.H., Richardson, A.D., Friedl, M.A., 2016b. Multisite analysis of land surface phenology in North American temperate and boreal deciduous forests from Landsat. *Remote Sensing of Environment* 186, 452–464. <https://doi.org/10.1016/j.rse.2016.09.014>
- Menzel, A., Sparks, T.H., Estrella, N., Koch, E., Aasa, A., Ahas, R., Alm-Kübler, K., Bissolli, P., Braslavská, O., Briede, A., Chmielewski, F.M., Crepinsek, Z., Curnel, Y., Dahl, Å., Defila, C., Donnelly, A., Filella, Y., Jatzcak, K., Måge, F., Mestre, A., Nordli, Ø., Peñuelas, J., Pirinen, P., Remišová, V., Scheifinger, H., Striz, M., Susnik, A., Vliet, A.J.H.V., Wielgolaski, F.-E., Zach, S., Zust, A., 2006. European phenological response to climate change matches the warming pattern. *Global Change Biology* 12, 1969–1976. <https://doi.org/10.1111/j.1365-2486.2006.01193.x>
- Meyers, T.P., Hollinger, S.E., 2004. An assessment of storage terms in the surface energy balance of maize and soybean. *Agricultural and Forest Meteorology* 125, 105–115. <https://doi.org/10.1016/j.agrformet.2004.03.001>
- Monteith, J.L., Unsworth, M.H., 2013. *Principles of environmental physics: plants, animals, and the atmosphere*, 4th ed. ed. Elsevier/Academic Press, Amsterdam ; Boston.
- Moon, M., Li, D., Liao, W., Rigden, A.J., Friedl, M.A., 2020. Modification of surface energy balance during springtime: The relative importance of biophysical and meteorological changes. *Agricultural and Forest Meteorology* 284, 107905. <https://doi.org/10.1016/j.agrformet.2020.107905>
- Moon, M., Zhang, X., Henebry, G.M., Liu, L., Gray, J.M., Melaas, E.K., Friedl, M.A., 2019. Long-term continuity in land surface phenology measurements: A comparative assessment of the MODIS land cover dynamics and VIIRS land surface phenology products. *Remote Sensing of Environment* 226, 74–92. <https://doi.org/10.1016/j.rse.2019.03.034>
- Moore, K.E., Fitzjarrald, D.R., Sakai, R.K., Goulden, M.L., Munger, J.W., Wofsy, S.C., 1996a. Seasonal Variation in Radiative and Turbulent Exchange at a Deciduous Forest in Central Massachusetts. *Journal of Applied Meteorology* 35, 122–134. [https://doi.org/10.1175/1520-0450\(1996\)035<0122:SVIRAT>2.0.CO;2](https://doi.org/10.1175/1520-0450(1996)035<0122:SVIRAT>2.0.CO;2)
- Moore, K.E., Fitzjarrald, D.R., Sakai, R.K., Goulden, M.L., Munger, J.W., Wofsy, S.C., 1996b. Seasonal Variation in Radiative and Turbulent Exchange at a Deciduous Forest in Central

- Massachusetts. *Journal of Applied Meteorology* 35, 122–134. [https://doi.org/10.1175/1520-0450\(1996\)035<0122:SVIRAT>2.0.CO;2](https://doi.org/10.1175/1520-0450(1996)035<0122:SVIRAT>2.0.CO;2)
- Morin, X., Lechowicz, M.J., Augspurger, C., O’keefe, J., Viner, D., Chuine, I., 2009. Leaf phenology in 22 North American tree species during the 21st century. *Global Change Biology* 15, 961–975. <https://doi.org/10.1111/j.1365-2486.2008.01735.x>
- Myneni, R.B., Keeling, C.D., Tucker, C.J., Asrar, G., Nemani, R.R., 1997. Increased plant growth in the northern high latitudes from 1981 to 1991. *Nature* 386, 698–702. <https://doi.org/10.1038/386698a0>
- Nagol, J.R., Vermote, E.F., Prince, S.D., 2009. Effects of atmospheric variation on AVHRR NDVI data. *Remote Sensing of Environment* 113, 392–397. <https://doi.org/10.1016/j.rse.2008.10.007>
- Noormets, A., Gavazzi, M.J., McNulty, S.G., Domec, J.-C., Sun, G., King, J.S., Chen, J., 2010. Response of carbon fluxes to drought in a coastal plain loblolly pine forest. *Global Change Biology* 16, 272–287. <https://doi.org/10.1111/j.1365-2486.2009.01928.x>
- Noormets, A., McNulty, S.G., Domec, J.-C., Gavazzi, M., Sun, G., King, J.S., 2012. The role of harvest residue in rotation cycle carbon balance in loblolly pine plantations. Respiration partitioning approach. *Global Change Biology* 18, 3186–3201. <https://doi.org/10.1111/j.1365-2486.2012.02776.x>
- Oishi, A.C., Oren, R., Stoy, P.C., 2008. Estimating components of forest evapotranspiration: A footprint approach for scaling sap flux measurements. *Agricultural and Forest Meteorology* 148, 1719–1732. <https://doi.org/10.1016/j.agrformet.2008.06.013>
- Ollinger, S.V., Richardson, A.D., Martin, M.E., Hollinger, D.Y., Frohling, S.E., Reich, P.B., Plourde, L.C., Katul, G.G., Munger, J.W., Oren, R., Smith, M.-L., U, K.T.P., Bolstad, P.V., Cook, B.D., Day, M.C., Martin, T.A., Monson, R.K., Schmid, H.P., 2008. Canopy nitrogen, carbon assimilation, and albedo in temperate and boreal forests: Functional relations and potential climate feedbacks. *Proceedings of the National Academy of Sciences USA* 105, 19336–19341. <https://doi.org/10.1073/pnas.0810021105>
- Omernik, J.M., 1987. Ecoregions of the Conterminous United States. *Annals of the Association of American Geographers* 77, 118–125. <https://doi.org/10.1111/j.1467-8306.1987.tb00149.x>
- Omernik, J.M., Griffith, G.E., 2014. Ecoregions of the Conterminous United States: Evolution of a Hierarchical Spatial Framework. *Environmental Management* 54, 1249–1266. <https://doi.org/10.1007/s00267-014-0364-1>
- Oren, R., Hsieh, C.-I., Stoy, P., Albertson, J., McCarthy, H.R., Harrell, P., Katul, G.G., 2006. Estimating the uncertainty in annual net ecosystem carbon exchange: spatial variation in turbulent fluxes and sampling errors in eddy-covariance measurements. *Global Change Biology* 12, 883–896. <https://doi.org/10.1111/j.1365-2486.2006.01131.x>
- Park, T., Chen, C., Macias-Fauria, M., Tømmervik, H., Choi, S., Winkler, A., Bhatt, U.S., Walker, D.A., Piao, S., Brovkin, V., Nemani, R.R., Myneni, R.B., 2019. Changes in timing of seasonal peak photosynthetic activity in northern ecosystems. *Global Change Biology*. gcb.14638. <https://doi.org/10.1111/gcb.14638>
- Park, T., Ganguly, S., Tømmervik, H., Euskirchen, E.S., Høgda, K.-A., Karlsen, S.R., Brovkin, V., Nemani, R.R., Myneni, R.B., 2016. Changes in growing season duration and productivity of northern vegetation inferred from long-term remote sensing data. *Environmental Research Letters* 11, 084001. <https://doi.org/10.1088/1748-9326/11/8/084001>
- Parker, G.G., Russ, M.E., 2004. The canopy surface and stand development: assessing forest canopy structure and complexity with near-surface altimetry. *Forest Ecology and Management* 189, 307–315. <https://doi.org/10.1016/j.foreco.2003.09.001>

- Peichl, M., Arain, M.A., Brodeur, J.J., 2010. Age effects on carbon fluxes in temperate pine forests. *Agricultural and Forest Meteorology* 150, 1090–1101. <https://doi.org/10.1016/j.agrformet.2010.04.008>
- Peñuelas, J., Rutishauser, T., Filella, I., 2009. Phenology Feedbacks on Climate Change. *Science* 324, 887–888. <https://doi.org/10.1126/science.1173004>
- Piao, S., Ciais, P., Friedlingstein, P., Peylin, P., Reichstein, M., Luysaert, S., Margolis, H., Fang, J., Barr, A., Chen, A., Grelle, A., Hollinger, D.Y., Laurila, T., Lindroth, A., Richardson, A.D., Vesala, T., 2008. Net carbon dioxide losses of northern ecosystems in response to autumn warming. *Nature* 451, 49–52. <https://doi.org/10.1038/nature06444>
- Piao, S., Liu, Z., Wang, T., Peng, S., Ciais, P., Huang, M., Ahlstrom, A., Burkhardt, J.F., Chevallier, F., Janssens, I.A., Jeong, S.-J., Lin, X., Mao, J., Miller, J., Mohammat, A., Myneni, R.B., Peñuelas, J., Shi, X., Stohl, A., Yao, Y., Zhu, Z., Tans, P.P., 2017. Weakening temperature control on the interannual variations of spring carbon uptake across northern lands. *Nature Climate Change* 7, 359–363. <https://doi.org/10.1038/nclimate3277>
- Pielke, R.A., Sr, Avissar, R., Raupach, M., Dolman, A.J., Zeng, X., Denning, A.S., 1998. Interactions between the atmosphere and terrestrial ecosystems: influence on weather and climate. *Global Change Biology* 4, 461–475. <https://doi.org/10.1046/j.1365-2486.1998.t01-1-00176.x>
- Reed, B.C., Brown, J.F., VanderZee, D., Loveland, T.R., Merchant, J.W., Ohlen, D.O., 1994. Measuring phenological variability from satellite imagery. *Journal of Vegetation Science* 5, 703–714. <https://doi.org/10.2307/3235884>
- Richardson, A.D., Black, T.A., Ciais, P., Delbart, N., Friedl, M.A., Gobron, N., Hollinger, D.Y., Kutsch, W.L., Longdoz, B., Luysaert, S., Migliavacca, M., Montagnani, L., Munger, J.W., Moors, E., Piao, S., Rebmann, C., Reichstein, M., Saigusa, N., Tomelleri, E., Vargas, R., Varlagin, A., 2010. Influence of spring and autumn phenological transitions on forest ecosystem productivity. *Philosophical Transactions of the Royal Society of London B: Biological Sciences* 365, 3227–3246. <https://doi.org/10.1098/rstb.2010.0102>
- Richardson, A.D., Hollinger, D.Y., Dail, D.B., Lee, J.T., Munger, J.W., O’keefe, J., 2009. Influence of spring phenology on seasonal and annual carbon balance in two contrasting New England forests. *Tree Physiol* 29, 321–331. <https://doi.org/10.1093/treephys/tpn040>
- Richardson, A.D., Hufkens, K., Milliman, T., Aubrecht, D.M., Chen, M., Gray, J.M., Johnston, M.R., Keenan, T.F., Klosterman, S.T., Kosmala, M., Melaas, E.K., Friedl, M.A., Frolking, S., 2018a. Tracking vegetation phenology across diverse North American biomes using PhenoCam imagery. *Scientific Data* 5, 180028. <https://doi.org/10.1038/sdata.2018.28>
- Richardson, A.D., Hufkens, K., Milliman, T., Aubrecht, D.M., Furze, M.E., Seyednasrollah, B., Krassovski, M.B., Latimer, J.M., Nettles, W.R., Heiderman, R.R., Warren, J.M., Hanson, P.J., 2018b. Ecosystem warming extends vegetation activity but heightens vulnerability to cold temperatures. *Nature*. <https://doi.org/10.1038/s41586-018-0399-1>
- Richardson, A.D., Hufkens, K., Milliman, T., Frolking, S., 2018c. Intercomparison of phenological transition dates derived from the PhenoCam Dataset V1.0 and MODIS satellite remote sensing. *Scientific Reports* 8, 5679. <https://doi.org/10.1038/s41598-018-23804-6>
- Richardson, A.D., Keenan, T.F., Migliavacca, M., Ryu, Y., Sonnentag, O., Toomey, M., 2013. Climate change, phenology, and phenological control of vegetation feedbacks to the climate system. *Agricultural and Forest Meteorology* 169, 156–173. <https://doi.org/10.1016/j.agrformet.2012.09.012>

- Rienecker, M.M., Suarez, M.J., Gelaro, R., Todling, R., Bacmeister, J., Liu, E., Bosilovich, M.G., Schubert, S.D., Takacs, L., Kim, G.-K., Bloom, S., Chen, J., Collins, D., Conaty, A., da Silva, A., Gu, W., Joiner, J., Koster, R.D., Lucchesi, R., Molod, A., Owens, T., Pawson, S., Pegion, P., Redder, C.R., Reichle, R., Robertson, F.R., Ruddick, A.G., Sienkiewicz, M., Woollen, J., 2011. MERRA: NASA's Modern-Era Retrospective Analysis for Research and Applications. *J. Climate* 24, 3624–3648. <https://doi.org/10.1175/JCLI-D-11-00015.1>
- Rigden, A., Li, D., Salvucci, G., 2018. Dependence of thermal roughness length on friction velocity across land cover types: A synthesis analysis using AmeriFlux data. *Agricultural and Forest Meteorology* 249, 512–519. <https://doi.org/10.1016/j.agrformet.2017.06.003>
- Rigden, A.J., Li, D., 2017. Attribution of surface temperature anomalies induced by land use and land cover changes. *Geophysical Research Letters* 44, 6814–6822. <https://doi.org/10.1002/2017GL073811>
- Runkle, B.R.K., Rigby, J.R., Reba, M.L., Anapalli, S.S., Bhattacharjee, J., Krauss, K.W., Liang, L., Locke, M.A., Novick, K.A., Sui, R., Suvočarev, K., White, P.M., 2017. Delta-Flux: An Eddy Covariance Network for a Climate-Smart Lower Mississippi Basin. *Agricultural & Environmental Letters* 2. <https://doi.org/10.2134/ael2017.01.0003>
- Ryu, Y., Baldocchi, D.D., Ma, S., Hehn, T., 2008. Interannual variability of evapotranspiration and energy exchange over an annual grassland in California. *Journal of Geophysical Research: Atmospheres* 113. <https://doi.org/10.1029/2007JD009263>
- Saikkonen, K., Taulavuori, K., Hyvönen, T., Gundel, P.E., Hamilton, C.E., Vänninen, I., Nissinen, A., Helander, M., 2012. Climate change-driven species' range shifts filtered by photoperiodism. *Nature Climate Change* 2, 239–242. <https://doi.org/10.1038/nclimate1430>
- Sakai, R.K., Fitzjarrald, D.R., Moore, K.E., 1997. Detecting leaf area and surface resistance during transition seasons. *Agricultural and Forest Meteorology* 84, 273–284. [https://doi.org/10.1016/S0168-1923\(96\)02359-3](https://doi.org/10.1016/S0168-1923(96)02359-3)
- Sakamoto, T., Wardlow, B.D., Gitelson, A.A., Verma, S.B., Suyker, A.E., Arkebauer, T.J., 2010. A Two-Step Filtering approach for detecting maize and soybean phenology with time-series MODIS data. *Remote Sensing of Environment* 114, 2146–2159. <https://doi.org/10.1016/j.rse.2010.04.019>
- Santanello, J.A., Dirmeyer, P.A., Ferguson, C.R., Findell, K.L., Tawfik, A.B., Berg, A., Ek, M., Gentile, P., Guillod, B.P., van Heerwaarden, C., Roundy, J., Wulfmeyer, V., 2018. Land–Atmosphere Interactions: The LoCo Perspective. *Bulletin of the American Meteorological Society* 99, 1253–1272. <https://doi.org/10.1175/BAMS-D-17-0001.1>
- Schwartz, M.D., 1992. Phenology and Springtime Surface-Layer Change. *Mon. Wea. Rev.* 120, 2570–2578. [https://doi.org/10.1175/1520-0493\(1992\)120<2570:PASSLC>2.0.CO;2](https://doi.org/10.1175/1520-0493(1992)120<2570:PASSLC>2.0.CO;2)
- Schwartz, M.D., Crawford, T.M., 2001. Detecting Energy-Balance Modifications at the Onset of Spring. *Physical Geography* 22, 394–409. <https://doi.org/10.1080/02723646.2001.10642751>
- Sellers, P.J., 1985. Canopy reflectance, photosynthesis and transpiration. *International Journal of Remote Sensing* 6, 1335–1372. <https://doi.org/10.1080/01431168508948283>
- Shaw, R.H., Pereira, A.R., 1982. Aerodynamic roughness of a plant canopy: A numerical experiment. *Agricultural Meteorology* 26, 51–65. [https://doi.org/10.1016/0002-1571\(82\)90057-7](https://doi.org/10.1016/0002-1571(82)90057-7)
- Sonnentag, O., Hufkens, K., Teshera-Sterne, C., Young, A.M., Friedl, M., Braswell, B.H., Milliman, T., O'Keefe, J., Richardson, A.D., 2012. Digital repeat photography for

- phenological research in forest ecosystems. *Agricultural and Forest Meteorology* 152, 159–177. <https://doi.org/10.1016/j.agrformet.2011.09.009>
- Stewart, J.B., 1988. Modelling surface conductance of pine forest. *Agricultural and Forest Meteorology* 43, 19–35. [https://doi.org/10.1016/0168-1923\(88\)90003-2](https://doi.org/10.1016/0168-1923(88)90003-2)
- Su, Y.-S., Yajima, M., 2015. R2jags: Using R to Run “JAGS”.
- Sulla-Menashe, D., Gray, J.M., Abercrombie, S.P., Friedl, M.A., 2019. Hierarchical mapping of annual global land cover 2001 to present: The MODIS Collection 6 Land Cover product. *Remote Sensing of Environment* 222, 183–194. <https://doi.org/10.1016/j.rse.2018.12.013>
- Sulla-Menashe, D., Woodcock, C.E., Friedl, M.A., 2018. Canadian boreal forest greening and browning trends: an analysis of biogeographic patterns and the relative roles of disturbance versus climate drivers. *Environmental Research Letters* 13, 014007. <https://doi.org/10.1088/1748-9326/aa9b88>
- Suyker, A.E., Verma, S.B., Burba, G.G., Arkebauer, T.J., 2005. Gross primary production and ecosystem respiration of irrigated maize and irrigated soybean during a growing season. *Agricultural and Forest Meteorology* 131, 180–190. <https://doi.org/10.1016/j.agrformet.2005.05.007>
- Tan, B., Masek, J.G., Wolfe, R., Gao, F., Huang, C., Vermote, E.F., Sexton, J.O., Ederer, G., 2013. Improved forest change detection with terrain illumination corrected Landsat images. *Remote Sensing of Environment* 136, 469–483. <https://doi.org/10.1016/j.rse.2013.05.013>
- Thornton, P.E., Law, B.E., Gholz, H.L., Clark, K.L., Falge, E., Ellsworth, D.S., Goldstein, A.H., Monson, R.K., Hollinger, D., Falk, M., Chen, J., Sparks, J.P., 2002. Modeling and measuring the effects of disturbance history and climate on carbon and water budgets in evergreen needleleaf forests. *Agricultural and Forest Meteorology*, FLUXNET 2000 Synthesis 113, 185–222. [https://doi.org/10.1016/S0168-1923\(02\)00108-9](https://doi.org/10.1016/S0168-1923(02)00108-9)
- THORNTON, P.E., THORNTON, M.M., MAYER, B.W., WEI, Y., DEVARAKONDA, R., VOSE, R.S., COOK, R.B., 2017. Daymet: Daily Surface Weather Data on a 1-km Grid for North America, Version 3. ORNL Distributed Active Archive Center. <https://doi.org/10.3334/ORNLDAAAC/1328>
- Tilman, D., 1989. Ecological Experimentation: Strengths and Conceptual Problems, in: Likens, G.E. (Ed.), *Long-Term Studies in Ecology: Approaches and Alternatives*. Springer New York, NY, pp. 136–157. https://doi.org/10.1007/978-1-4615-7358-6_6
- Tucker, C.J., 1979. Red and photographic infrared linear combinations for monitoring vegetation. *Remote Sensing of Environment* 8, 127–150. [https://doi.org/10.1016/0034-4257\(79\)90013-0](https://doi.org/10.1016/0034-4257(79)90013-0)
- Uemura, S., 1994. Patterns of leaf phenology in forest understory. *Canadian Journal of Botany* 72, 409–414. <https://doi.org/10.1139/b94-055>
- van Heerwaarden, C.C., Vilà-Guerau de Arellano, J., Gounou, A., Guichard, F., Couvreur, F., 2010. Understanding the Daily Cycle of Evapotranspiration: A Method to Quantify the Influence of Forcings and Feedbacks. *Journal of Hydrometeorology* 11, 1405–1422. <https://doi.org/10.1175/2010JHM1272.1>
- Verma, M., Friedl, M.A., Finzi, A., Phillips, N., 2016. Multi-criteria evaluation of the suitability of growth functions for modeling remotely sensed phenology. *Ecological Modelling* 323, 123–132. <https://doi.org/10.1016/j.ecolmodel.2015.12.005>
- Walther, G.-R., Post, E., Convey, P., Menzel, A., Parmesan, C., Beebee, T.J.C., Fromentin, J.-M., Hoegh-Guldberg, O., Bairlein, F., 2002. Ecological responses to recent climate change. *Nature* 416, 389–395. <https://doi.org/10.1038/416389a>

- Wang, P., Li, D., Liao, W., Rigden, A., Wang, W., 2019. Contrasting Evaporative Responses of Ecosystems to Heatwaves Traced to the Opposing Roles of Vapor Pressure Deficit and Surface Resistance. *Water Resources Research*.
<https://doi.org/10.1029/2019WR024771>
- Wang, T., Ottlé, C., Peng, S., Janssens, I.A., Lin, X., Poulter, B., Yue, C., Ciais, P., 2014. The influence of local spring temperature variance on temperature sensitivity of spring phenology. *Global Change Biology* 20, 1473–1480. <https://doi.org/10.1111/gcb.12509>
- Wang, Z., Schaaf, C.B., Sun, Q., Shuai, Y., Román, M.O., 2018. Capturing rapid land surface dynamics with Collection V006 MODIS BRDF/NBAR/Albedo (MCD43) products. *Remote Sensing of Environment* 207, 50–64. <https://doi.org/10.1016/j.rse.2018.02.001>
- White, M.A., Beurs, K.M.D., Didan, K., Inouye, D.W., Richardson, A.D., Jensen, O.P., O’keefe, J., Zhang, G., Nemani, R.R., Leeuwen, W.J.D.V., Brown, J.F., Wit, A.D., Schaepman, M., Lin, X., Dettinger, M., Bailey, A.S., Kimball, J., Schwartz, M.D., Baldocchi, D.D., Lee, J.T., Lauenroth, W.K., 2009. Intercomparison, interpretation, and assessment of spring phenology in North America estimated from remote sensing for 1982–2006. *Global Change Biology* 15, 2335–2359. <https://doi.org/10.1111/j.1365-2486.2009.01910.x>
- Wilson, K.B., Baldocchi, D.D., 2000. Seasonal and interannual variability of energy fluxes over a broadleaved temperate deciduous forest in North America. *Agricultural and Forest Meteorology* 100, 1–18. [https://doi.org/10.1016/S0168-1923\(99\)00088-X](https://doi.org/10.1016/S0168-1923(99)00088-X)
- Wolf, S., Keenan, T.F., Fisher, J.B., Baldocchi, D.D., Desai, A.R., Richardson, A.D., Scott, R.L., Law, B.E., Litvak, M.E., Brunsell, N.A., Peters, W., van der Laan-Luijkx, I.T., 2016. Warm spring reduced carbon cycle impact of the 2012 US summer drought. *Proceedings of the National Academy of Sciences of the United States of America* 113, 5880–5885. <https://doi.org/10.1073/pnas.1519620113>
- Wolkovich, E.M., Cook, B.I., Allen, J.M., Crimmins, T.M., Betancourt, J.L., Travers, S.E., Pau, S., Regetz, J., Davies, T.J., Kraft, N.J.B., Ault, T.R., Bolmgren, K., Mazer, S.J., McCabe, G.J., McGill, B.J., Parmesan, C., Salamin, N., Schwartz, M.D., Cleland, E.E., 2012. Warming experiments underpredict plant phenological responses to climate change. *Nature* 485, 494–497. <https://doi.org/10.1038/nature11014>
- Wood, J.D., Sadler, E.J., Fox, N.I., Greer, S.T., Gu, L., Guinan, P.E., Lupo, A.R., Market, P.S., Rochette, S.M., Speck, A., White, L.D., 2019. Land-Atmosphere Responses to a Total Solar Eclipse in Three Ecosystems With Contrasting Structure and Physiology. *Journal of Geophysical Research: Atmospheres* 124, 530–543. <https://doi.org/10.1029/2018JD029630>
- Woodcock, C.E., Allen, R., Anderson, M., Belward, A., Bindschadler, R., Cohen, W., Gao, F., Goward, S.N., Helder, D., Helmer, E., Nemani, R., Oreopoulos, L., Schott, J., Thenkabail, P.S., Vermote, E.F., Vogelmann, J., Wulder, M.A., Wynne, R., 2008. Free Access to Landsat Imagery. *Science* 320, 1011–1011. <https://doi.org/10.1126/science.320.5879.1011a>
- Wouters, H., Petrova, I.Y., van Heerwaarden, C.C., Vilà-Guerau de Arellano, J., Teuling, A.J., Meulenbergh, V., Santanello, J.A., Miralles, D.G., 2019. Atmospheric boundary layer dynamics from balloon soundings worldwide: CLASS4GL v1.0. *Geoscientific Model Development* 12, 2139–2153. <https://doi.org/10.5194/gmd-12-2139-2019>
- Xiao, X., Hollinger, D., Aber, J., Goltz, M., Davidson, E.A., Zhang, Q., Moore, B., 2004. Satellite-based modeling of gross primary production in an evergreen needleleaf forest. *Remote Sensing of Environment* 89, 519–534. <https://doi.org/10.1016/j.rse.2003.11.008>

- Yang, X., Mustard, J.F., Tang, J., Xu, H., 2012. Regional-scale phenology modeling based on meteorological records and remote sensing observations. *Journal of Geophysical Research: Biogeosciences* 117. <https://doi.org/10.1029/2012JG001977>
- Yang, X., Tang, J., Mustard, J.F., 2014. Beyond leaf color: Comparing camera-based phenological metrics with leaf biochemical, biophysical, and spectral properties throughout the growing season of a temperate deciduous forest. *Journal of Geophysical Research: Biogeosciences* 119, 181–191. <https://doi.org/10.1002/2013JG002460>
- Zeller, K., 2000. Wintertime Ozone Fluxes and Profiles above a Subalpine Spruce–Fir Forest. *Journal of Applied Meteorology* 39, 92–101. [https://doi.org/10.1175/1520-0450\(2000\)039<0092:WOFAPA>2.0.CO;2](https://doi.org/10.1175/1520-0450(2000)039<0092:WOFAPA>2.0.CO;2)
- Zhang, Q., Phillips, R.P., Manzoni, S., Scott, R.L., Oishi, A.C., Finzi, A., Daly, E., Vargas, R., Novick, K.A., 2018. Changes in photosynthesis and soil moisture drive the seasonal soil respiration-temperature hysteresis relationship. *Agricultural and Forest Meteorology* 259, 184–195. <https://doi.org/10.1016/j.agrformet.2018.05.005>
- Zhang, X., 2015. Reconstruction of a complete global time series of daily vegetation index trajectory from long-term AVHRR data. *Remote Sensing of Environment* 156, 457–472. <https://doi.org/10.1016/j.rse.2014.10.012>
- Zhang, X., Friedl, M.A., Schaaf, C.B., 2006. Global vegetation phenology from Moderate Resolution Imaging Spectroradiometer (MODIS): Evaluation of global patterns and comparison with in situ measurements. *Journal of Geophysical Research: Biogeosciences* 111. <https://doi.org/10.1029/2006JG000217>
- Zhang, X., Friedl, M.A., Schaaf, C.B., Strahler, A.H., 2004. Climate controls on vegetation phenological patterns in northern mid- and high latitudes inferred from MODIS data. *Global Change Biology* 10, 1133–1145. <https://doi.org/10.1111/j.1529-8817.2003.00784.x>
- Zhang, X., Friedl, M.A., Schaaf, C.B., Strahler, A.H., Hodges, J.C.F., Gao, F., Reed, B.C., Huete, A., 2003. Monitoring vegetation phenology using MODIS. *Remote Sensing of Environment* 84, 471–475. [https://doi.org/10.1016/S0034-4257\(02\)00135-9](https://doi.org/10.1016/S0034-4257(02)00135-9)
- Zhang, X., Jayavelu, S., Liu, L., Friedl, M.A., Henebry, G.M., Liu, Y., Schaaf, C.B., Richardson, A.D., Gray, J., 2018a. Evaluation of land surface phenology from VIIRS data using time series of PhenoCam imagery. *Agricultural and Forest Meteorology* 256–257, 137–149. <https://doi.org/10.1016/j.agrformet.2018.03.003>
- Zhang, X., Liu, L., Liu, Y., Jayavelu, S., Wang, J., Moon, M., Henebry, G.M., Friedl, M.A., Schaaf, C.B., 2018b. Generation and evaluation of the VIIRS land surface phenology product. *Remote Sensing of Environment* 216, 212–229. <https://doi.org/10.1016/j.rse.2018.06.047>
- Zhang, X., Liu, L., Yan, D., 2017a. Comparisons of global land surface seasonality and phenology derived from AVHRR, MODIS, and VIIRS data. *Journal of Geophysical Research: Biogeosciences* 122, 1506–1525. <https://doi.org/10.1002/2017JG003811>
- Zhang, X., Wang, J., Gao, F., Liu, Y., Schaaf, C., Friedl, M., Yu, Y., Jayavelu, S., Gray, J., Liu, L., Yan, D., Henebry, G.M., 2017b. Exploration of scaling effects on coarse resolution land surface phenology. *Remote Sensing of Environment* 190, 318–330. <https://doi.org/10.1016/j.rse.2017.01.001>
- Zhang, Y., Li, D., Lin, Z., Santanello, J.A., Gao, Z., 2019. Development and Evaluation of a Long-Term Data Record of Planetary Boundary Layer Profiles From Aircraft Meteorological Reports. *Journal of Geophysical Research: Atmospheres* 124, 2008–2030. <https://doi.org/10.1029/2018JD029529>

- Zhao, L., Lee, X., Smith, R.B., Oleson, K., 2014. Strong contributions of local background climate to urban heat islands. *Nature* 511, 216–219. <https://doi.org/10.1038/nature13462>
- Zhao, L., Lee, X., Suyker, A.E., Wen, X., 2016. Influence of Leaf Area Index on the Radiometric Resistance to Heat Transfer. *Boundary-Layer Meteorology* 158, 105–123. <https://doi.org/10.1007/s10546-015-0070-4>
- Zohner, C.M., Benito, B.M., Svenning, J.-C., Renner, S.S., 2016. Day length unlikely to constrain climate-driven shifts in leaf-out times of northern woody plants. *Nature Climate Change* 6, 1120–1123. <https://doi.org/10.1038/nclimate3138>
- Zohner, C.M., Renner, S.S., 2017. Innately shorter vegetation periods in North American species explain native–non-native phenological asymmetries. *Nature Ecology & Evolution* 1, 1655. <https://doi.org/10.1038/s41559-017-0307-3>

CURRICULUM VITAE

